Estimation of wintertime Arctic sea ice thickness with satellite scatterometers

H. N. Egbers

April 2019

Technische Universiteit Delft

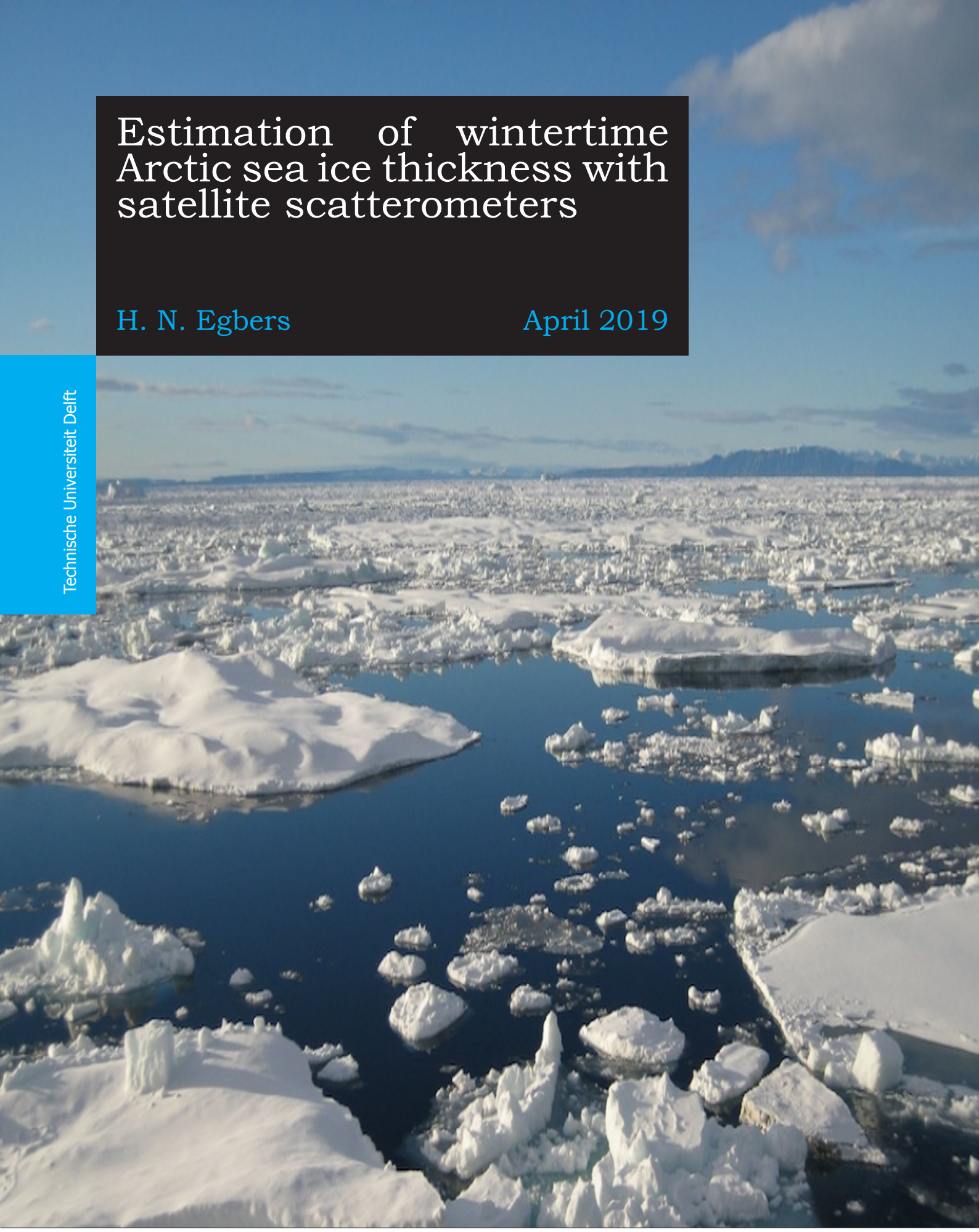

TU Delft Delft University of Technology

Challenge the future

Estimation of wintertime Arctic sea ice thickness with satellite scatterometers

by

H. N. Egbers

in partial fulfillment of the requirements for the degree of

Master of Science
in Applied Earth Sciences

at the Delft University of Technology,
to be defended publicly on 24 April, 2019 at 14:00 PM.

Supervisors:	Dr. ir. M. Belmonte - Rivas	KNMI
	Dr. ir. S. L. M. Lhermitte	TU Delft
Thesis committee:	Prof. dr. ir. R. F. Hanssen	TU Delft
	Dr. ir. S. L. M. Lhermitte	TU Delft
	Dr. ir. D. C. Slobbe	TU Delft
	Dr. ir. M. Belmonte - Rivas	KNMI

TU Delft Delft University of Technology

Preface

In my final year as a Master student at Delft University of Technology I spoke to a lot of people in order to find a suitable MSc research project. I would like to thank Miren Vizcaino for her efforts to set up a meeting with Maria Belmonte-Rivas at the KNMI, because this would end in an interesting research topic after weeks (or months) of discussions with several staff members at the Faculty of Civil Engineering and Geosciences. I would also like to thank the scatterometer workgroup at the KNMI for fruitful discussions and helping me out with practical problems I encountered during my stay at the KNMI.

Finally, I would like to express my appreciation to my parents, family and friends for their support in a turbulent year. Last, but not least, I would like to thank Bregje for her advice and patience during this period, which helped me a lot in putting together this thesis.

H. N. Egbers
Delft, April 2019

Abstract

Accurate information on Arctic sea ice thickness has been historically limited both spatially and temporally to spare submarine sonar measurements until the advent of satellite altimeters such as ICEsat (operating from 2002 to 2008) and CryoSat-2 (operating from 2011 to present day). This study aims to use the historical record of normalized radar backscatter measurements from satellite Ku-band and C-band scatterometers (ERS, QuikSCAT and ASCAT), which have been continuously operating since 1992, to homogenize the satellite altimeter record and extend the record of Arctic sea ice thickness measurements backwards in time.

This study is structured so as to first derive a set of empirical relationships between normalized backscatter measurements and wintertime sea ice thickness estimates in the Arctic using existing satellite altimeter records as a reference. Two separate scatterometer sea ice thickness models are produced using coincident scatterometer and altimeter observations, one for C-band sea ice thickness estimation using ASCAT and CryoSat-2 collocations, and another for Ku-band sea ice thickness estimation using QuikSCAT and ICESat collocations. Based on the agreement to the altimeter records, the estimation of wintertime sea ice thickness using the C-band and Ku-band scatterometer models is uncertain to within 0.5 m (1-sigma), that is, a precision similar to that of the original altimeter references. The homogenization of the satellite altimeter records cannot be done directly, because the ICESat and CryoSat-2 instruments operate in different periods, but it can be done indirectly by comparing the sea ice thickness estimates obtained from Ku-band (based on ICESat) and C-band (based on CryoSat-2) estimates during the years that the Ku-band and C-band scatterometers operate simultaneously. These overlap years have been used to verify the consistency between the C-band and Ku-band relationships, and to correct for a 0.55 m bias in the CryoSat-2 reference, having considered the earlier ICESat record as absolute standard. After removing this bias from the CryoSat-2 reference, the sea ice thickness estimates from C-band and Ku-band records agree to within 0.15 m (1-sigma). Moreover, the resulting scatterometer sea ice thickness models allow the introduction of new thickness thresholds from a previously existing backscatter-based classification of Arctic sea ice types, providing a thickness threshold of 1.54 m to define first year ice (FYI), and a thickness threshold of 2.25 m to separate second year ice (SYI) from older multiyear ice (old MYI).

Ancillary datasets were used to investigate the correlations between backscatter-based sea ice thickness and physical variables, such as snow depth and surface deformation, in order to investigate possible sources of systematic error, which otherwise appear to be bound within 0.30 m (1-sigma). The maps of differences between scatterometer and altimeter sea ice thickness estimates were analysed in terms of collocated sea ice convergence, sea ice shear and snow depth parameters using a multiple regression model. The results show that both the Ku-band and C-band models underestimate ice thickness in areas of high convergence such as the Fram Strait, and overestimate ice thickness in areas with high shear such as the Beaufort Gyre. These correlations may be interpreted as led by increases in backscatter due to surface deformation with (case of convergence) or without (case of shear) associated increases in ice thickness. In addition, the Ku-band model is found sensitive to snow load, with overestimation interpreted as led by an increase in backscatter without associated ice growth, and the C-band model is sensitive to marginal rough ice. An unphysically large dependence on snow depth was found for the C-band estimate, which we conjecture is due to problems with the CryoSat-2 reference.

Finally, a reconstruction of Arctic sea ice thickness in the wintertime has been made by combining the Ku-band and C-band sea ice thickness models with the normalized radar backscatter record of ERS, QuikSCAT and ASCAT from 1992 through 2017. These showed a decline average Arctic sea ice thickness of -0.28 m / decade, with a steady decline in second-year ice and high variability in the mean multi-year ice thickness.

Contents

List of Figures

List of Tables

Nomenclature

Acronyms

ASCAT	Advanced Scatterometer
AVHRR	Advanced Very High Resolution Radiometer
AWI	Alfred Wegener Institute
CAA	Canadian Arctic Archipelago
CS-2	CryoSat-2
DORIS	Doppler Orbitography and Radiopositioning Integrated by Satellite
EASE	Equal-Area Scalable Earth
ERS	European Remote-Sensing Satellite
ESA	European Space Agency
FYI	First Year Ice
GLAS	Geoscience Laser Altimeter System
GMF	Geophyiscal Model Function
GPS	Global Positioning System
IABP	International Arctic Buoy Programme
ICESat	Ice, Cloud, and land Elevation Satellite
KNMI	Koninklijk Nederlands Meteorologisch Instituut
LIDAR	Light Detection and Ranging
LRM	Low Resolution Mode
MSS	Mean Sea Surface
MYI	Multi Year Ice
NASA	National Aeronautics and Space Administration
NIR	Near-Infrared
NLLSQ	Non-linear Least Squares
NSIDC	National Snow and Ice Data Center
PIOMAS	Pan-Arctic Ice-Ocean Modeling and Assimilation System
PS	Polar Stereographic
QuikSCAT/QSCAT	Quik Scatterometer
RMSE	Root Mean Square Error
ROI	Region of Interest
SAR	Synthetic Aperture Radar
SARIn	Synthetic Aperture Radar Interferometric
SIRAL	SAR Interferometric Radar Altimeter
SSA	Sea Surface Anomaly
SSM/I	Special Sensor Microwave/Imager
SSMIS	Special Sensor Microwave Imager Sounder
SYI	Second Year Ice
TFMRA	Threshold First Maximum Retracker Algorithm
THC	Thermohaline Circulation

Symbols

Latin

A	Area	$[m^2]$
d	Diameter	$[m]$
d_f	Freeboard height	$[m]$
d_i	Sea ice thickness	$[m]$
d_s	Snow depth	$[m]$
G	Gain of the antenna	$[dB]$
P_r	Power received back from the target by the radar	$[Watts]$
P_t	Input power of the transmitted signal	$[Watts]$
R	Slant range from the radar	$[m]$
S	Surface area	$[m^2]$
t	Time	$[s]$
u	Eastward velocity	$[m/s]$
u_x	x-ward velocity in EASE-Grid	$[m/s]$
v	Northward velocity	$[m/s]$
v_y	y-ward velocity in EASE-Grid	$[m/s]$

Greek

θ	Incidence angle	$[°]$
ψ	Azimuth angle	$[°]$
λ	Wavelength	$[m]$
σ	Standard deviation	$[-]$
μ	Mean	$[-]$
σ^0	Backscatter coefficient	$[-]$
σ^0_{dB}	Backscatter coefficient	$[[dB]]$
ρ_i	Sea ice density	$[kg/m^3]$
ρ_s	Snow density	$[kg/m^3]$
ρ_w	Water density	$[kg/m^3]$

1

Introduction

1.1. General context

Arctic sea ice is an important element of the global climate. It modulates heat, moisture and momentum exchanges between the ocean and atmosphere due to the variability in sea ice extent and thickness (Kurtz et al., 2011). Sea ice extent has been derived with help of satellite passive radiometers such as AMSR and SSMI(S) or satellite scatterometers such as ERS-1/2, the SeaWinds instrument aboard QuikSCAT and ASCAT. Recently, an Arctic sea ice extent record has been produced which combined measurements from these missions (Belmonte-Rivas et al., 2018). Scatterometers are also able to monitor the evolution of backscatter response of sea ice and different types of sea ice can be distinguished by investigating the backscatter signature of the sea ice surface.

However, to fully understand the impact of changing sea ice cover in the Arctic, knowledge of sea ice extent is not sufficient. A variable sea ice extent causes changes in albedo, but a variable sea ice thickness causes changes in the heat exchange between the ocean and atmosphere in the Arctic. (Zhang et al., 2012) stated that the percentage decline of Arctic sea ice volume is much larger than that of Arctic sea ice area. The seasonal variance of Arctic sea ice plays an important role to understand the impact of both sea ice extent and sea ice thickness. The summer of 2007 showed a drastic retreat of summer sea ice extent and trends in sea ice area was strongly negative at -13.5% per decade (Comiso, 2012). Figure 1.1 shows the large seasonal change in Arctic sea ice extent during the months December-April.

Recently, Arctic sea ice thickness has been derived from satellite altimetry measurements, such as from ICESat (2003-2009) and CryoSat-2 (2010 - present). Limitations of these measurements are however that campaigns were short and that ICESat sea ice thickness information was limited to track measurements during these short periods of measurements. Similarly, CryoSat-2 derived sea ice thickness has the same limitations and another limitation is that CryoSat-2 measures with a Ku-band radar, instead of a lidar as ICESat and Ku-band radar waves are able to penetrate through the surface. However, earlier mean ice thickness observations, based on declassified submarine sonar data, have been sparse spatially and temporally in the past (Kwok and Rothrock, 2009). Figure 1.2 shows the evolution of Arctic sea ice thickness based on a regression analysis of the submarine record from 1975-2000 and the ICESat + CryoSat-2 measurement periods during February-March and October-November within the area delimited in the lower left of the figure (Kwok, 2018). The variability between winter and fall is high, where February - March sea ice is up to 1 m thicker than October-November. This record does however show some periods in which no sea ice thickness information is available.

A recent study done by Tschudi et al. (2016b) proposed a relationship between sea ice age and sea ice thickness. Sea ice age is defined as the amount of summer melt cycles that a given sea ice parcel has undergone over time. Sea ice age is typically derived derived from passive microwave sea ice extent and sea ice motion vectors, which are integrated in to a lagrangian sea ice tracking model. Sea ice age is also seen to be correlated with normalized radar backscatter, as backscatter increases as sea ice grows older. Therefore, by combining these ideas to relate sea ice age to backscatter and sea ice age to thickness, an opportunity arises to use normalized radar backscatter as a useful proxy for sea ice thickness in the Arctic to extend knowledge even when altimetry measurements were not available. Normalized radar backscatter periods are available during 1992-present on a daily basis at

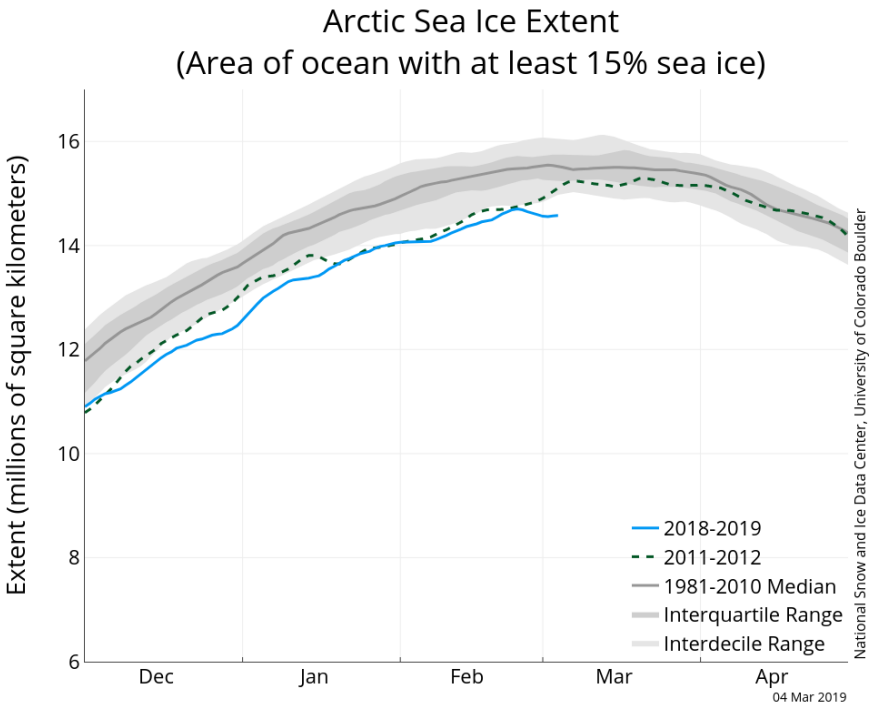

Figure 1.1: Arctic sea ice extent from December - April (NSIDC, 2019)

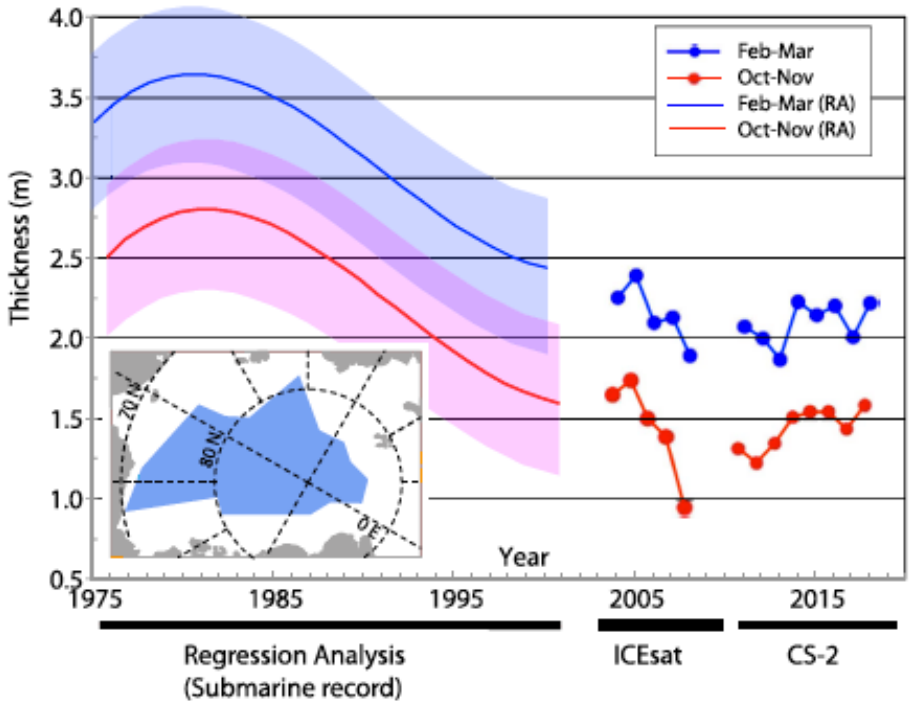

Figure 1.2: Changes in mean winter and fall sea ice thickness, from a submarine record, ICESat and CryoSat-2.The blue/red shadings show the expected residuals in the regression analysis. The inset shows the area covered by US submarine data. (Kwok, 2018)

C- and Ku-band, providing the option of being used as a proxy for sea ice thickness, such that the record in figure 1.2 can be extended. However, scatterometer measurements exhibit their own limitations during melting conditions, since melt effects result in substantial surface wetness and melt pond fractions that mask the backscatter signature of the underlying sea ice (Drinkwater and Liu, 2000). Therefore, the ideal period to focus on is a period in which melt conditions are limited, such that the radar scattering will be much less influenced by melt ponds and water on top of the sea ice, since these have greatly different scattering properties (Onstott, 1992). For this reason, wintertime measurements (where wintertime is defined as March) of normalized radar backscatter and Arctic sea ice thickness are used in this study. Seasonal variability is excluded in this way, but the assumption is made that backscatter signatures of winter sea ice does not change with time.

The radar backscatter response measured by scatterometers will be different for varying ice types, for example less radar backscatter will be registered for first-year ice (FYI) than for multi-year ice (MYI) (Onstott, 1992). MYI is defined as sea ice that has survived the summer melting period and will generally be thicker than FYI, which partly melts during summer and fractions of FYI that survive the summer melt period will be called second-year ice (SYI). Figure 1.3 shows the distribution of sea ice age types in the Arctic. A large decrease in older ice can be observed in the Western part of the Arctic basin, but the distribution of sea ice age has not changed much geographically. However, the lower panel in figure 1.3 shows that the fraction of older ice has drastically decreased since 1980, especially since 2007. This is compensated by an increase in fractions of first year ice in the Arctic basin.

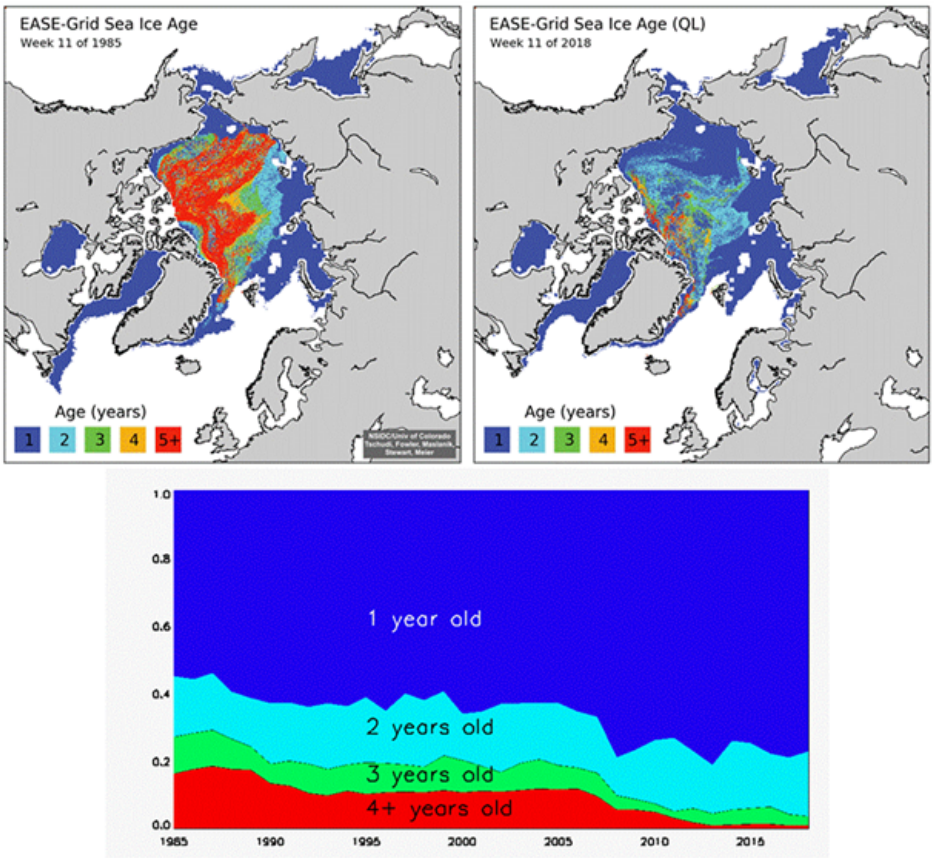

Figure 1.3: Sea ice coverage map for a) March 1985, b) March 2018 c) per year (1985-2018) (Perovich et al., 2018).

The scope of this research is to use the normalized radar backscatter measurements done by ERS, QuikSCAT and ASCAT to estimate wintertime (March) Arctic sea ice thickness, by using collocated sea ice thickness measurement from ICESat and CryoSat-2. A theoretical background on active remote sensing of sea ice is given in chapter 2. A description of the used (ancillary) datasets is provided in chapter 3. The methods, results and discussion on the backscatter models are provided in chapter 4. The methods and results on the derived scattermeter record of wintertime Arctic sea ice thickness are

presented in chapter 5. Finally, concluding remarks and recommendations can be found in chapter 6.

1.2. Research questions and objectives

This research focuses on extending the availability of Arctic sea ice thickness data, since there is a gap in sea ice thickness information outside of the periods when satellite altimeters such as ICESat and CryoSat-2 operate. Furthermore, ICESat/CryoSat-2 provide limited thickness information, whereas using the normalized radar backscatter as a proxy provides a way of estimating Arctic wintertime sea ice thickness on a daily and monthly basis in March. The goal is to establish empirical relationships relating the normalized radar backscatter at C- and Ku-band scatterometers to wintertime (March) sea ice thickness by using collocated sea ice thickness data from ICESat and CryoSat-2. This leads to the following research question:

How can normalized radar backscatter measured from satellite scatterometers be used to estimate wintertime Arctic sea ice thickness?

Subquestions that are derived from the research questions are:

- What is the empirical relationship between wintertime (March) Arctic sea ice thickness and σ^0 at C- and Ku-band?
- What is the consistency of the empirical relationships when they are applied?
- Under which conditions are these relationships valid and what are the limitations and error sources?
- How does the scatterometer based Arctic mean wintertime sea ice thickness evolve from 1992 to present day?

The following objectives will aid in solving the main research question and subquestions.

- Derive a functional empirical relationship between normalized radar backscatter at C- and Ku-band and wintertime (March) Arctic sea ice thickness by using QuikSCAT - ICESat and ASCAT - CryoSat-2 collocated data.
- Evaluate the performance of these relationships in comparison with the used training data (ICESat / CryoSat-2)
- Check the consistency between the estimates given by the C-band relationship with the Ku-band relationship during mission overlap years
- Find physical processes that are responsible for disagreement between scatterometer and altimeter based sea ice thickness
- Provide a reconstruction of wintertime (March) Arctic sea ice thickness estimated with empirical relationships over the backscatter record of ERS, QuikSCAT and ASCAT during 1992-2017

2

Background

The polar caps have been monitored for decades with both active and passive microwave remote sensing instruments. This chapter starts with a section on the importance and physics of sea ice. This is followed by the theory and application of microwave remote sensing of sea ice.

2.1. Sea ice

2.1.1. Significance of sea ice

Sea ice is the frozen part of the polar oceans and is one of the major components of the cryosphere. It has a local important role in the polar ecosystem, but it is also an important moderator of the global climate. This section describes the role of sea ice locally and globally.

Local and global influence

Sea ice has an important role in the polar ecosystem. Its extent varies greatly seasonally, but the loss of Arctic sea ice impacts species living in the Arctic, such as polar bears, wolves, foxes, seals and fish. A loss of sea ice also opens up possibilities for new Arctic shipping routes, disturbing the habitat of these species further. Furthermore, algae thrives below the surface of sea ice and once spring begins the algae growth increases. The algae are eaten by zooplankton, which are the base of the food chain. So, a decrease in algae levels due to disappearing sea ice can cause the entire food chain to be affected (Arrigo et al., 2008).

Besides having influence on ecology, sea ice decline is also one of the mechanisms which can cause polar amplification, because of the reflective properties of sea ice, since sea ice reflects more incoming radiation than open water (Onstott, 1992). So any change in sea ice locally can cause the temperature to increase further at a local scale. Sea ice also has a vital role in the global climate system. The albedo of sea ice is much higher than the albedo of the oceans, thus sea ice reflects incoming solar radiation better than other surfaces and hence leads to lower temperatures. A loss of sea ice means a loss of albedo and thus leading to less areas where radiation can be reflected back into space. More energy is absorbed at the surface and thus the temperature will rise. This causes a feedback loop since higher temperatures will cause more sea ice to melt (Deser et al., 2010). Apart from this, sea ice also insulates the oceans from heat loss and if the sea ice cover declines, the insulation will reduce and cause the ocean to lose heat to the atmosphere (Vihma, 2014). This means that the polar regions are exceptionally sensitive to climate change.

Sea ice also has a large effect on the movement of water in the worlds oceans through the thermohaline circulation (THC), as shown in figure 2.1. Even though the surface water movements are mainly driven by winds, salinity and temperature play a role in water transport. This ”conveyor belt” is thus driven by density differences in water masses, since the density of water is greatly influenced by temperature or salinity differences. The cooling of water at high latitudes leads to a lower temperature of water masses at the poles and due to the nature of the sea ice formation process, the salinity in the water below sea ice will be high due to brine flushing (Cox and Weeks, 1974), where the salt is ejected from the sea ice into the underlying water. The lower temperature and increased salt concentration will result in a high density water mass and these dense waters will sink (downwelling). These regional

density and temperature differences cause the constant circulation of water, making the THC also an important mechanism for heat distribution in the oceans. Thus, a change in the amount of sea ice could impact ocean circulation, due to reduced reflection of sunlight (albedo feedback), leading to warmer water masses at high latitudes (Rahmstorf, 2006).

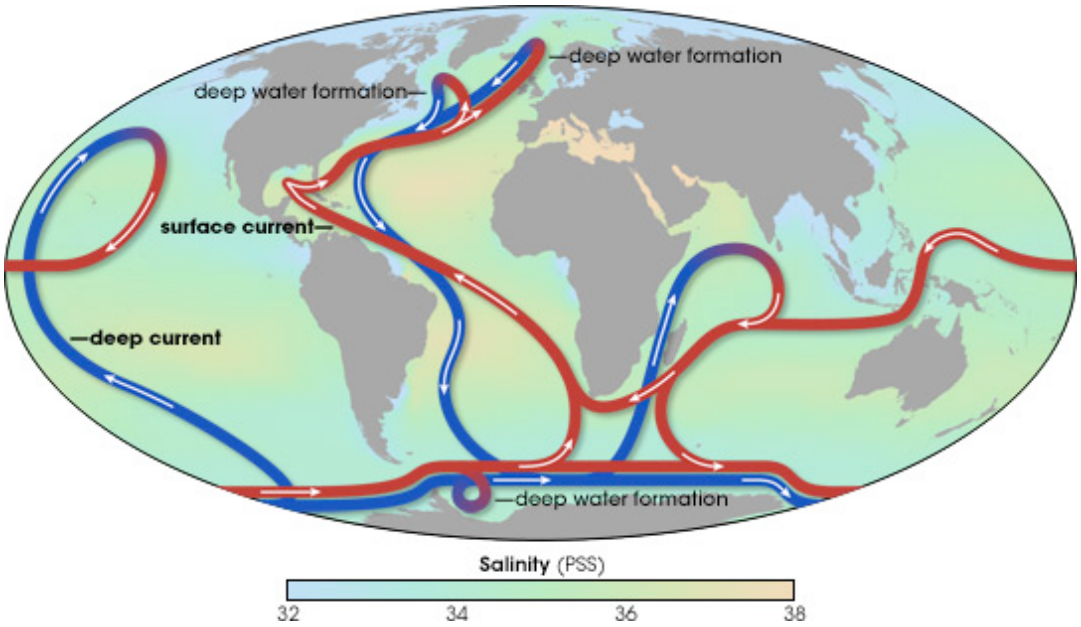

Figure 2.1: Thermohaline circulation (Credit: NASA Earth Observatory).

2.1.2. Current state

Both the Arctic and Antarctic regions are prone to the high seasonality that occurs at these latitudes. Seasonal changes causes the sea ice extent and thickness to increase in autumn/winter and decrease during spring/summer. These regions are however quite different in sea extents and sea ice thickness. The Arctic has a typical maximum sea ice extent of $16 \cdot 10^6 km^2$ and a minimum of $7 \cdot 10^6 km^2$, while the Antarctic sea ice extent varies between $19 \cdot 10^6 km^2$ and $3 \cdot 10^6 km^2$. Typically, the sea ice thickness in the Arctic will be higher than in the Antarctic, 2-3 m (up to 5> m) and 1-2 m, respectively.

The annual sea ice extent has decreased with 3.8% in the Arctic in the period of 1979-2012 (Vaughan et al., 2013). Arctic sea ice thickness has also decreased in the last decades, as shown in figure 1.2 (Kwok, 2018). More recently, a rapid decline of thickness in multi-year ice in the Arctic has also been observed. The decline in Arctic sea ice thickness is as worrying as the decline in its extent because of a retreating sea ice cover will cause a positive albedo-feedback loop. Therefore, more knowledge on Arctic sea ice thickness is desirable.

2.1.3. Physics and classification

Sea ice formation

It is important to understand the formation, dynamics and composition of sea ice in order to interpret microwave radar measurements. Shokr and Sinha (2015) and Gow and Tucker (1990) provide detailed descriptions on the formation of sea ice.

Once the ocean surface is cool enough, a random suspension of ice crystals forms at the surface, called *frazil*. If this occurs in calm seas, frazil continues to form an unconsolidated layer of crystals called *grease ice*. Once frazil crystals form, a good fraction of the original seawater salt content will be ejected into the ocean, while another fraction gets trapped into vertically elongated brine pockets between ice crystals. Further freezing results in a thin layer of dark ice, called *dark nilas* and these will become lighter as it thickens. The nilas can be pushed around and slide over each other under the influence of ocean currents or winds, this process is also known as *rafting*. The sea ice will grow further due to crystallization and the ice continues to thicken and transforms in a stable layer with a smooth bottom surface, *congelation ice*.

Frazil follows a different pathway to transform into sheet sea ice in rough oceans. In these conditions frazil crystals will form disks of ice, *pancakes* or *pancake ice*. Typical features of pancake ice are raised edges due to pancakes bumping into each other. Again, if the winds or ocean currents are strong enough, rafting may occur. Once the ice is thick enough, a process called *ridging* will occur and cause the sea ice to pile up, creating ridges which can be several meters thick. Once the sea ice is formed into sheet ice, it will continue to grow throughout winter. The arrival of spring/summer and thus higher temperatures will cause sea ice to melt. The ice that does not melt completely during summer and survives until next winter is called *second year ice*. The fresh water melt ponds on top of the sea ice will drain the brine channels and desalinate the sea ice further and increase the size of the brine channels. If second year ice survives another melt cycle in the summer, it will be called *multiyear ice*. As a result of continued brine drainage, the multiyear sea ice backscatter signature is different due to its very low salinity and higher porosity. Typical values of salinity, thickness and snow cover are given in table 2.1. Note that in this study the following a distinction is made between SYI and older MYI. SYI is ice that has survived one melt cycle and older multi-year ice is sea ice that has survived two or more melt cycles.

Sea ice classification

Sea ice is usually classified into different classes, depending on its age or its associated thickness. Table 2.1 shows how sea ice is classified (Comiso, 2010). New ice refers to ice that has just started growing. New ice transforms into young ice when the thickness increases up to 30 cm and the salinity decreases to 15 ppm. When a snow layer covers the young ice and the ice thickness increases again, it will become (thin) FYI. If first year ice survives one summer melt cycles it will be called second-year ice. Older ice, thus having survived more than 2 summer melt cycles, will be called multi-year ice.

Table 2.1: Sea ice types and characteristics.

Ice Type	**New**	**Young**	**Thin First Year**	**First Year**	**Multi-Year**
Thickness (cm)	<10	<30	<70	<200	~200
Salinity (ppm)	25	15	4-15	4-5	2
Snow cover (cm)	0	0	~10	~10	~30

Normalized radar backscatter thresholds for C- and Ku-band have been established in Belmonte-Rivas et al. (2018) based on the MY ice fractions reported by SAR in Kwok (2004) and based on the apparent separability of the SY and older MY ice classes in the space of backscatter measurements. This provides an efficient way of distinguishing seasonal (FY) and perennial ice (MY). Table 2.2 shows σ^0 thresholds for FYI, SYI and old MYI.

Table 2.2: Sea ice type σ^0 thresholds for C- and Ku-band.

Sea ice type	**C-band threshold [dB]**	**Ku-band threshold [dB]**
FYI	< -18.3	< -14.5
SYI	> -18.3 & < -15	> -14.5 & < -10
old MYI	> -15	> -10

2.2. Active remote sensing of sea ice.

Active remote sensing of sea ice can be done with different instruments, depending on the desired parameter. Microwave scatterometers are used to determine sea ice extent and altimeters are used to determine sea ice freeboard and thickness. A microwave scatterometer is a radar instrument which measures the *normalized radar cross section* (σ^0), also called backscatter coefficient of a surface illuminated with microwave energy coming from the radar. The backscatter, or the power that is reflected back towards the receiver, is related to several variables such as the surface roughness, dielectric constant and ice structure. Typically, backscatter consists of many individual point scatterers which will

cause a more diffuse reflection (for example on a ridge) than specular reflection on a smooth surface, which will give a more mirror like reflection (in calm waters), as shown in 2.3.

The transmitted and received power by a radar instrument such as a scatterometer are related by the radar equation, as given in equation 2.1.

$$P_r = \frac{P_t G^2 \lambda^2 A}{(4\pi^3) R^4} \sigma^0, \tag{2.1}$$

In this equation P_r is the power received by the radar, P_t is the transmitted power, G is the antenna gain, λ is the wavelength of the signal, A is the effective area of the receiving antenna and R is the slant range from the receiver to the target and σ^0 is the normalized radar cross section or backscatter coefficient. The backscatter coefficient σ^0 is typically expressed in dB:

$$\sigma^0_{dB} = 10 \cdot \log(\sigma^0) \tag{2.2}$$

Backscatter measurements made with scatterometers also depend on other factors, such as incidence (θ) and azimuth (ϕ) angle, but also on the frequency and polarization of the transmitted signal. Figure 2.3 shows how the backscatter response varies for multi-year ice (MYI), first year ice (FYI) and open water.

Backscatter from open water is a purely surface scattering phenomenon, arising from the change in dielectric permittivity that occurs at the ocean surface and modulated by the surface roughness induced by the wind. Backscatter from sea ice has both surface and volume scattering contributions. The surface scattering component, enhanced by the strong dielectric contrast that characterizes new ice and modulated by roughness induced by deformation, decreases as sea ice becomes less saline with age. The radar signal then begins to penetrate deeper into older and less saline ice, interacting with wavelength-scale volume inhomogeneities such as air and brine pockets within the ice, and giving rise to the volume scattering component - which is responsible for the stronger backscatter signature that characterizes older ice.

The contribution of snow to the backscatter signature of sea ice can also be important. Kim et al. (1984) found that the effect of a snow cover on top of FYI can be severe and that the effect of a snow cover is higher on FYI than on MYI. The low thermal conductivity of snow compared to sea ice, causes a rise in the temperature of the ice surface, resulting in a higher dielectric constant for the ice, which will in turn change the backscatter from the surface and the scattering volume. The effect of a dry snow cover is also frequency dependent, namely negligible at L-band, but increasing with frequency, as seen for thick FYI in figure 2.2. Therefore, Ku-band is more sensitive than C-band to volume scattering from snow. It should also be noted that the presence of a wet snow cover can block the volume-scattering contribution of MYI (Kim et al., 1984), which is the responsible for the high backscatter signature of old sea ice.

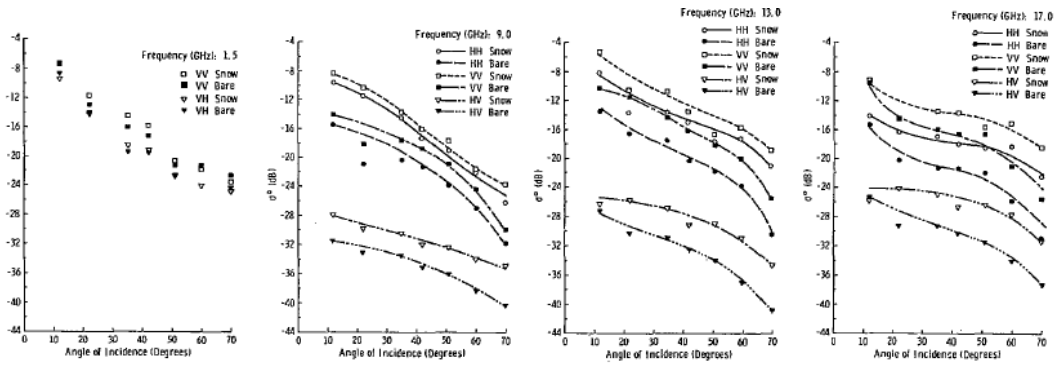

Figure 2.2: Average backscatter coefficient of snow-free and snow-covered thick first year-ice at several frequencies (Kim et al., 1984).

The method used to differentiate sea ice from open water in this study is the Geophysical Model Function approach. This approach calculates the distances to the open water and sea ice GMFs (Geophysical Model Functions). Both the GMFS are defined in an empirical manner to relate the backscatter

coefficient to sea ice properties or to ocean wind properties. This distance is then used to classify a measurement location as either sea ice or open water, depending on the distance between the backscatter measurement point and the GMFs, as done in (Belmonte-Rivas et al., 2012).

Backscatter observations at C- and Ku-band will be used in this study. The measurements made at these 2 different frequencies will give a different backscatter response. For example, Ku-band is more sensitive to volume scattering in multi-year ice (Ezraty and Cavanie, 1999).

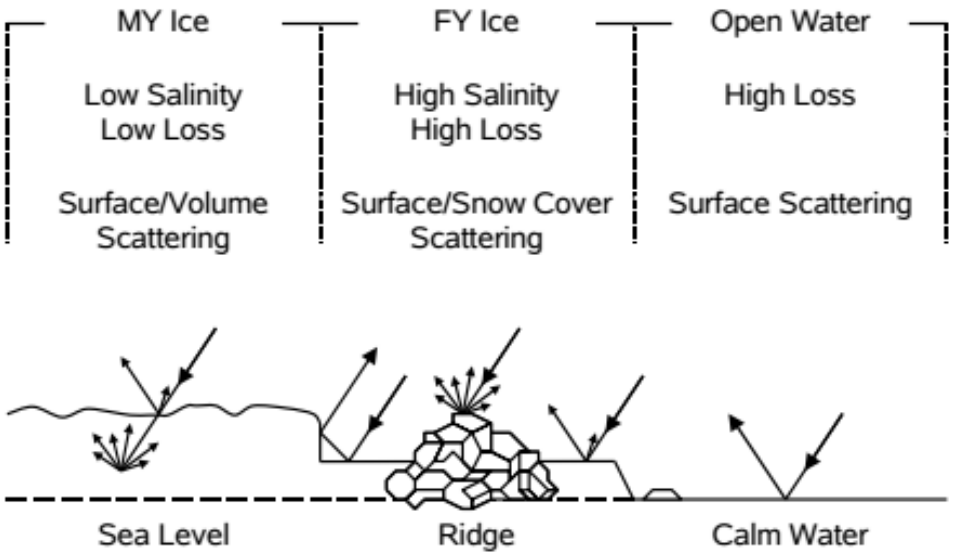

Figure 2.3: Backscatter interactions for different surfaces. (Onstott, 1992)

3

Data Description

This section describes the used data products in this research. Figure 3.1 gives the timeline at which each of the missions was operational. The main scatterometers used in this study are ERS-1/2, QuikSCAT and ASCAT. The main altimeters used are ICESat (lidar) and CryoSat-2 (radar). Both the ERS and ASCAT scatterometers operate at C-band, while QuikSCAT and CryoSat-2 operate at Ku-band.

This chapter describes the used scatterometers and the KNMI σ^0 backscatter in section 3.1 and the Arctic sea ice thickness datasets in section 3.2. A short outline of the sea ice extent classification algorithm is also provided in section 3.1.1 and the sea ice thickness retrieval algorithms are shortly outlined in sections 3.2.2 (ICESat) and 3.2.4 (CryoSat-2).

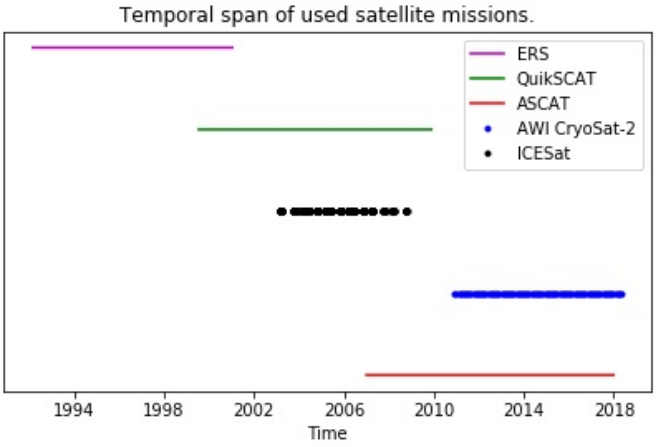

Figure 3.1: Timeline of the used satellite missions.

3.1. Satellite scatterometers

Scatterometer data has been used extensively to investigate wind characteristics above the open ocean since 1978, with the launch of the Seasat Scatterometer (SSCAT) by NASA. ESA then developed and launched the ERS-1 (17/07/1991 - 10/03/2000) & ERS-2 (21/04/1995 - 05/09/2011) satellites, from now on called ERS as both (C-band operating) scatterometers were identical, which is one of three scatterometers used in this study. The second operational scatterometer used in this study, is the Ku-band (13.4 GHz) SeaWinds scatterometer on board the QuikSCAT satellite, launched at June 19, 1999. Finally, the last operational scatterometer used in this study is the at C-band operating Advanced Scatterometer ASCAT, launched onboard MetOp-A at October 19th 2006, followed up by MetOp-B, which was launched at September 17th 2012. Recently, scatterometer data of ERS/QuikSCAT/ASCAT has been used to derive a continuous and homogeneous long term record of sea ice extent and normalized backscatter (Belmonte-Rivas et al., 2018). A detailed description of the algorithm is provided in Otosaka

et al. (2017), Belmonte-Rivas and Stoffelen (2011) and Belmonte-Rivas et al. (2012), but is also briefly discussed in section 3.1.1.

ERS

The ERS satellites boarded a C-band fan-beam scatterometer (5.3 GHz, VV polarization) and was operational from March 1992 until January 2001. Three antennae are on board the instrument looking forward (45° fore-beam), sideways (90°, mid-beam) and backward (135°, aft-beam) w.r.t. the along-track direction of the satellite. The incidence angles over which ERS collects measurements vary from 18 to 64° and in order to find a relationship at C-band, the incidence angle needs to be normalized to a standard incidence angle (52.8°)such that the observed backscatter observations from different missions are comparable. The observation geometry of ERS is given in figure 3.2.

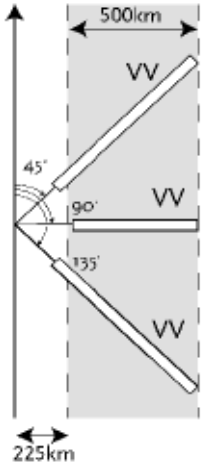

Figure 3.2: ERS scanning configuration. (Stoffelen, 2001)

QuikSCAT

The SeaWinds instrument on board QuikSCAT has a different scanning configuration. It uses a rotating pencil beam antenna at Ku-band (13.4 GHz) which measures the normalized radar backscatter cross-section at 2 polarizations, HH and VV at different incidence angles (46° and 54° respectively). The geometry for this instrument, henceforth called QuikSCAT, is shown in figure 3.3. QuikSCAT provided nearly uninterrupted measurements for nearly a decade, until November 2009. The polarization used in this study is VV, collected at the outer beam at 54°, since ERS/ASCAT both are scatterometers that use VV polarized beams.

ASCAT

The Advanced Scatterometer (ASCAT) instrument on board the MetOp satellite series is a real aperture radar operating at C-band (VV polarization). Like ERS, ASCAT is also a fan-beam scatterometer, but has three antennae mounted on both sides of the instrument. This results in a double sided swath, each 500 km wide. The three antannae on both sides of the satellite are directed 45° forward, orthogonally and 45° backward, thus making triplets of observations of the backscatter coefficient from different directions. The ASCAT scatterometer was fully operational in May 2007 and is currently still active. Since every WVC of ASCAT is illuminated by three beams, one obtains three observations $\sigma^0_{fore}, \sigma^0_{mid}, \sigma^0_{aft}$, each made at a different azimuth and incidence angle. The reference angle at which the ASCAT backscatter measurements are normalized is the same as for ERS, 52.8 °. The observation geometry of ASCAT is shown in figure 3.4.

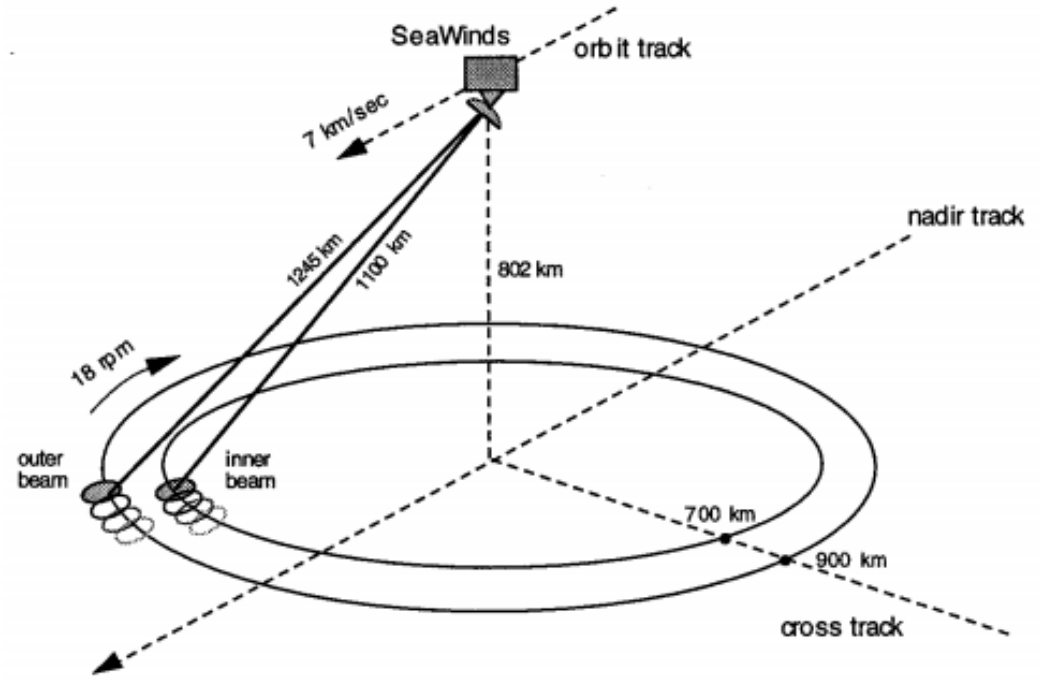

Figure 3.3: SeaWinds scanning configuration. (Spencer et al., 2000)

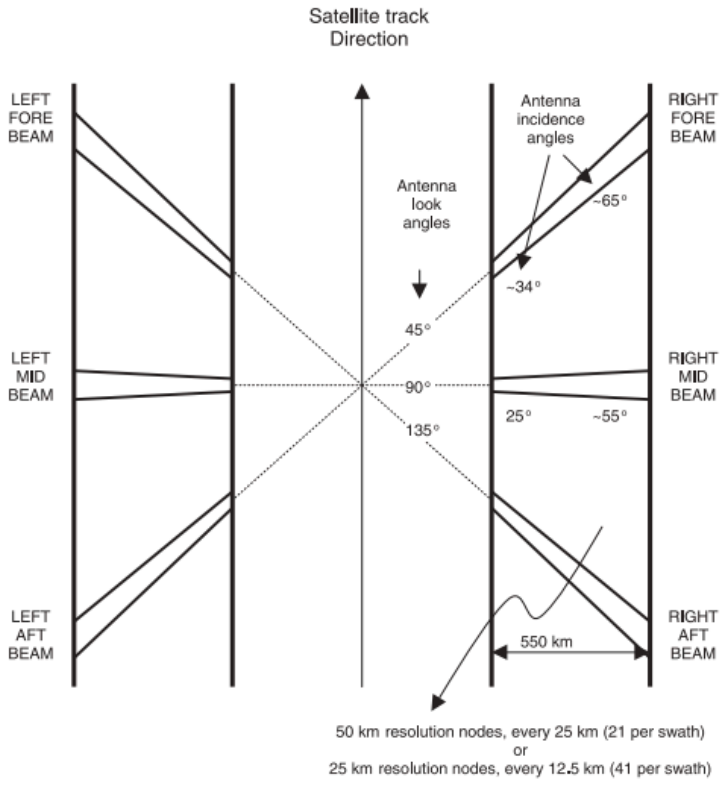

Figure 3.4: ASCAT scanning configuration. (Figa-Saldaña et al., 2002)

3.1.1. Bayesian sea ice extent classification

A brief description of the sea ice extent detection algorithms used is given in this section. The QuikSCAT retrieval algorithm is explained in detail in (Belmonte-Rivas and Stoffelen, 2011), the ASCAT retrieval

algorithm in (Belmonte-Rivas et al., 2012) and the ERS algorithm in (Otosaka et al., 2017).

Bayesian statistics

The Bayesian detection algorithm for ERS, QuikSCAT and ASCAT is based on a Bayesian approach of describing the plausibility of an hypothesis, for example if a pixel contains either sea ice or water. Bayes theorem is used to update the probability of a statement when information becomes available. (Bolstad, 2009) explains that the a-priori probability of an unobserved event and a likelihood function that contains observational information can be combined into the posterior probability. In such a case, Bayes theorem is used to update the a-priori hypothesis ($P(A)$) or probability with information from measurements, which results in the posterior probability ($P(A|B)$). Bayes theorem states as follows:

$$p(A|B) = \frac{P(B|A)P(A)}{\sum_i P(B|A_i) \cdot P(A_i)} \tag{3.1}$$

The Bayesian approach assumes that there are only 2 possibilities, a pixel contains either contains sea ice or water, with a-priori probabilities $p_0(ice), p_0(ocean)$ and posterior probabilities $p(ice|\sigma^0), p(ocean|\sigma^0)$ as follows, since a pixel is either classified as a sea ice surface or an ocean surface. Thus, the total probabilities are stated as given in equations 3.2 and 3.3

$$p_0(ice) + p_0(ocean) = 1 \tag{3.2}$$

$$p(ice|\sigma^0) + p(ocean|\sigma^0) = 1 \tag{3.3}$$

Thus by using Bayes' theorem, the posterior sea ice probability can be derived as:

$$p(ice|\sigma^0) = \frac{p(\sigma^0|ice)p_0(ice)}{p(\sigma^0|ice)p_0(ice) + p(\sigma^0|ocean)p_0(ocean)} \tag{3.4}$$

This equation uses the knowledge from previous satellite passes ($p_0(ice), p_0(ocean)$) and the distance to the ocean and sea ice GMFs ($p(\sigma^0|ice), p(\sigma^0|ocean)$) to update the posterior sea ice probability ($p(ice|\sigma^0)$) after each orbit.

GMFs

The detection algorithm uses the sea ice and ocean geophysical model functions to calculates the distance towards these GMFs. This calculation states that if the probabilistic distance towards the sea ice GMF than to the wind GMF, then it is more likely that this measurement has been made above a sea ice surface than on an ocean surface and vice versa. Geophysical model functions give backscatter triplets according to the for-, mid- and aft-beam measurements. Figure 3.5 shows the ocean and sea ice GMFS for the fore-, mid- and aft-beams for ASCAT. The ocean GMF is a 2-d conical surface, whereas the sea ice GMF is a straight line in backscatter space. The sea ice GMF is also on a straight line for the QuikSCAT and ERS scatterometers as documented in (Otosaka et al., 2017) and (Belmonte-Rivas and Stoffelen, 2011).

The ocean wind GMFS used for ERS and ASCAT is CMOD7. The QuikSCAT wind GMF is based on NSCAT measurements and collocated ECMWF NWP winds (Belmonte-Rivas and Stoffelen, 2011). The ocean GMF relates the backscatter measurements above the ocean to wind properties, such as speed and direction.

The sea ice GMF is slightly different than the ocean wind GMF, since sea ice backscatter shows no directional preference in azimuth, meaning that the fore- and aft-beam illuminate the same surface. This means that $\sigma^0_{ice,FORE} = \sigma^0_{ice,AFT}$ and tells us that all ice points lie on a straight line in backscatter dB-space, the sea ice line. The empirical Ku-band GMF σ^0_{ice} is based on the distribution of winter ice backscatter (pure), which is grouped in a straight curve in QuikSCAT dB space and is described as: $\sigma_{VV,dB} = 1.06 \cdot \sigma_{HH,dB} - 1.0$ (Belmonte-Rivas and Stoffelen, 2011). The C-band sea ice GMF is defined as (Belmonte-Rivas et al., 2012):

$$\sigma^0_{ice} = \begin{cases} \sigma^0_{ice,FORE} = \sigma^0_{ice,AFT} \\ \sigma^0_{ice,MID} = 0.7 + 0.925\sigma^0_{ice,FORE} \end{cases} \tag{3.5}$$

If one changes the measurement coordinate system to a new system (e_a, e_b, e_c), which is defined relative to the ice line in σ measurement space, then one obtains new coordinates (a,b,c), where *a*

is the abscissa along the ice line and *b* and *c* are the coordinates perpendicular to the ice line, with e_c in the plane $\sigma_{fore} = \sigma_{aft}$. The a parameter is a geophysical parameter representing the ice age, coordinates b and c define the distance of a measurement to the ice line as $d = \sqrt{b^2 + c^2}$. A higher a parameter thus means stronger backscatter and older sea ice.

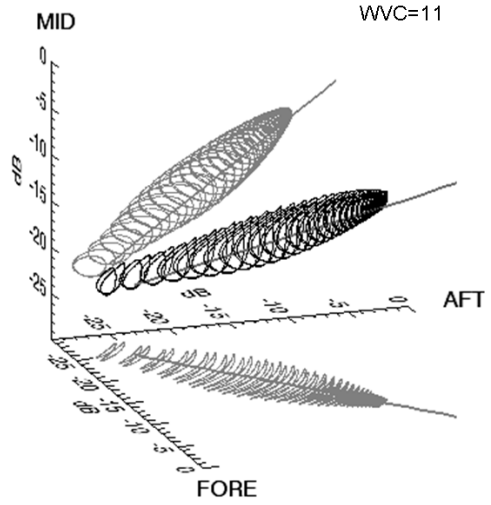

Figure 3.5: GMFs for C-band VV polarized ocean and sea ice backscatter in ASCAT dB-space (Belmonte-Rivas et al., 2012).

Sea ice extent algorithm

The algorithm for ERS, QuikSCAT and ASCAT use the same basic approach to detect sea ice. The following steps are used:

(a) A-priori probabilities initilization (set $P(A)$):

$$p_0(ice) = p(ice|\sigma^0) = 0.35 \tag{3.6}$$

$$p_0(ocean) = 1 - p_0(ice) \tag{3.7}$$

(b) Loop over orbits

- Calculation of $p(\sigma^0|ice), p(\sigma^0|ocean)$
- Calculation of $p(ice|\sigma^0)$
- Calculation of sea ice age
- Update the a-priori probabilities to the newly calculated posterior probabilities: $p_0(ice) = p(\sigma^0|ice)$

(c) Smoothing and relaxation to a-priori information and writing of output.

Smoothing of the sea ice probability is done by means of spatial averaging and the relaxation is applied depending on the posterior probability value as follows:

$$p_0(ice) = \begin{cases} 0.5, & \text{if } p(ice|\sigma^0) > 0.70. \\ 0.15, & \text{if } p(ice|\sigma^0) < 0.70. \end{cases} \tag{3.8}$$

Finally, a threshold is introduced on the value of the posterior probability to classify a pixel either as sea ice or open water. The probability should be at least 55 % to classify a surface as sea ice.

3.1.2. Scatterometer Arctic sea ice extent and normalized backscatter product

The KNMI sea ice product contains sea ice probability and the proxy age of sea ice. The sea ice age is the normalized projection of backscatter on the sea ice GMF in dB (Stoffelen and de Haan, 2001). The proxy age of sea ice can be converted into normalized sea ice backscatter, in VV-polarization for C-band for ERS/ASCAT and HH- or VV-polarization for QuikSCAT. The sea ice probability and sea ice age proxy is presented on a 12.5 km polar stereographic grid. Daily data is available from the ERS (1992-2001), QuikSCAT (1999-2009) and ASCAT (2007-2018) scatterometer missions. The products are given in netCDF files which contain the following parameters:

- X coordinate in km
- Y coordinate in km
- Latitude in degrees
- Longitude in degrees
- Sea ice probability
- Sea ice age (normalized projection of backscatter on sea ice GMF) in dB
- Time of update: time elapsed since last update (ERS)

3.1.3. Data processing

The scatterometer products contain information on the sea ice age, sea ice probability and latitude/longitude (or X-Y grid coordinates). The sea ice age is the projection of the normalized radar backscatter on the sea ice GMF in dB and thus needs to be converted into normalized radar backscatter σ^0. This is done with equation 3.9 for C-band (ASCAT/ERS) and equation 3.10 Ku-band (QuikSCAT), respectively. ERS and ASCAT sea ice age are converted to C-band backscatter at 52.8 degrees of incidence, where $\bar{\sigma^0}$ is the mean fore beam sea ice backscatter, <a> is the mean a-parameter and U_{ice} is the fore beam component of the sea ice GMF vector. QuikSCAT can either be transformed to backscatter collected at the inner beam (HH, 54 degrees of incidence) or the outer beam (VV, 46 degrees of incidence). The values of the used parameters are presented in table 3.1. Since ASCAT and ERS both collect backscatter at VV polarization, the QuikSCAT sea ice age will be converted to sea ice backscatter at VV polarization.

The daily scatterometer products have a different temporal resolution than the sea ice thickness datasets. Sea ice thickness for both ICESat and CryoSat-2 can be seen as a monthly average, whereas σ^0 is available on a daily basis. Therefore, temporal averaging has been applied to the daily March scatterometer data. The geographic mask described in section 3.3.1 is then applied to all datasets to obtain a consistent area of interest, with a reduced high backscatter response for FYI in the marginal ice zone.

$$\sigma^0 = \bar{\sigma^0} + (iceage + < a >) * U_{ice} \tag{3.9}$$

$$\sigma^0_{VV} = offset + (a - < a >) * U_{ice_{VV}} \tag{3.10}$$

Table 3.1: Conversion parameters (KNMI, 2018).

Parameter	Value
$\bar{\sigma^0}$	-17.44 [dB]
<a> [C-band]	-0.42
U_{ice}	0.592
offset	-1.25 [dB]
<a> [Ku-band]	14.00 [dB]
$U_{ice_{VV}}$	0.72083306

Firstly, the daily sea ice age of each grid cell was converted into the normalized radar backscatter σ^0 and averaged such that a March average (representative of wintertime conditions) is obtained. This was done for ERS, QuikSCAT and ASCAT. This results in a sea ice extent record containing the average normalized radar backscatter in March during 1992-2017. The normalized radar backscatter plots can

be found in Appendix A.

Secondly, sea ice thickness data from ICESat and AWI CryoSat-2 was interpolated to the PS12.5 grid such that the each grid cell contains a sea ice thickness value during March 2003-2008 (ICESat) and March 2011-2017 (CryoSat-2). The reference sea ice thickness plots are documented in Appendix B. PIOMAS snow depth, NSIDC sea ice age and the divergence and shear of the sea ice velocity field have also been interpolated to the PS12.5 km grid for later use.

Noticeably, after processing March ERS backscatter data for March 1992 it became clear that the sampling was not complete at that time. Figures 3.6 and 3.7 shows March and April 1992 σ^0 data. Therefore, from this moment onwards April 1992 ERS backscatter will be used as a substitute of the incomplete March 1992 dataset.

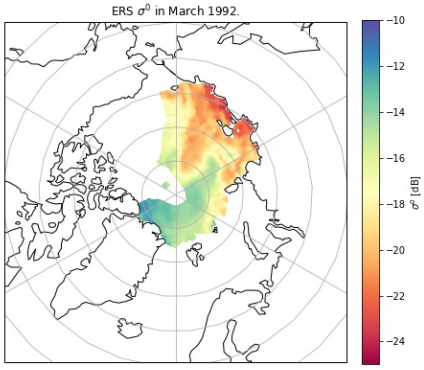

Figure 3.6: ERS σ^0 in March 1992.

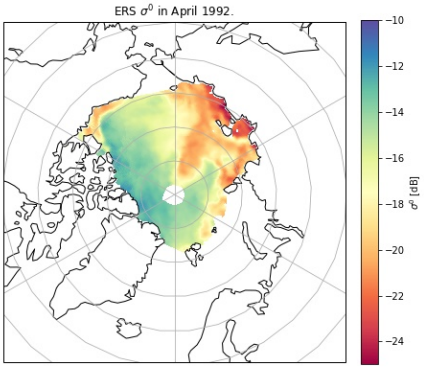

Figure 3.7: ERS σ^0 in April 1992.

3.2. Satellite altimeters

Satellite altimeter data can be used to obtain freeboard and sea ice thickness measurements. Sea ice thickness is obtained by converting freeboard measurements into sea ice thickness, where one assumes hydrostatic equilibrium. The altimeters used in this study are ICESat (2003-2009) (Yi and Zwally, 2009) and CryoSat-2 (2010 - present) (Hendricks et al., 2016). ICESat boards GLAS and is a laser altimeter, while CryoSat-2 is a radar altimeter operating in SAR mode over sea ice areas. ICESat is a beam-limited altimeter and the technique used over sea ice (SAR) for CryoSat-2 is also called delay-Doppler-altimetry. The principle of altimetry is simple: a satellite lidar or radar transmits pulses at high frequencies to the Earth and receives echoes from the Earth's surface. These echoes, or 'waveforms', are then analysed to derive a measurement of the time it took for a signal to make this trip. Together with the constant speed of light at which these signals propagate this holds the range measurement, or distance between the satellite and Earth's surface.

A simple schematic showing a typical situation when measuring sea ice thickness with a altimeter is given in figure 3.8. This figure shows the total sea ice thickness h_i, snow thickness h_s, freeboard h_f, the sea surface height above the reference ellipsoid h_{alt} and the sea surface height h_{ssh}. Note that, thicknesses in this thesis will be noted down with d instead of h in figure 3.8 in order to avoid confusion between thicknesses or ellipsoidal heights, which are typically denoted as h. The use of altimetry in sea ice thickness measurements is based on the assumption that the radar signal reflects from the snow-sea ice interface, instead of the air-snow interface in lidar measurements (Beaven et al., 1995). The following geometrical relations play a role in determination of the sea ice thickness h_i. The total freeboard height is defined as $d_f = d_s + d_i$, where d_s and d_i are snow and sea ice thicknesses, respectively. The total freeboard derived from an altimetry measurement is then the difference between h_{surf} and h_{ssh}, $d_f = h_{surf} - h_{ssh}$, where all heights are measured relatively to a certain reference ellipsoid. This means that the sea ice freeboard can be calculated by using leads, by comparing open water elevation measurements with elevations measurements of ice. h_{surf} is the freeboard height of the snow-air interface and h_{ssh} is the sea surface height relative to the reference ellipsoid. The sea ice thickness d_i is then derived by assuming hydrostatic equilibrium and knowledge

of the snow depth and ice/water/snow densities, either from a climatology or measurements.

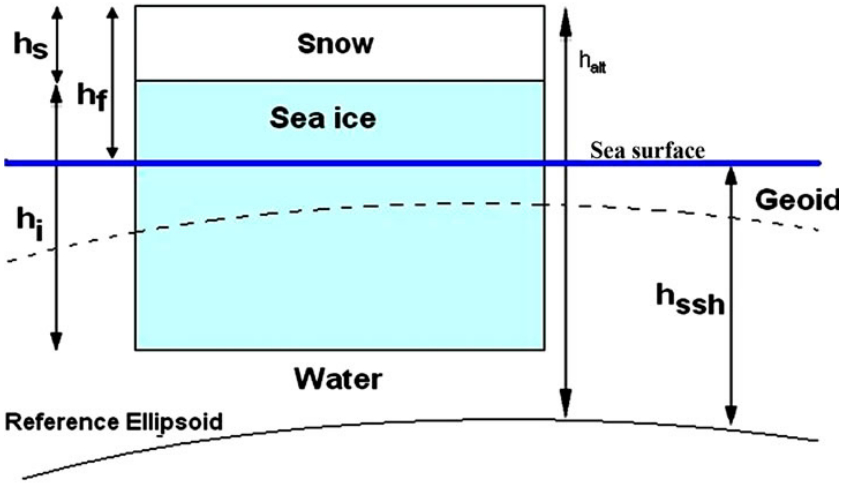

Figure 3.8: Schematic showing sea ice floating on water. (Teleti and Luis, 2013)

3.2.1. ICESat

The ICESat satellite (launched in 2003) boarded a laser altimeter system, the Geoscience Laser Altimeter System (GLAS), which made travel time measurements of laser pulses, allowing sea ice freeboard to be determined with centimeter precision. GLAS consists of three lasers, Laser 1, Laser 2 and Laser 3, but only one laser was operational at a given time (Schutz et al., 2005). Each of the lasers produced beams at two wavelengths 1064-nm (NIR) and 532-nm (green), where the first laser was used to measure the surface height and the latter was used to measure the vertical distribution of clouds and aerosols (Zwally et al., 2002). ICESat operated at 600 km altitude in a near polar (94°) orbit. The laser illuminates areas of 60 m in diameter and are separated 170 m in the along-track direction of the satellite.

3.2.2. ICESat sea ice thickness retrieval algorithm (Zwally et al., 2008)

In this study, the NSIDCs Arctic Sea Ice Freeboard and Thickness (V1) dataset was used.

The method of deriving freeboards uses segments of open water and thin ice detected by the laser altimeter to determine the height of the along□track ocean surface, which is then used as the ocean reference level for the freeboard heights (d_f). The freeboard height is defined as the total height of the snow cover and sea ice above the ocean. The freeboard height d_f is determined relative to an ocean reference level h_o calculated for each ICESat along□track elevation measurement. The ocean reference level is determined by averaging the lowest 2% of relative elevations in a 50km section of the profile - assumed to be coming from open leads (a long, narrow opening in pack ice that may be covered by thin ice). Note that in extreme cases without open water within ±25 km range, h_o will measure the height of thin ice, thus underestimating freeboard (Zwally et al., 2008). A more detailed description on the derivation of the ICESat surface elevation, ocean levels and freeboard is given in Zwally et al. (2008).

Estimation of sea ice thickness from freeboard also requires knowledge of snow density, snow depth, ice density and water density. The sea ice thickness can then be calculated by using the buoyancy principle, leading to an expression for sea ice thickness d_i in equation 3.11. Equation 3.11 shows how the sea ice thickness d_i (m) depends on water density ρ_w, sea ice density ρ_i, snow density ρ_s, freeboard height d_f and snow depth d_s. Constant values of $\rho_w = 1023.9 kg/m^3, \rho_i = 915.1 kg/m^3$ were used, whereas ρ_s was based on (Zwally et al., 2008).

$$d_i = \frac{\rho_w}{\rho_w - \rho_i} d_f - \frac{\rho_w - \rho_s}{\rho_w - \rho_i} d_s \tag{3.11}$$

Mean uncertainties for ICESat derived measurements were reported in Kwok and Cunningham (2008). The ICESat ice drafts were reported to be within 0.5 m of ice draft measurements done

at nearby moorings. Mean sea ice thickness uncertainties for ICESat were reported to be 0.7 m by using error propagation.

NSIDC Arctic freeboard and thickness product V1

This product (Yi and Zwally, 2009) provides information on Arctic sea ice freeboard and thickness. The data was derived from measurements made by GLAS, as described earlier in this chapter. The resolution of the gridded product is 25 km and is presented on a polar stereographic grid, covering an area from 65-86° N at all longitudes. This product can be interpreted as a monthly mean sea ice thickness per grid cell. Data from several ICESat campaigns was used, as presented in table 3.2. The product is available at `https://nsidc.org/data/nsidc-0393` in gridded and ASCII format.

Table 3.2: ICESat datasets used.

Laser	Campaign	Period
1ab	2003	20 Feb - 29 Mar
2b	2004	17 Feb - 21 Mar
3b	2005	17 Feb - 24 Mar
3e	2006	22 Feb - 27 Mar
3h	2007	12 Mar - 14 Apr
3j	2008	17 Feb - 21 Mar

3.2.3. CryoSat-2

CryoSat-2 is an ESA satellite which was launched in 2010. It carries 2 main instruments, a DORIS (Doppler Orbitography and Radiopositioning Integrated by Satellite) tracking system and SIRAL, an SAR Interferometric Radar Altimeter. Its high inclination of 92° allows CryoSat-2 to reach a high global coverage up to 88°. CryoSat-2's main instrument SIRAL (Synthetic Aperture Interferometetric Radar Altimeter) is a 13.5 GHz normal incidence radar altimeter which can operate in three different modes: SAR, Low Resolution Mode (LRM) and SAR Interferometry (SARIn). LRM is a traditional pulse-limited altimetry mode, while SAR has a higher spatial resolution in the along-track direction. SARIn mode uses a second antenna for along-track aperture synthesis, which allows the determination of the cross-track position (Calafat et al., 2017). The SIRAL mode acquisition mask is shown in figure 3.9. Over ice sheets and temperate land ice (purple) SARIn mode will be used, over sea ice SAR mode will be used (green) and over the Antarctic and Greenland ice sheets (and oceans) the LRM will be used (red).

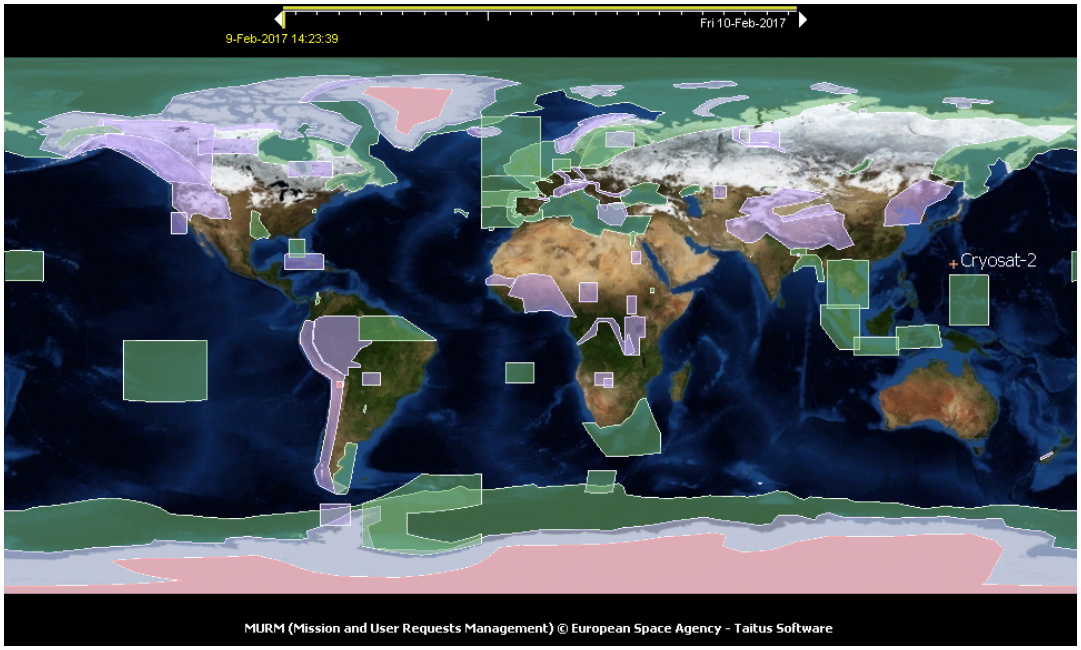

Figure 3.9: SIRAL mode acquisition mask. SARIn (purple) will be used over ice sheet margins and temperate land ice, whereas SAR mode (green) will be used over sea ice and some part of basins/coastlines. LRM (red) will be used above the ocean, the Antarctic and Greenland interiors (ESA, 2019).

3.2.4. AWI CryoSat-2 sea ice thickness retrieval algorithm (Hendricks et al., 2016)

The Alfred Wegener Institute developed its own processor to estimtate sea ice thickness from CryoSat-2 radar waveforms. Another aim of the processor is to estimate uncertainties in sea ice thickness from the CryoSat-2 measurements. In order to estimate the elevation, the AWI processor uses a Threshold-First-Maximum-Retracker (TFMRA) (Ricker et al., 2014), which assumes that the main scattering interface is at 50 percent of the first maximum peak power of the returned waveform. The TFMRA is used for all surfaces to estimate the ellipsoidal elevation (h_L). Afterwards, the elevation needs to be converted to freeboard. This is done by first subtracting the mean sea surface height. AWI uses the DTU15 global MSS height (h_{MSS}) product to reduce errors in areas where the actual sea surface height cannot be obtained due to the absence of leads. Secondly, open water spots are automatically detected in the ice cover. The elevation of these leads defines the sea surface anomaly (h_{SSA}), defined as the deviation of the actual sea surface elevation from the mean sea surface height, which also needs to be subtracted from the ellipsoidal elevation to arrive at the height of the sea-ice surface. An assumption made by AWI is that the main scattering horizon is at the snow-ice interface (see figure 3.8). A correction factor is applied to account for a lower propagation speed in snow. The used correction factor is $\delta_c = d_s(1-\frac{c_s}{c})$, where d_s is the snow depth and c_s is the propagation speed of light in snow and c is the speed of light in vacuum. The sea ice freeboard is finally calculated as $d_f = h_L - (h_{MSS} + h_{SSA}) + \delta_c$. Subsequently, the sea ice thickness d_i is calculated with equation 3.12, by assuming hydrostatic equilibrium.

$$d_i = \frac{\rho_w}{\rho_w - \rho_i} d_f + \frac{\rho_s}{\rho_w - \rho i} d_s \tag{3.12}$$

Fixed values for water density ρ_w, first year ice and multi year sea ice are used (1024 kg/m^3, 916.7 kg/m^3, 882.0 kg/m^3). The snow depth and density from the Warren climatology are used (Warren et al., 1999).

Typical uncertainty values in the freeboard and sea ice thickness retrieval algorithm developed by AWI are shown in figure 3.10. It shows the thickness uncertainties due to surface roughness and physical signal penetration assumptions can lead to biases of up to 0.6 m in FYI and 1.2 m in MYI, which is roughly 10 times the freeboard bias due to the freeboard-thickness conversion.

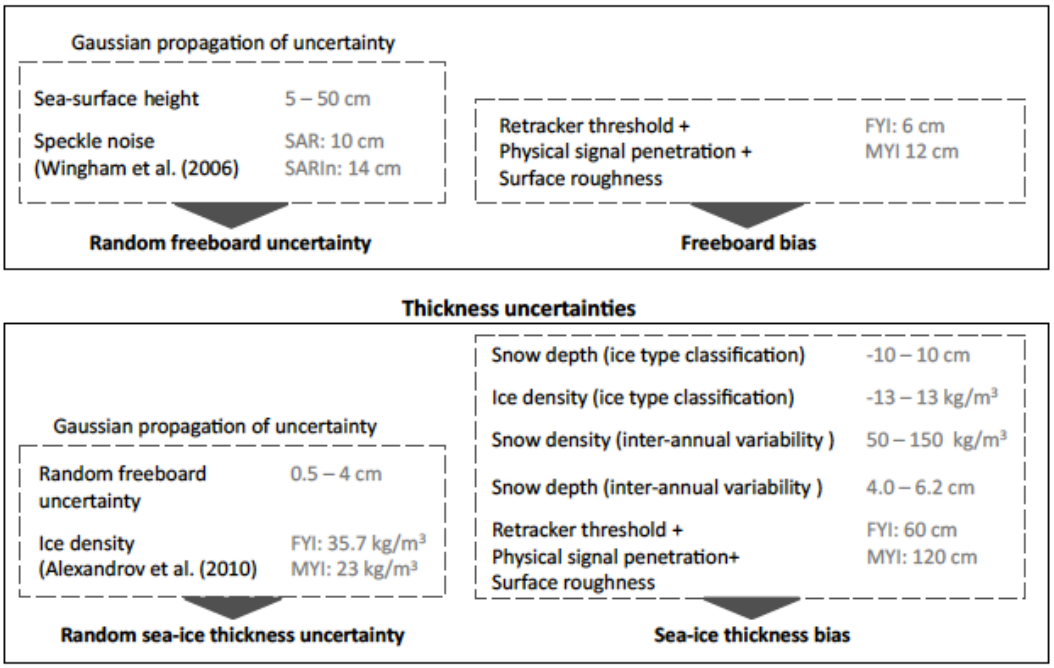

Figure 3.10: CryoSat-2 uncertainties for freeboard and sea ice thickness, showing a typical range per parameter for a single CryoSat-2 measurement (Ricker et al., 2014)

.

AWI CryoSat-2 sea ice thickness product (v1.2)

The Alfred-Wegener Insitute has developed a sea-ice level processor which calculates sea ice thickness and uncertainties in the Arctic. Several versions of this product are available, the latest of which is version 1.2, which will be used in this research. Monthly sea ice thickness data is available from November 2010 until present. Therefore, March data from 2011 - 2017 was used. The gridded data is available from `https://www.meereisportal.de/en.html` on the EASE2.0 grid, where the grid cells are 25 x 25 km^2. It should be noted that at the time of writing this dataset should not be considered as an operational product, because the research on the interpretation of CryoSat-2 radar signals is on-going. It is thus not yet a fully calibrated and validated data product.
The NetCDF data files contain several parameters per grid cell, such as freeboard thickness, random and systematic uncertainties for sea ice freeboard and thickness and (valid) waveform counts. The random sea ice freeboard uncertainties are dependent on the range measurements and the uncertainty of the sea-surface anomaly, which is a function of the standard deviation of lead elevation and the distance to the next lead. Typical values are reported to be 0.10-0.14 m and 0.05 - 0.5 m respectively (Hendricks et al., 2016). The sea ice thickness uncertainties depend on the sea ice freeboard uncertainty and the uncertainty in sea ice density, which is variable for FYI (35.7 kg/m^3) and MYI (23 kg/m^3) (Hendricks et al., 2016). Furthermore, snow depth and density and ice density are also provided. The parameters of interest in this research are limited to: latitude, longitude and sea ice thickness.

Data processing

The used datasets are not provided on the same grid as the scatterometer grids, so it is necessary to collocate the different datasets to the same grid. This grid will be the Northern Polar Stereographic grid (12.5 km, 608*896 grid cells). The KNMI scatterometer products already are presented on this grid, hence all other parameters of interest (PIOMAS snow depth, NSIDC sea ice motion and sea ice age products) from different grids will be interpolated to the PS 12.5 km grid). It is not necessary to mask land or other values, as this has already been done to retrieve the sea ice extent in the KNMI backscatter products and in the sea ice thickness products by AWI and NSIDC.

3.3. Ancillary data

This section describes ancillary products that were used in this research. Firstly, the geographic mask is described in section 3.3.1. PIOMAS and NSIDC sea ice motion and NSIDC sea ice age are described in sections 3.3.2, 3.3.3 and 3.3.4.

3.3.1. Study area and Arctic basin mask

Figure 3.12 shows the study area with a description of the seas. A geographic mask was introduced in order to screen the high-backscatter response of deformed FYI in the marginal ice zone, as defined in (Belmonte-Rivas et al., 2018). This high backscatter is caused by surface deformation due to compression and irreversible snow/ice metamorphism after melt-freeze events (Voss et al., 2003; Willmes et al., 2011). The geographical mask delimits the Arctic basin across the Fram Strait and Svalbard to Severnaya Zemlya through Franz Josef Land. The multi-year ice present in the Greenland sea is also omitted with this geographical mask. The geographic mask is shown in figure 3.11.

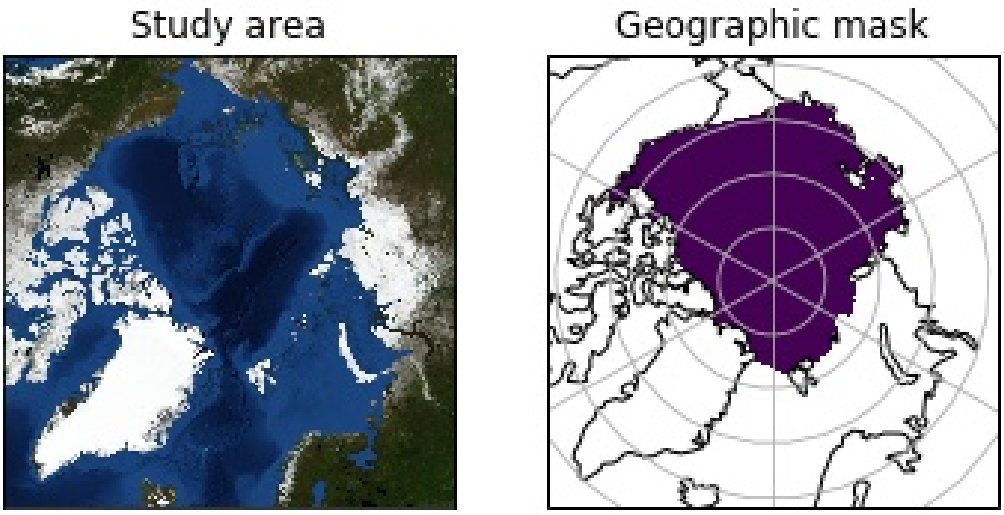

Figure 3.11: Study area and geographic mask.

Figure 3.12: Detailed study area map (Credit: NSIDC).

3.3.2. PIOMAS (v2.1)

The PIOMAS (Pan-Arctic Ice-Ocean Modelling and Assimilation System) (Zhang and Rothrock, 2003) is a model that provides estimates on several important sea ice and ocean parameters, including but not limited to: sea ice thickness, concentration, snow depth, sea ice advection, surface temperature. The model output is available from 1978 - present, with a temporal resolution of one month. It is presented on a generalized curvilinear coordinate system (grid size: 360x120) that has a spatial coverage of 45° to 90 N°. The snow depth parameter is used in this research. The data is accessible at `http://psc.apl.uw.edu/research/projects/arctic-sea-ice-volume-anomaly/data/model_grid` in binary format.

3.3.3. NSIDC ice motion vectors (v3)

This is a sea ice drift dataset that has been constructed with various satellite sensors, available for the northern and southern hemisphere. The southern hemisphere uses data provided by the following sensors: Scanning Multichannel Microwave Radiometer (SMMR), the Spectral Sensor Microwave/Imager (SSM/I) and Imager + Sounder (SSM/IS) and the AVVHR (Advanced Very High Resolution Radiometer). More sensors are available for the Arctic product, since this is consists of the earlier mentioned sensors

and in addition has data of the Advanced Multichannel Scanning Radiometer (AMSR-E), buoy observations of the International Arctic Buoy program (IABP) and ice motion derived from NCEP/NCAR surface wind vectors. It is both available on a daily and monthly basis, however only the monthly product will be used in this research. It contains information on the sea ice velocities *u, v*, gridded sea ice velocities u_x, v_y, velocity (in grid), divergence, vorticity and shear, together with an indicator of the number of days that contain valid data. NSIDC provides the data at https://nsidc.org/data/nsidc-0116 (Tschudi et al., 2017) and NetCDF data containing the additional parameters was made available by the Integrated Climate Data Center of the University of Hamburg (Tschudi et al., 2017). Monthly velocities are provided in [m/s] and divergence/shear/vorticity is provided in [1/s]. Data is provided on a 25 km EASE-grid from November 1978 to February 2017, on daily and monthly temporal resolution.

The parameters used in this research are the monthly divergence and shear. Divergence is defined from the sea ice grid velocities u_x, v_y as $\nabla = \frac{\partial u_x}{\partial x} + \frac{\partial v_y}{\partial y}$, while shear is defined as $\frac{\partial u_x}{\partial y} + \frac{\partial v_y}{\partial x}$. These experimental parameters were calculated over 150 km distance, in order to account for inhomogeneities present in the spatial distribution of ice motion due to incorporation of raw buoy data (Szanyi et al., 2016).

3.3.4. NSIDC EASE-grid sea ice age (v3)

This data set contains weekly estimates of the sea ice age in the Arctic, derived from passive remote sensing satellites, buoys and a weather model. The ice age is derived from multiple passive microwave sensors: SMMR, SSM/I, SSM/IS. Furthermore, visible and infra-red data from AVVHR is used through 2004. Drifting buoy data from the International Arctic Buoy Program (IABP) and the NCEP/NCAR Reanalysis Project (CDAS) were also used in constructing this dataset. The data is provided weekly from November 1978 until February 2017, meaning no data for March 2017 is available for sea ice age. It is provided on 12.5 km Northern Hemisphere Equal Area Scalable Earth Grid (EASE-Grid).
Data is provided in flat binary, 1 byte files with little endian byte order, stored by row. The values in the files are either: 0 (open water or < 15 % sea ice concentration), or [5,10,15, ..., 80] for sea ice age. Division by 5 is necessary to obtain true sea ice age ranging from 1 to 16 years old. Data marked with 254 or 255 is coastline or land, respectively. This dataset is accessible at https://nsidc.org/data/nsidc-0611 (Tschudi et al., 2016a).

4

Scatterometer sea ice thickness model

This chapter introduces the derived scatterometer wintertime sea ice thickness models for C- and Ku-band. Collocated wintertime (monthly mean March) sea ice thickness and normalized radar backscatter data has been used to derive the empirical fits, as presented in section 4.1. This chapter is divided into different sections describing the used methodology (4.1.1) and the results are presented and discussed in section 4.1.2.

A consistency check (section 4.2)was performed after determining the empirical relationships at both C- and Ku-band. The C- and Ku-band estimates during overlap years are compared with the ICESat historical reference and with each other. The used methodology is described in section 4.2.1 and the results are discussed in section 4.2.2.

Finally, this chapter concludes with an error analysis in section 4.3, done separately per frequency with help of ancillary datasets that provide information on several parameters (snow depth, convergence and shear) of sea ice during the collocation period.

4.1. Empirical fit

This section describes how functional relationships were derived, which are able to order to estimate wintertime Arctic sea ice thickness from normalized radar backscatter measurements. This was done separately for C- and Ku-band, however the used methodology is similar and described in section 4.1.1. The results will be presented in section 4.1.2 and will be discussed per frequency band.

4.1.1. Methodology

QuikSCAT scatterometry data and the ICESat derived NSIDC sea ice thickness product was used to determine an empirical relationship between sea ice thickness and normalized radar backscatter at Ku-band in wintertime (mean March measurements during 2003-2008). Similarly, to find a relationship between these parameters at C-band, ASCAT scatterometry data has been used together with the AWI CryoSat-2 sea ice thickness product. 2-Dimensional histograms have been produced to show the distribution of these parameters, after collocation and interpolation to the same grid. These are shown in figures 4.1, 4.2, 4.3 and 4.4. Figures 4.2 and 4.4 will serve as the base of a fitting procedure since the data spread after applying the mask (section 3.3.1) has reduced greatly, due to the masking the high-backscatter response of deformed FYI in the marginal ice zone.

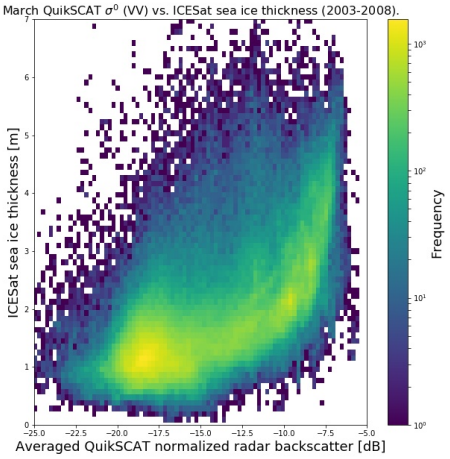

Figure 4.1: 2-D histogram of unmasked QuikSCAT σ^0 vs. ICESat sea ice thickness.

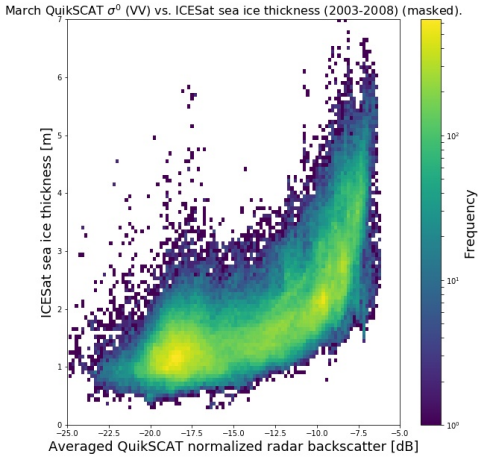

Figure 4.2: 2-D histogram of masked QuikSCAT σ^0 vs. ICESat sea ice thickness.

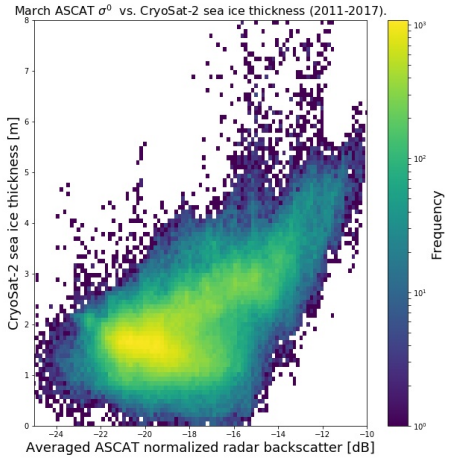

Figure 4.3: 2-D histogram of unmasked wintertime ASCAT σ^0 vs. CryoSat-2 sea ice thickness.

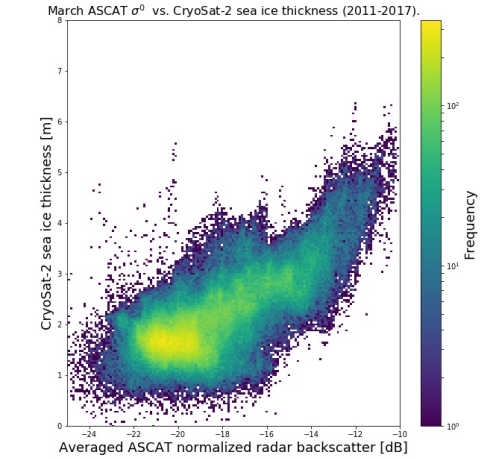

Figure 4.4: 2-D histogram of masked wintertime ASCAT σ^0 vs. CryoSat-2 sea ice thickness.

A functional relationship has to be derived from these 2-D histograms. This can be achieved with equal 2-dimensional binning of the data, where σ^0 is on the x-axis and sea ice thickness d_i on the y-axis. A Gaussian function *f* has been fitted per backscatter bin to end up with a function that best describes the distribution of sea ice thickness per backscatter interval. The backscatter bin sizes are 0.18 dB for Ku-band and 0.14 dB for C-band. The function in equation 4.1 has been used where $x = \sigma^0, b = \mu$ and $c^2 = \sigma^2$, where σ^0 is the normalized radar backscatter in a bin, μ is the mean sea ice thickness in the backscatter bin and σ^2 is the variance. Non-linear least squares (NLLSQ) in form of the Levenberg-Marqardt method was used to estimate the mean sea ice thickness μ and variance σ^2 per backscatter bin.

$$f(x) = a \cdot e^{\frac{-(x-b)^2}{2c^2}} \tag{4.1}$$

The mean sea ice thickness per bin that results from these Gaussians are used as input in another NLLSQ routine to derive a relationship between σ^0 and wintertime (March) Arctic sea ice thickness d_i. Based on the shape of the 2-dimensional histograms, the relationship in equations 4.2 is proposed, with

unknown parameters a, b, c and d to be estimated, σ^0 the backscatter per bin and $\bar{d}_i$ the corresponding mean sea ice thickness per backscatter bin. This will result in the optimal parameters a, b, c, d and an estimation of the covariance matrix. The RMSE of each relationship will be calculated subsequently. The RMSE is defined as $\sqrt{\frac{\sum_{i=1}^{N}(\hat{d}_i - d_i)^2}{N}}$, where $\hat{d}_i$ are the predicted sea ice thicknesses for a grid cell according to the empirical relationship and d_i is the reference thickness for that grid cell, N is the total amount of grid cells that have a sea ice thickness estimate and a reference sea ice thickness. This means that the RMSE in this case is calculated over all data points ranging from 2003-2008 in case of the Ku-band relationship and the C-band RMSE is calculated for all points in 2011-2017.

$$\bar{d}_i = a \cdot e^{b\sigma^0} + c + d\sigma^0 \tag{4.2}$$

If the distribution of residuals has a mean offset when comparing the empirical relationship with the sea ice thickness reference, then this mean offset will be removed to improve the fit. Ideally, there would be no offset since the fitting procedure aims to minimize this offset. However, the mean sea ice thickness per bin might be biased in case of a small amount of data points per backscatter bin.

Finally, after obtaining the optimal fit parameters, an estimation of sea ice thickness can be made using the mean March backscatter in the years 1992-2017. The C-band fit can be applied to ASCAT and ERS backscatter measurements and the Ku-band fit will be used for QuikSCAT, using the previously calculated March average σ^0 values.

4.1.2. Results and discussion

The 2-D histograms in section 4.1.1 contain all collocated points for the overlap years (2003-2008) for Ku-band and (2011-2017) for C-band. Yearly 2-D histograms are provided in Appendix D.

Both histograms (figures 4.4 and 4.2) serve as the base of the Gaussian fitting procedure in which a Gaussian function was fitted for each backscatter bin. The centre of these backscatter bins together with the estimated parameters for the Gaussian function for Ku- and C-band are documented in table C.1 and table C.2.

The results of the parameter estimates (second NLLSQ procedure) and the RMSE are documented in tables 4.1a and 4.1b.

Table 4.1: Results of the NLLSQ fits.

(a) C-band relationship results.

	a	b	c	d	RMSE [m]	σ [m]
Model	30.41	0.21	2.39	0.05	0.47	0.47

(b) Ku-band relationship results.

	a	b	c	d	RMSE [m]	σ [m]
Model	44.24	0.42	1.87	0.04	0.49	0.48

The functional relationships at C-band is:

$$\bar{d}_i = 30.41 \cdot e^{0.21\sigma^0} + 2.39 + 0.05\sigma^0 \tag{4.3}$$

While the relationship at Ku-band becomes:

$$\bar{d}_i = 44.24 \cdot e^{0.42\sigma^0} + 1.87 + 0.04\sigma^0 \tag{4.4}$$

Finally, the 20 and 80 % quantiles are plotted together with the 2-D histograms and their fits in figures 4.5 and 4.6. The residuals of these models are plotted in histograms in figures 4.7 and 4.8, defined as the C/Ku-band estimate - reference thickness. The Ku-band estimate shows a mean offset of -0.106 m and a standard deviation of 0.48 m. The C-band estimate has a mean offset of 0.02 m and a standard deviation of 0.47 m. Note that at this point, the model was established by using all available training data, rather than splitting it. This is because it is desirable to have sea ice thickness / backscatter information for the complete range of the data. Similarly, the model residuals were also

calculated for all points within the geographic basin.
However, in order to assess whether the found offsets and standard deviations are the result from including all data (overtraining the model), a second assessment was made by using randomly splitting the data into 80 % training data and 20 % test data. The results for Ku-band and C-band are shown in table 4.2 and 4.3. It becomes clear form these Ku-band runs that the the mean offset remains approximately -0.1 m, similar to the result of using all data to train the model. The same holds for the RMSE and standard deviation of the residuals between the test and model data. The small variation in model parameters do not influence the overall performance greatly. Similarly, the model parameters for C-band also show some variation, but these variations in model parameters do not influence the the RMSE, the mean of the residuals and the standard deviation of the residuals.

Table 4.2: Ku-band test results after splitting the data into an 80/20 train/test ratio 5 times. Documented are the model parameters A,b,c,d together with the RSME, standard deviation σ and mean offset of the residuals between the test and model data μ.

	run 1	**run 2**	**run 3**	**run 4**	**run 5**
A	45.91	43.69	47.78	43.10	44.29
b	0.42	0.42	0.43	0.41	0.42
c	1.87	1.88	1.89	1.86	1.87
d	0.04	0.04	0.04	0.04	0.04
RMSE [m]	0.49	0.49	0.49	0.48	0.48
σ **[m]**	0.48	0.48	0.48	0.47	0.47
μ **(mean offset) [m]**	-0.10	-0.10	-0.11	-0.11	-0.11

Table 4.3: C-band test results after randomly splitting the collocated data into an 80/20 train/test ratio 5 times. Documented are the model parameters A,b,c,d together with the RSME, standard deviation σ and mean offset of the residuals between the test and model data μ.

	run 1	**run 2**	**run 3**	**run 4**	**run 5**
A	23.28	24.83	24.03	23.13	24.77
b	0.16	0.18	0.17	0.16	0.18
c	0.91	1.68	1.14	0.54	1.37
d	0.01	0.03	0.01	-0.01	0.02
RMSE [m]	0.47	0.47	0.47	0.47	0.47
σ **[m]**	0.47	0.47	0.47	0.47	0.47
μ **(mean offset) [m]**	0.02	0.02	0.02	0.02	0.02

The results of the non-linear least square fitting procedure of the Gaussian fits for Ku-band show that a Gaussian function has some limitations. This holds at high and low end of the σ^0 regime, where few data points are left after applying the geographic mask.

The spread of the reference altimeter sea ice thickness estimates about the scatterometer sea ice thickness models (±0.50 m) is comparable to the reported nominal uncertainty levels for the references (Kwok and Rothrock, 2009; Laxon et al., 2013).
The Ku-band estimate will be corrected for the mean offset, visible in the residuals. This will result in a changing offset in the c-term of equation 4.4. Removing the offset leads to a shifted histogram, as visible in figure 4.9 and to a corrected relationship, as given in equation 4.5.

$$\bar{d}_i = 44.24 \cdot e^{0.42\sigma^0} + 1.76 + 0.04\sigma^0 \tag{4.5}$$

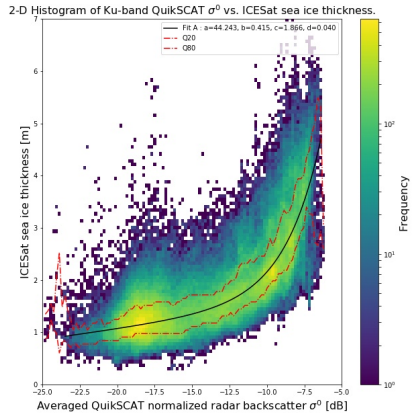

Figure 4.5: 2-D histogram showing QuikSCAT σ^0 vs. ICESat sea ice thickness including Q20-Q80 and fit.

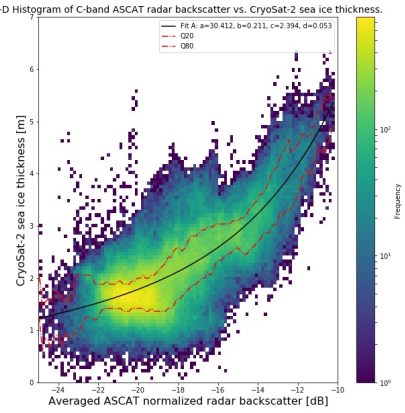

Figure 4.6: 2-D histogram showing ASCAT σ^0 vs. CryoSat-2 sea ice thickness including Q20-Q80 and fit.

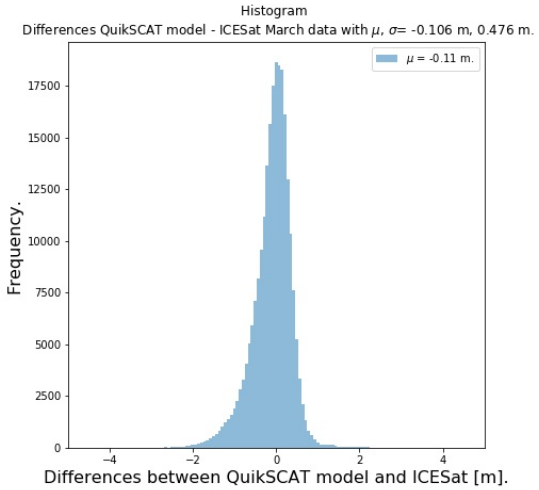

Figure 4.7: Model residuals (QuikSCAT-ICESat) histogram.

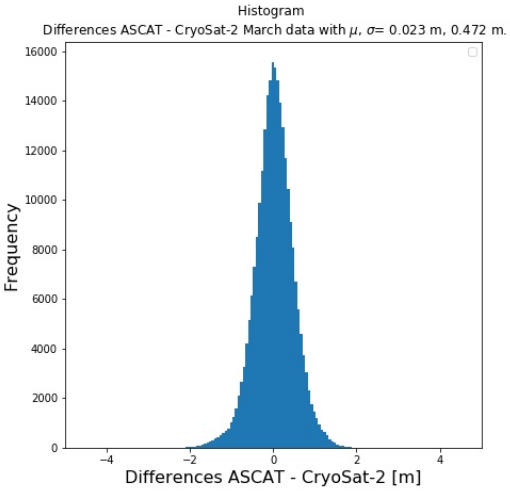

Figure 4.8: Model residuals (ASCAT-CS2) histogram.

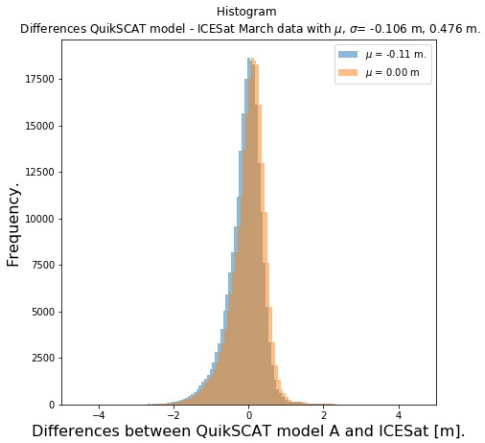

Figure 4.9: Model + corrected residuals (QuikSCAT-ICESat) histogram.

4.1.3. Ku-band relationship

It must be noted that the yearly 2-D histograms in figure D (Appdendix D) indicate that the ICESat sea ice thickness in 2008 is lower than the previous years. A different shape of the distribution can also be observed in 2008.

The results of the non-linear least square fitting procedure of the Gaussian fits for Ku-band show that a Gaussian function has some limitations. This holds at high and low end of the σ^0 regime, where few data points are left after applying the geographic mask. The profit of this mask is that the spread in the data is greatly reduced. The main cause of this is because high backscatter FYI in the marginal seas is masked. Failure of fitting can be recognized in table C.2 due to an inability to estimate the mean and standard deviation (nan/infinity) or extremely high values of $\sigma_a, \sigma_b, \sigma_c$. This means that in some backscatter bins the distribution is not Gaussian, but a very limited amount of bins is influenced by this. The reason is that the scatter in those bins is high and therefore a mean or variance estimation is highly influenced by these extreme data points. The Q20 & Q80 quantiles show this clearly in the ranges of [-25, -23] and > -8 dB.

The following NLLSQ fit is based on the means of the estimated backscatter bins, which are used as input. Backscatter bins that have failed to provide sa reasonable mean estimate are left out in this procedure. The resulting RMSE and sigma was over all years ranging from 2003-2008 in the Ku-band relationship. The resulting RMSE and σ are both 0.48 and 0.49 m, respectively. (Kwok and Rothrock, 2009) states an ICESat altimetry standard deviation of 0.37 m for sea ice thickness, which is slightly better than the observed value of 0.47 m.

4.1.4. C-band relationship

Yearly 2-D histograms provided in Appendix D show little yearly variation in shape, but in some years the distributions tail is less pronounced. March 2017 gives a slightly ambiguous spread in the interval [-22,-16] dB. The observed shapes during 2011-2017 are similar to each other, apart from slight variations.

The Gaussian functions that were fitted again work well up to -12 dB. Failure of providing a good estimate here is caused by a low amount of data points within these backscatter bins, i.e. these bins can not be estimated with a Gaussian. These bins were disregarded and not used further on.

The NLLSQ fit routine for C-band was constructed in the same way as for Ku-band. RMSE and σ were calculated using all data points in (2011-2017) and were 0.47 and 0.47 m, respectively. The RMSE is slightly lower than the RMSE for the Ku-band fit, but the difference is negligible. There reported standard deviation is in line with the standard deviation from the CryoSat-2 altimetry dataset, which was reported to be 0.46 m for gridded ice thickness estimates in (Laxon et al., 2013). The residuals are shown in figure 4.8 and the mean residuals is reported to be 0.02 m, between the C-band estimate and the CryoSat-2 dataset.

Slight differences can be observed between the 2-d histograms between C- and Ku-band. C-band shows significantly less spread in the high backscatter regime.

4.2. Consistency check

This section is devoted to checking the consistency between the scatterometer sea ice thickness relationships with each other and with the ICESat historical record. The methodology used to analyse the consistency is described in section 4.2.1 and the results are presented and discussed in section 4.2.2.

4.2.1. Methodology

The different scatterometry satellite missions have overlap years, as seen in figure 3.1. These mission overlap years can be used to check the consistency of the sea ice thickness models at Ku-band and C-band, since different methods ideally would estimate the same thickness. Overlap years that can be used are 2000 (ERS/QuikSCAT) and 2007/2008/2009 (QuikSCAT/ASCAT). ICESat also has overlap years (2007/2008) with the scatterometer missions and these years can be used to compare the estimates together with ICESat used as reference. ICESat was chosen as historical reference, since Ricker et al. (2014) stated that the AWI CryoSat-2 product might be biased. Furthermore, the ICESat estimates are better tied to the historical record of submarine sonar and EM readings (Kwok and Rothrock, 2009; Vaughan et al., 2013).

Ideally the C- and Ku-band estimates would give the same sea ice thickness estimate, but any systematic differences may be observed by using multiple overlap years. The residuals were calculated

between the different estimates during the overlap years and the results are given in histograms to see whether the estimates agree. These residuals are plotted in figure 4.10.

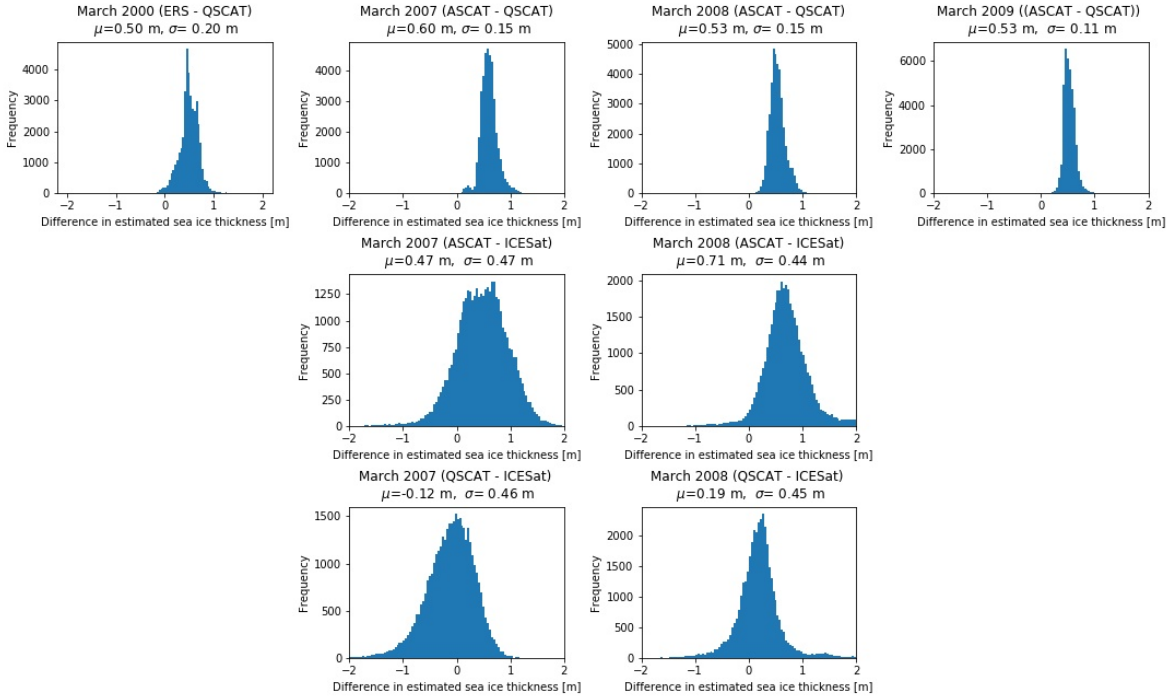

Figure 4.10: Overlap years showing residuals between estimates. The residuals are defined as: ERS estimate - QuikSCAT estimate (2000), ASCAT estimate - QuikSCAT estimate (2007-2009), ASCAT estimate - ICESat (2008) and QuikSCAT estimate - ICESat. All histograms show the residuals on the x-axis and frequency on the y-axis.

A bias may be calculated the from these differences, since the histograms of residuals can provide a mean and standard errors of the estimated sea ice thickness distributions. The method which has been used to calculate a bias is weighted averaging, applied as given in equations 4.8 and 4.9, where $\bar{\Delta}_n$ and is the mean thickness residual between a combination of (C-band, Ku-band, ICESat) and σ_i is the standard deviation of the distribution of the residuals of that combination. A final bias and standard deviation σ^* can be determined using weighted averaging.
Different definitions of $\bar{\Delta}_n$ have been used in this study, as stated as follows. $\bar{\Delta}_1$ (equation 4.6) is the bias between the C-band estimate and ICESat reference, using overlap years 2007 and 2008. $\bar{\Delta}_2$ (equation 4.7) is the bias between the C- and Ku-band estimate, thus solely based on scatterometer information, using overlap years 2000, 2007, 2008 and 2009. If a bias between the C-band estimated sea ice thickness and Ku-band or ICESat is observed, it will be removed for consistency.

$$\bar{\Delta}_1 = \frac{\Delta_{(ASCAT-ICESat)2007} + \Delta_{(ASCAT-ICESat)2008}}{2} \tag{4.6}$$

$$\bar{\Delta}_2 = \frac{\Delta_{(ERS-QuikSCAT)2000} + \Delta_{(ASCAT-QuikSCAT2007)} + \Delta_{(ASCAT-QuikSCAT2008)} + \Delta_{(ASCAT-QuikSCAT2009)}}{4} \tag{4.7}$$

$$bias = \frac{\frac{\bar{\Delta}_1}{\sigma_1^2} + \frac{\bar{\Delta}_2}{\sigma_2^2}}{\frac{1}{\sigma_1^2} + \frac{1}{\sigma_2^2}} \tag{4.8}$$

$$\sigma^* = \frac{1}{\sqrt{\frac{1}{\sigma_1^2}} + \sqrt{\frac{1}{\sigma_2^2}}} \tag{4.9}$$

4.2.2. Results and discussion

An interesting feature can be observed from the information in figure 4.10 and table 4.4, namely the C-band estimate (ASCAT/ERS) gives is consistently higher than the Ku-band estimate of sea ice thickness. The top row in figure 4.10, which illustrates the annual differences between the C-band and Ku-band estimates, shows that the C-band estimate is approximately 0.5 m higher than the Ku-band estimate, with an uncertainty of ±0.15 m. The lower two rows, which show the annual differences between both the C-band and Ku-band sea ice thickness relative to ICESat, indicate that the disagreement between the C- and Ku-band estimates can be traced to a disagreement between the altimetry references used for the C-band model (CryoSat-2) and the Ku-band model (ICESat).

All residuals are defined as (C-band - Ku-band) for scatterometer combinations and as (C- / Ku-band - ICESat) for the ICESat reference. A summary of the mean and standard deviations of the differences are shown in figure 4.10 and in table 4.4. The upper panel in the figure shows the (C- Ku-band) residuals for all years. The middle panel shows the overlap years 2007 and 2008 of ASCAT and ICESat. It is immediately clear that the spread in these distributions is larger than for the scatterometer overlap years. Finally, the lower panel of this figure shows the overlap years of the Ku-band estimate with ICESat. Note that the standard deviation of the differences is remarkably larger when using ICESat as a reference, probably of ICESats larger single shot uncertainty.

This figure shows that the agreement between the C- and Ku-band estimates is better than to the reference, due to lower values of σ. However, the C-band thickness is in all cases higher than the Ku-band estimate and ICESat. Therefore, the C-band thickness estimate is biased high with respect to ICESat as historical reference.

Based on these observed mean differences, a bias was calculated in two different ways. Firstly, a bias that is based on comparison between the ASCAT estimate and the ICESat training data using overlap years 2007 and 2008. Secondly, a bias based on comparing the ASCAT and QuikSCAT thickness estimates was also calculated during overlap years 2000, 2007, 2008 and 2009. Finally, these were combined to obtain 1 single bias estimate with equations 4.8 and 4.9, where weighted averaging was used with the standard deviations as weight. The results are shown in table 4.5.

Table 4.5 shows the results of a weighted averaging these overlap years in one value per combination (C-band - ICESat) or (C-band - Ku-band). An offset of 0.59 $\pm$ 0.12 m for (C-band - ICESat) and 0.54 $\pm$ 0.04 m for (C-band - Ku-band) is observed. Weighted averaging of these two offsets + standard deviations lead to a weighted offset of 0.55 $\pm$ 0.04 m which should be removed from the C-band estimate and CryoSat-2 reference.

Table 4.4: Mean differences and standard deviations observed in overlap years.

Combination	**Year**	**Mean residual [m]**	σ [m]	RMSE [m]
ERS - QuikSCAT	2000	0.50	0.20	0.64
QuikSCAT - ICESat	2007	-0.12	0.46	0.51
ASCAT - ICESat	2007	0.47	0.47	0.67
ASCAT - QuikSCAT	2007	0.60	0.15	0.73
ASCAT - QuikSCAT	2008	0.53	0.15	0.65
ASCAT - ICESat	2008	0.71	0.44	0.84
QuikSCAT - ICESat	2008	0.19	0.45	0.45
ASCAT - QuikSCAT	2009	0.53	0.11	0.64

Table 4.5: Bias between ASCAT - ICESat and ASCAT - QuikSCAT.

Combination	**Years**	**Bias [m]**	σ [m]
C-band - ICESat	2007, 2008	0.59	0.12
C-band - Ku-band	2000, 2007, 2008, 2009	0.54	0.04
Weighted averaging of above results		**0.55**	**0.04**

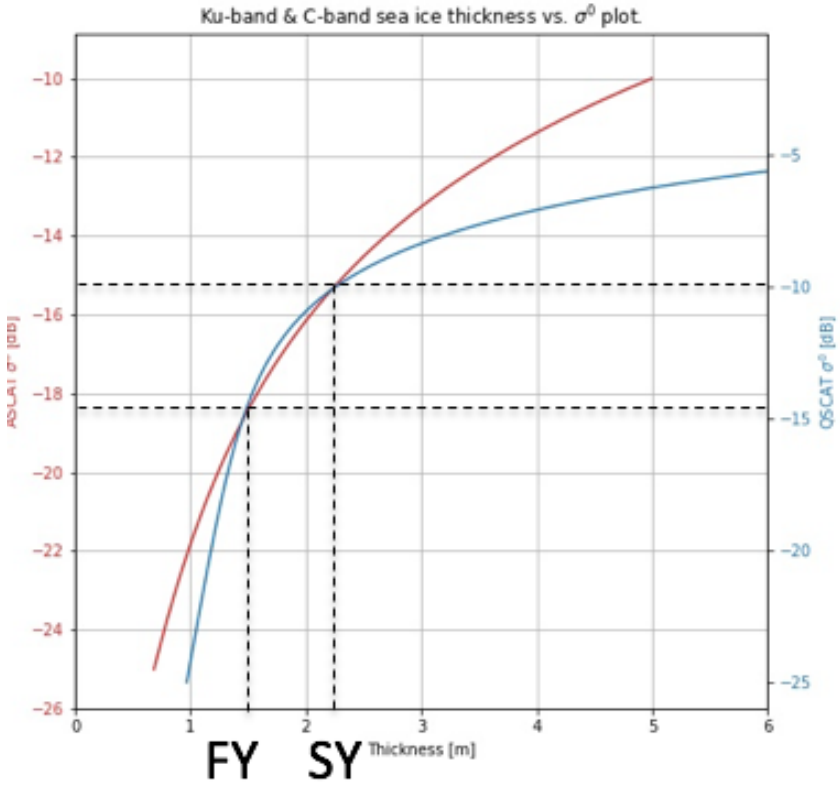

Figure 4.11: σ^0 vs. wintertime Arctic sea ice thickness, 0.55 m bias in C-band was removed.

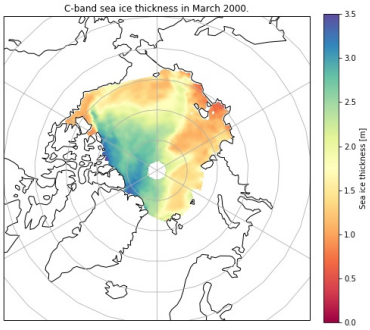

Figure 4.12: ERS (C-band) Arctic sea ice thickness in March 2000.

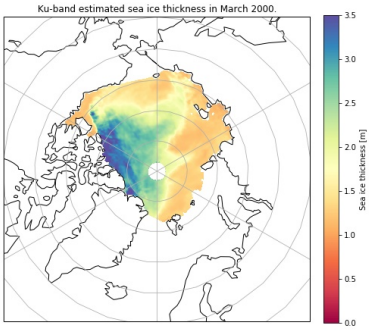

Figure 4.13: QuikSCAT (Ku-band) Arctic sea ice thickness in March 2000.

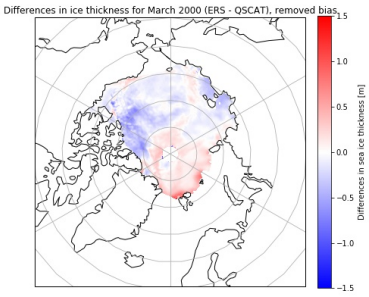

Figure 4.14: Residuals of ERS - QuikSCAT in March 2000.

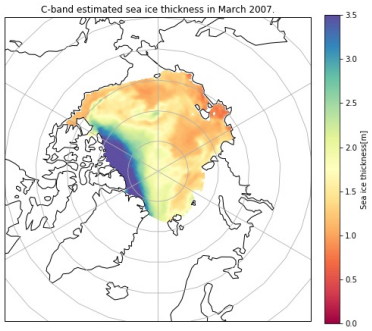

Figure 4.15: ASCAT (C-band) Arctic sea ice thickness in March 2007.

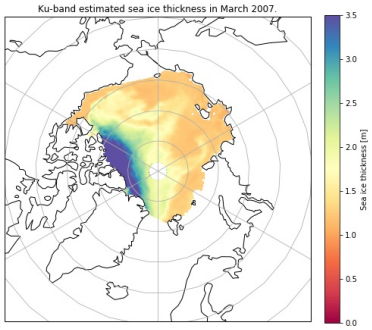

Figure 4.16: QuikSCAT (Ku-band) Arctic sea ice thickness in March 2007.

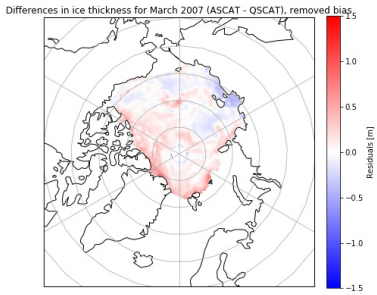

Figure 4.17: Residuals of ASCAT - QuikSCAT in March 2007.

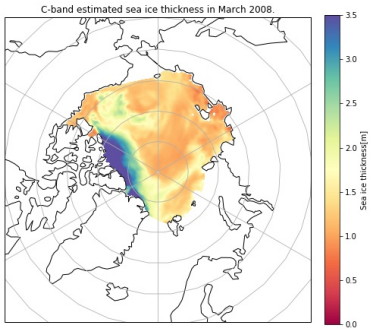

Figure 4.18: ASCAT (C-band) Arctic sea ice thickness in March 2008.

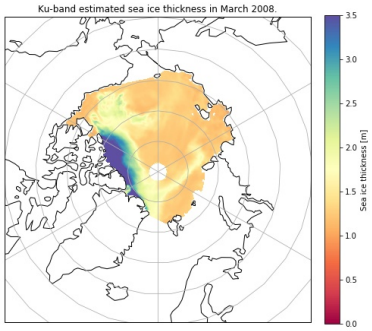

Figure 4.19: QuikSCAT (Ku-band) Arctic sea ice thickness in March 2008.

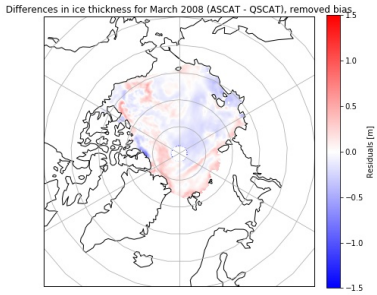

Figure 4.20: Residuals of ASCAT - QuikSCAT in March 2008.

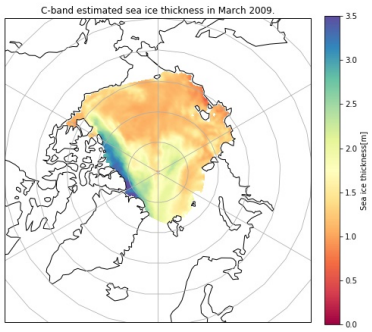

Figure 4.21: ASCAT (C-band) Arctic sea ice thickness in March 2009.

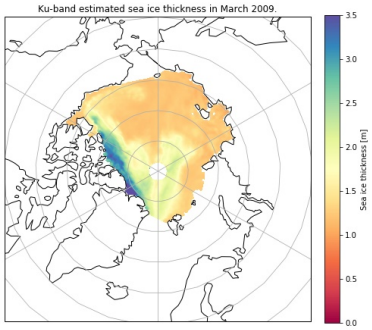

Figure 4.22: QuikSCAT (Ku-band) Arctic sea ice thickness in March 2009.

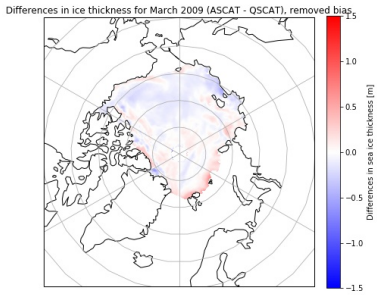

Figure 4.23: Residuals of ASCAT - QuikSCAT in March 2009.

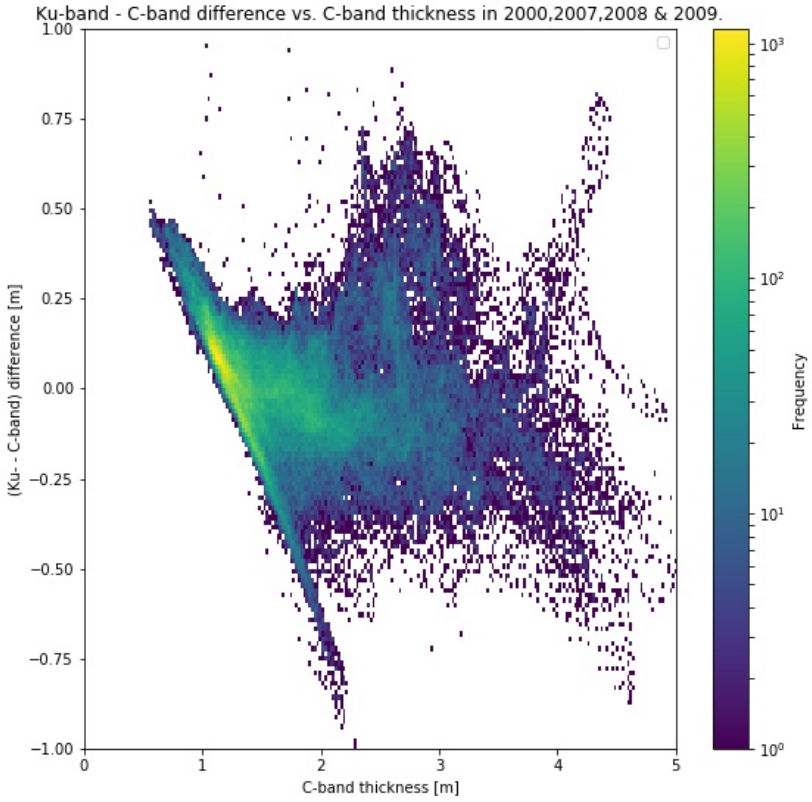

Figure 4.24: C-band sea ice thickness vs. Ku-band - C-band residuals after bias (0.55 m) removal.

The final wintertime scatterometer sea ice thickness estimation models for Ku-band and C-band are shown in figure 4.11. It contains the C- and Ku-band models, where σ^0 is on the y-axis and sea ice thickness on the x-axis. The plot informs on the sensitivity of the different frequencies to thickness. It also allows determination of equivalent thickness thresholds for the backscatter-based ice class thresholds given in Belmonte-Rivas et al. (2018). The equivalent thickness thresholds derived from 4.11 are shown in table 4.6. The red line indicates the C-band thickness, whereas the blue line indicates Ku-band thickness. The slope of the curves, $\frac{d\sigma}{dh}$, can be regarded as the sensitivity of backscatter to sea ice thickness, per frequency. This figure shows that the Ku-band model has a high slope the FYI region, but saturates (low $\frac{d\sigma}{dh}$) in thick ice regimes. This implicates that the Ku-band will have issues estimating thick sea ice thickness, since a small variation in backscatter will lead to a significantly different sea ice thickness estimate. The C-band relationship shows opposite behaviour, having a low sensitivity $\frac{d\sigma}{dh}$ in the thin ice regime, but it has a significantly higher value of $\frac{d\sigma}{dh}$ in the thick ice regime than the Ku-band model. Therefore, the C-band relationship is more sensitive to high backscatter and is thus better at estimating MYI sea ice thickness.

The spatial distribution of residuals between the C- and Ku-band estimates are given in figures 4.14, 4.17 ,4.20 and 4.23, where the bias has been removed from the C-band estimates. Figures 4.12, 4.15, 4.18 and 4.21 show the corrected C-band estimates in the same month. Similarly, figures 4.13, 4.16, 4.19 and 4.22 shows the Ku-band wintertime sea ice thickness. The analysis of spatial distribution of scatterometer to altimeter sea ice thickness errors is given in 4.3.2.

Figure 4.24 shows the distribution of K-band versus C-band sea ice thickness estimates as a function of sea ice thickness, showing that the RMS agreement between the scatterometer models is within 15 cm (1 sigma, see also top row in 4.10) regardless of thickness, that is, their internal agreement is better than the agreement to the altimetry references, and that there are not significant signs of model

shape errors.

For the reasons already mentioned above (i.e. the ICESat record was taken as an absolute reference because it is better tied to the historical sonar and EM survey records), the observed bias for the C-band estimate will eventually be removed from all further C-band estimates on grounds of consistency.

Table 4.6: Sea ice class backscatter and thickness thresholds.

	FYI	**old MYI**
C-band threshold [dB]	<-18.3	>-15
Ku-band threshold [dB]	<-14.5	>-10
C-band thickness [m]	1.58	2.24
Ku-band thickness [m]	1.50	2.26
Class thickness threshold [m]	1.54	2.25

4.3. Error analysis

4.3.1. Methodology

The geographic distribution of systematic differences between QuikSCAT/ICESat and ASCAT/CryoSat-2 can also be analysed in order to look for correlations with processes that may constitute sources of systematic error in the estimation of wintertime sea ice thickness using backscatter. The focus here lies on finding physical processes that help identify and explain systematic backscatter-to-altimeter based sea ice biases. This is done separately for the Ku-band estimate + ICESat and for the C-band estimate + CryoSat-2, since both relationships rely on different training data and operate at a different frequency. The physical parameters that have been investigated are:

1. Snow depth
2. Divergence/convergence of sea ice velocity field
3. Sea ice shear

Convergence and shear of the sea ice velocity field can cause ridging of the sea ice, whereas a snow layer on top of the ice gives different reflective properties of the surface at C- and Ku-band (Kim et al., 1984). Snow depth and surface deformation are particularly interesting, since these are processes that can potentially change the backscatter signature of sea ice, without there being any change in underlying ice thickness. Note that sea ice convergence is used as an indication of surface deformation with associated thickening of ice by compression. Sea ice shear is also indicative of surface deformation, but not associated with thickening unless convergence occurs simultaneously.

Snow depth information has been extracted from PIOMAS. Divergence and shear has been derived from the NSIDC sea ice velocity field (ux,vy) instead, such that it is provided in the grid coordinates instead of north- and eastward velocities (u,v). Note that no information for March 2017 was available at the time of writing for the sea ice velocity field, thus the derived parameters for shear and divergence are missing for this year.

Residuals between the empirical relationships and truth data are defined as $e = d_{est} - d_{truth}$, where d_{est} is the C- or Ku-band estimated sea ice thickness and d_{truth} is the sea ice thickness from ICESat or CryoSat-2.

The Pearson correlation coefficients between the predicted and actual values of the dependent variable (sea ice thickness residuals) will be used using a multiple regression model that includes convergence, shear and snow depth as independent variables. The multiple correlation analysis is made difficult by the fact that the independent variables (convergence, shear and snow depth) are not really independent. In fact, it is observed that the effect of one variable (e.g. shear) on the backscatter-based sea ice thickness errors depends on the state of the other variables (e.g. whether there is also convergence in the background sea ice field), making it a non-linear problem that is difficult to treat with a basin-wide approach, but is easier to handle regionally. Hence, multiple correlations regression results are calculated basin-wide and per Region of Interest (ROI).

The correlations analyses are based on a multiple linear regression as defined in equation 4.10. Parameter y are the period means of the residuals, whereas x_1, x_2, x_3 are the period means of the parameters of interest: snow depth, divergence and shear. In this multiple linear regression, period means will be used for Ku-band as the mean of (2003-2007), whereas for C-band it will be the mean of the period (2011-2016). These calculations were done basin-wide, in ROI1 and ROI2. ROI1 includes the Beaufort Gyre, a wind-driven ice drift characterized by rotational motion with high shear and low convergence. ROI2 includes the Fram Strait located at the end of the Transpolar Drift Stream, which transports sea ice from the Siberian Sea and is characterized by large sea ice convergence. The geographical limits of the ROIs are given in table 4.7. Correlations resulting from this multiple linear regression are of interest, since from here the amount of variance in the residuals caused by a parameter can be quantified as $\frac{\sigma_n^2}{\sigma_{residuals}^2}$. σ_n^2 is the variance of the different terms resulting from equation 4.10.

$$y = ax_1 + bx_2 + cx_3 \tag{4.10}$$

Table 4.7: ROIs bounding boxes in degrees latitude (N/S) and degrees longitude (W/E).

	N	S	W	E
ROI 1: Beaufort	77	72	180	230
ROI 2: Fram Strait	88	82	60	40

4.3.2. Results and discussion

Initially, the spatial distribution of residuals (scatterometer versus altimeter) averaged over the respective collocation periods at C-band and Ku-band will be presented, which are obtained after using the relationships found in section 4.1.2. Afterwards, the residuals are compared with several geophysical parameters in order to look for physical processes that may explain systematic differences between scatterometer and altimeter estimates. Sections 4.3.2 and 4.3.2 contain the obtained results from this analysis for Ku- and C-band, respectively.

Ku-band error analysis

Residuals

The residual sea ice thickness can be calculated after using the equations found in section 4.1.2 together with the training data of ICESat. The residual thickness is defined as $d_{res} = d_{Ku-band} - d_{ICESat}$, with $d_{Ku-band}$ the Ku-band sea ice thickness and d_{ICESat} the ICESat sea ice thickness. Yearly residuals in the collocation period (2003-2008) are presented in figures F.4 to F.9. Yearly values for the parameters of interest are plotted on a PS12.5 grid in Appendix E. Figures 4.25 to 4.28 show the average (2003-2008) of the residuals, shear, convergence and snow depth in the Arctic. The RMSE of the (Ku-band - ICESat) residuals, which is a measure of the magnitude of the geographic standard deviation of systematic error between the two sources, was found to be 0.30 m during (2003-2008).

Blue areas in figure 4.25 indicate areas where the Ku-band underestimates the sea ice thickness in comparison with ICESat, whereas red areas indicate overestimation by the Ku-band relationship. Blue regions in figure 4.26 and 4.28 indicate areas with high shear / snow depth, where red regions show areas with low shear / snow depth. Blue regions in figure 4.27 show areas of convergence ($\nabla(ux, vy) < 0$), whereas red regions show divergent zones ($\nabla(ux, vy) > 0$). This description is also valid for the yearly parameters shown in Appendix E.

The period means and yearly patterns show some interesting features. A pattern of overestimation can be observed in the Beaufort Gyre and Chukchi seas, which is possibly related to large shear in these areas (ROI1). The residuals show mean patterns of underestimation of sea ice thickness compared to ICESat in the Fram Strait and in the Laptev sea. The Fram Strait is mostly covered with SYI/MYI during 2003-2008 and it experiences strong sea ice convergence. The Laptev Sea is mainly covered with new, undeformed FYI. The overestimated areas are mainly located in the Beaufort Gyre and the Chukchi seas, which are regions experiencing relatively high sea ice shear.

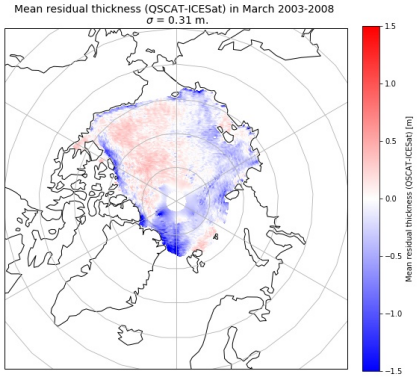

Figure 4.25: Mean residuals (QuikSCAT-ICESat) during (2003-2008).

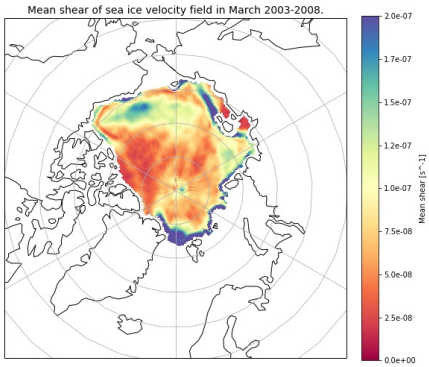

Figure 4.26: Mean shear during (2003-2008).

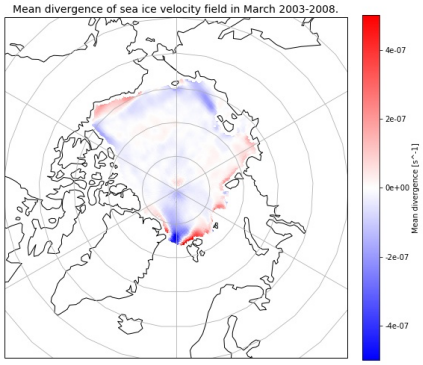

Figure 4.27: Mean convergence (from sea ice velocity field) during 2003-2008.

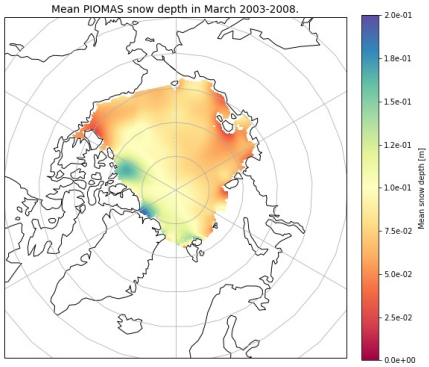

Figure 4.28: Mean PIOMAS snow depth during 2003-2008.

Ku-band geophysical error analysis

Correlation between the residuals (QuikSCAT estimate - ICESat reference) has been calculated using collocated data of PIOMAS snow depth and the divergence + shear of the sea ice velocity field from the NSIDC sea ice motion vectors. The correlation has been calculated using multiple linear regression, as described in section 4.3. This has been done for three regions: the Arctic basin, ROI 1 (Beaufort) and ROI 2 (Fram Strait). These ROIs have been chosen based on the yearly parameter plots in Appendix E. The regions of interest were selected after observing overestimation patterns in the Beaufort Gyre and Chukchi sea and after observing underestimation in the Fram Strait, (section 4.3.2). The results are shown in table 4.8, together with the amount of variance a certain parameters explains in the total variance of the residuals during (2003-2007).

Table 4.8: QuikSCAT correlations reported per ROI per parameter, noted as correlation / percentage of total variance explained.

	Basin-wide	**ROI 1 - Beaufort**	**ROI 2 - Fram**
Shear	-0.36 / 10%	0.31 / 11%	-0.46 / 17%
Convergence	-0.35 / 8%	0.06 / 1%	-0.64 / 32%
Snow depth	-0.01 / 0%	0.21 / 8%	-0.24 / 5 %
Total	0.49 / 19%	0.42 / 16%	0.81 / 55 %

The year 2008 is particularly interesting when comparing the behaviour of backscatter estimated sea ice thickness with ICESat. Figures F.8, F.9,4.14, 4.17,4.20 and4.23 show the residuals between the Ku-band estimate with ICESat and the residuals between C- and Ku-band, respectively. Neither the C- or Ku-band observations sense a drop in sea ice thickness (or backscater) in 2008, like the ICESat reference does. A previous study (Tschudi et al., 2016b) on using sea ice age as a thickness proxy noted a similar discrepancy in 2008 and proposed that older ice (higher age) may have undergone extremely large subsurface melting in 2008 as an explanation. The observations in this study may be indicative of problems with the estimation of wintertime sea ice thickness using backscatter under conditions such as heavy subsurface melt, but may also be indicative of a problem with the ICESat reference in 2008.

The results of multiple linear regression provided correlation values of the regions of interest (basin, ROI1 and ROI2) and the amount of variance that is explained by these parameters, as shown in table 4.8. Note that the year 2008 has been excluded in these calculations.

The analysis of correlations between sea ice thickness residuals and the proposed variables (convergence, shear and snow depth) that come out from a multiple regression model indicate that basin-wide there is appreciable Ku-band sea ice thickness underestimation (with moderate negative correlations) due to sea ice convergence and shear. These results are interpreted as the effect of compression in creating actually thicker (but not proportionally brighter) sea ice in areas such as the Fram Strait and the Siberian Sea. Thickness underestimation is particularly accentuated in the Fram Strait (ROI2), where strong negative correlations to exceptionally large sea ice convergence and shear explain up to 55 % of the variance in thickness error. The case of overestimation of ice thickness in the Beaufort Sea and the Central Arctic using the Ku-band estimation relationship needs to be looked at separately. In this case (ROI1), moderate positive correlations to shear (without convergence) and snow seem to suggest that these processes are playing a role in increasing surface backscatter without there being an increase in ice thickness. There is a dual role that sea ice shear appears to be playing when it comes to explain the nature of biases in scatterometer-based sea ice thickness estimation, as it may either explain under or overestimation, depending on whether the increase in backscatter associated with surface deformation (under shear) comes with or without a thickening of the underlying ice slab, which is determined by the amount of convergence in the ice field.

C-band error analysis

Residuals

The residual sea ice thickness can be calculated after using the equations found in section 4.1.2 together with the training data of CryoSat-2. The residuals are defined as $d_{res} = d_{C-band} - d_{CS-2}$ and can be calculated for each year in 2011-2017 and as a periodic mean (i.e. the mean of the parameter during 2011-2017). Note that there was no data available for 2017 for the sea ice velocity derived parameters, thus excluding these years in the period means. Yearly residuals in the collocation period (2011-2017) are presented in figures F.10 to F.16. Yearly values for the parameters of interest are plotted on a PS12.5 grid in section E. Figures 4.29 to 4.32 show the periodic means of the residuals, shear, convergence and snow depth in the Arctic. The RMSE of the (C-band - ICESat) residuals was found to be 0.30 m during (2011-2017).

Overall, a systematic pattern of C-band sea ice thickness error arises that is similar to that of Ku-band thickness estimates, with overestimation of sea ice thickness in the Beaufort Gyre, which might be shear related and underestimation in the Fram Strait, which might be related with sea ice convergence. Besides from this, a pattern of overestimation in the marginal seas (Laptev/Kara/Barents) can be observed. Figures F.10 to F.16 indeed show systematic overestimation of scatterometer sea ice thickness when compared with the reference data (CryoSat-2), particularly at the margins in the east of the basin, in the Laptev/Kara/Barents Seas.

Figures 4.29, 4.30, 4.31 and 4.32 show mean values for (C-band - CryoSat-2) residuals, sea ice shear, convergence and snow depth during 2011-2016, since no ancillary data data was available on the sea ice velocity field in 2017. Systematic errors can be observed again, similar to the Ku-band relationship. Thickness overestimation occurs in the Beaufort Gyre and Chukchi Sea, a large shear area and thickness underestimation in the Fram Strait, an area with high convergence and relatively high snow depth. Also, the marginal seas (Laptev/Kara/Barents) show signs of overestimation by the C-band relationship. The backscatter figures in figure A.3 show a presence of rough ice, thus a high backscatter signal. This is likely to be the cause of overestimation in these regions.

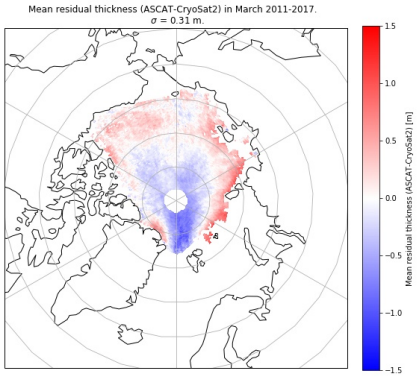

Figure 4.29: Mean residuals (ASCAT-CS2) during 2011-2017.

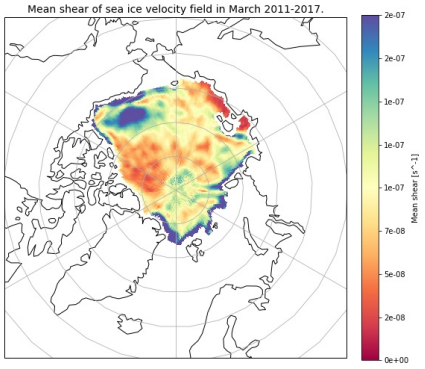

Figure 4.30: Mean shear during 2011-2016.

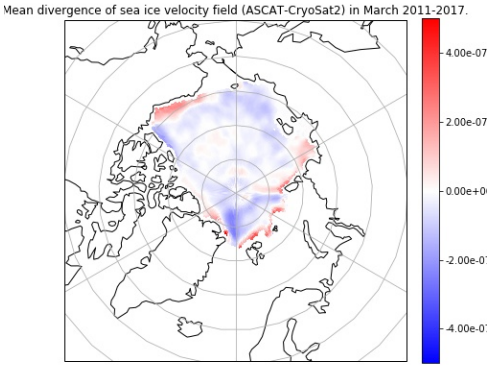

Figure 4.31: Mean convergence (from sea ice velocity field) during 2011-2016.

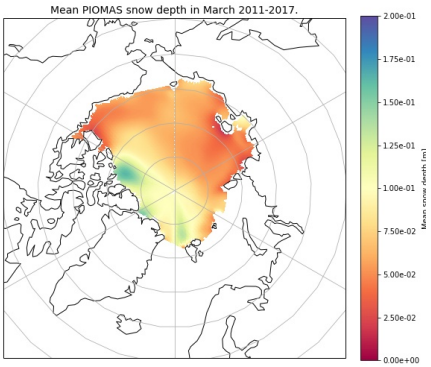

Figure 4.32: Mean PIOMAS snow depth during 2011-2017.

C-band geophysical error analysis

Multiple correlation coefficients between the residuals (ASCAT estimate - CryoSat-2 reference) and several independent variables (convergence, shear and snow depth) have been calculated using collocated data of PIOMAS snow depth and the divergence + shear of the sea ice velocity field from the NSIDC sea ice motion vectors. The correlation has been calculated using multiple linear regression, as described in section 4.3. This has been done for three regions: the Arctic basin, ROI 1 (Beaufort) and ROI 2 (Fram Strait). The results are shown in table 4.9, together with the amount of variance a certain parameters explains in the total variance of the residuals during (2011-2016). 2017 has been excluded from these calculations as no ancillary data was available at the time of writing, except for PIOMAS snow depth.

The most striking feature arising from the correlation analysis shown in table 4.9 is a very strong basin-wide negative correlation with snow depth, meaning that the C-band model is underestimating thickness under heavy snow loads. This result is difficult to interpret physically for two reasons. Firstly, snow is generally expected to increase surface backscatter without increasing ice thickness (thus resulting in overestimation of sea ice thickness, as observed in the Ku-band case). Secondly, the effect of snow on C-band estimates is expected to be much smaller than at Ku-band, since the volume scattering response of the snow grains decreases with wavelength. At this point, we conjecture that the anomalous negative correlation of thickness differences with snow depth at C-band may be attributed to a problem with the CryoSat-2 reference. Actually, preliminary investigations (Ricker et al., 2015) report positive correlations between CryoSat-2 thickness estimates and snow load. In order to clarify this matter, the residuals of ASCAT relative to CryoSat-2 have been plotted against the PIOMAS snow depth in Figure 4.33, and additional correlations have been calculated as a function of sea ice class/thickness using the thresholds defined in table 2.2. Figure 4.33 shows that the negative correlations observed at C-band are consistent with CryoSat-2 estimates that are biased high under heavier snow loads, as reported in Ricker et al. (2015), and that the effect of snow load in the C-band to CryoSat-2 differences is also a function of sea ice type, with MYI being the least affected.

Table 4.9: ASCAT correlations reported per ROI per parameter, noted as correlation / percentage of total variance explained.

	Basin-wide	**ROI 1 - Beaufort**	**ROI 2 - Fram**
Shear	0.22 / 0%	0.25 / 3%	0.38 / 0%
Convergence	-0.35 / 7%	-0.14 / 0%	-0.60 / 25%
Snow depth	-0.45 / 16%	-0.42 / 15%	-0.44 / 11 %
Total	0.54 / 27%	0.47 / 21%	0.69 / 35 %

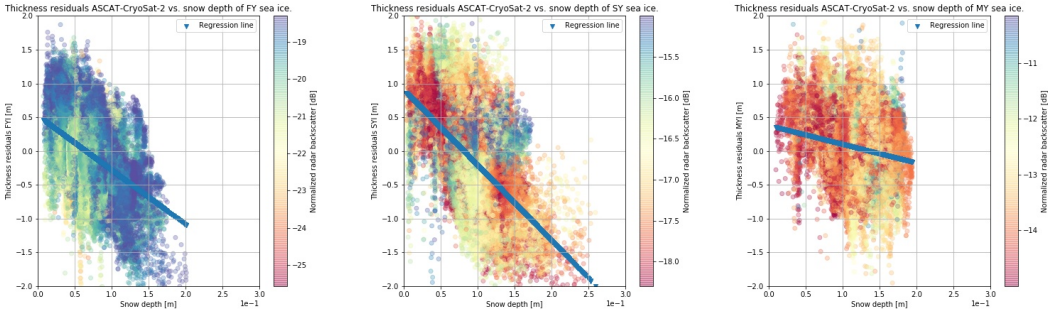

(a) FYI, correlation coefficent R=-0.44.

(b) SYI, correlation coefficent R=-0.61.

(c) MYI, correlation coefficent R=-0.21.

Figure 4.33: Residuals (ASCAT - CS2) versus PIOMAS snow depth [m] per sea ice age class.

Other than the negative correlations to snow depth, which explain up to 15% of the variance in thickness errors, two other processes appear to bear an imprint on the C-band thickness estimates. In the first place, sea ice convergence (with a strong negative correlation) appears to be the main cause of underestimation in the Fram Strait (ROI2), explaining up to 25% of the thickness error there. Then, sea ice shear (with a moderate positive correlation) appears to be the main cause of overestimation in the Beaufort Sea (ROI1). These results are in line with those obtained for the Ku-band case, supporting the interpretation that increases in backscatter due to surface deformation with (case of convergence) or without (case of shear) thickness accretion are the main sources of systematic error in estimation of sea ice thickness using backscatter as proxy.

Figure 4.33 shows the C-band residuals plotted against the snow depth. The 3 panels indicate FYI/SYI/MYI sea ice age classes based on the backscatter thresholds in table 2.2. Correlation values R are -0.44/-0.61/-0.21 for these classes, respectively.

5

Historical record 1992-2017

This chapter uses the empirical Ku-band and C-band relationships derived in chapter 4. The C-band relationships were applied to C-band backscatter measurements made by ERS and ASCAT, while the Ku-band relationship was applied to the Ku-band, VV polarized QuikSCAT backscatter measurements. Combining the scatterometer sea ice thickness estimates gives a historical record of wintertime sea ice thickness dating from 1992 - 2017. The previously discussed thickness thresholds (table 4.6) were used to classify the sea ice into distinct ice classes (FYI, SYI and MYI) and to create a record for these distinct ice classes during the same period.

Section 5.1 explains the methodology used in deriving the historical record, the results are presented and discussed in section 5.2.

5.1. Methodology

A historical sea ice thickness record for wintertime (March) sea ice thickness can be produced for 1992-2017 by using the C- and Ku-band relationships in combination with the backscatter record. The C-band relationship was therefore be extended to ERS scatterometer data, since it also operates at C-band.The mean sea ice thickness may be calculated for the study area and linear regression using all available scatterometer sea ice thickness information will be used to provide a mean growth/decline rate of wintertime Arctic sea ice thickness.

Furthermore, a mean sea ice thickness can also be calculated per sea ice age class by using the backscatter thresholds provided in table 4.6.

5.2. Results and discussion

The mean Arctic sea ice thickness was calculated every March in the period of 1992-2017 in the area limited by the geographic mask. The results for each estimate together with the ICESat reference and the AWI CS-2 thickness product are shown in figure 5.1. Note that the same bias has been removed from the AWI CS-2 reference product as from the C-band estimate, as a result of the consistency check between the C-band and Ku-band models and references. This figure is similar to figure 1.2, but the newly created record shows the homogenization of the altimeter records has been achieved by using the scatterometer-based thickness record. The standard deviation of the residuals of mean Arctic sea ice thickness for the (Ku-band-ICESat) σ_{Ku} and (C-band - CryoSat-2) σ_C collocation periods has been calculated and are 0.16 and 0.07 m, respectively. The full record can be found in Appendix F. Figures F.1, F.2 and F.3 show the estimated sea ice thickness of the ERS-1/2, QuikSCAT and ASCAT missions yearly in March.

Subsequently, the area has been divided into FYI/SYI/MYI classes using the thickness thresholds noted in table 4.6. The mean sea ice thickness per class can then be calculated for the scatterometer datasets. These are shown in figure 5.2. The upper panel shows the mean thickness of first year ice, the middle panel shows the mean thickness of second year ice and the lower panel shows the evolution of older multi-year sea ice thickness.

Finally, using all March scatterometer estimates and performing linear regression, a mean rate

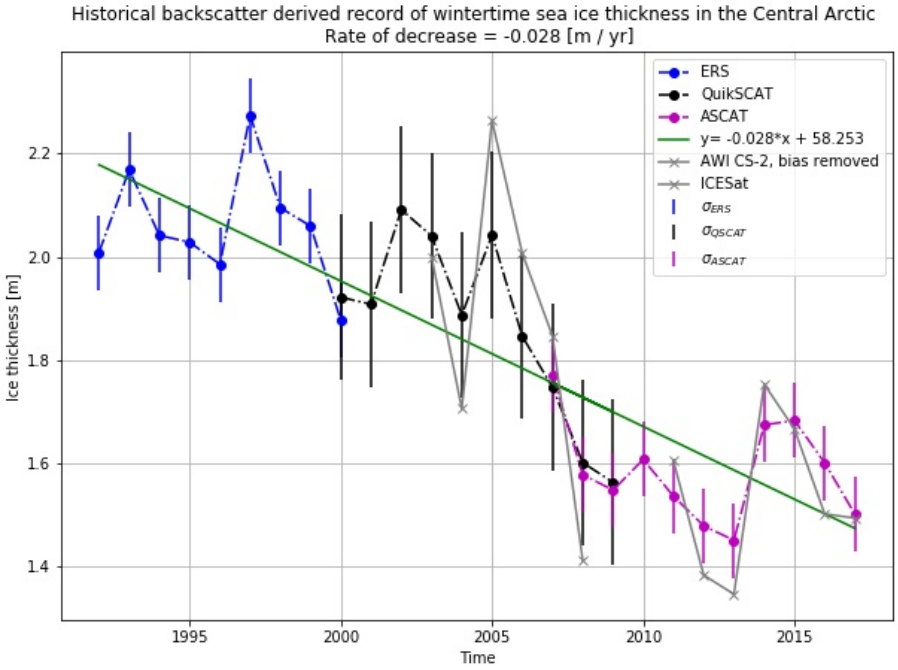

Figure 5.1: Historical record of mean Arctic sea ice thickness (1992-2017) and linear regression

of wintertime Arctic sea ice thickness decline of -0.28 m per decade was found. Figure 5.1 shows the interannual variability of mean sea ice thickness over the years together with the result of linear regression. Note that x is the year of interest, with a range of [1992-2017] and y is the mean sea ice thickness. The slope of this line is equal to the rate of growth/decrease of mean sea ice thickness in the Arctic.

The mean March sea ice thicknesses were calculated in the Arctic basin and are shown in given figure 5.1, together with the ICESat and CryoSat-2 references.This figure shows reasonable agreement with the thickness variability in the altimetry datasets of ICESat and CryoSat-2.

The overlap years (2000, 2007, 2008, 2009) show reasonable overlap with each-other (C-band + Ku-band). 2008 shows that the scatterometer datasets senses a higher mean sea ice thickness than ICESat. The overlap period (2011-2017) of ASCAT - CryoSat-2 show good overlap with each other, whereas (2003-2008) shows a slightly higher deviation between (QuikSCAT - ICESat) than (ASCAT - CryoSat-2).

Figure 5.2 shows the evolution of FYI, SYI and MYI in 1992-2017, based on the class thickness thresholds reported in table 4.6. The figure shows that there is no clear trend in FYI. It shows that first year ice (<1.54 m) looks thinner at C-band than at Ku-band, with differences in the range of 5 to 10 cm. Large uncertainties are observed in this sea ice age class, also between CryoSat-2 and ICESat. Figure 4.24 already showed a small disagreement between the C- and Ku-band estimates, which likely is the cause of the disagreement between the C- and Ku-band estimates . Note that since the disagreement in figure 4.24 was only 0.15 m (1-sigma), an empirical correction seemed not necessary, but is likely the cause of the disagreement in figure 5.2 as well. The middle panel shows the evolution of the SYI class. The thickness of SYI shows decline in this class.

The MYI ice age class shows the largest variability, since this ice age class is most vulnerable to seasonal effects and sea ice dynamics occurring outside of the winter period. The ICESat reference record shows a large decrease in mean old MYI thickness (>2.25 m) ice in 2008, whereas the Ku-band estimates register a slight increase and no appreciable change is observed at C-band.

Note that the record of mean sea ice thickness figure 5.1 for the entire Arctic basin registers a large drop in 2008, not caused by a decrease in the mean thick ice thickness, according to our records, but rather because the spatial extent of the thicker old MYI ice class suffers a remarkable decrease in 2008.

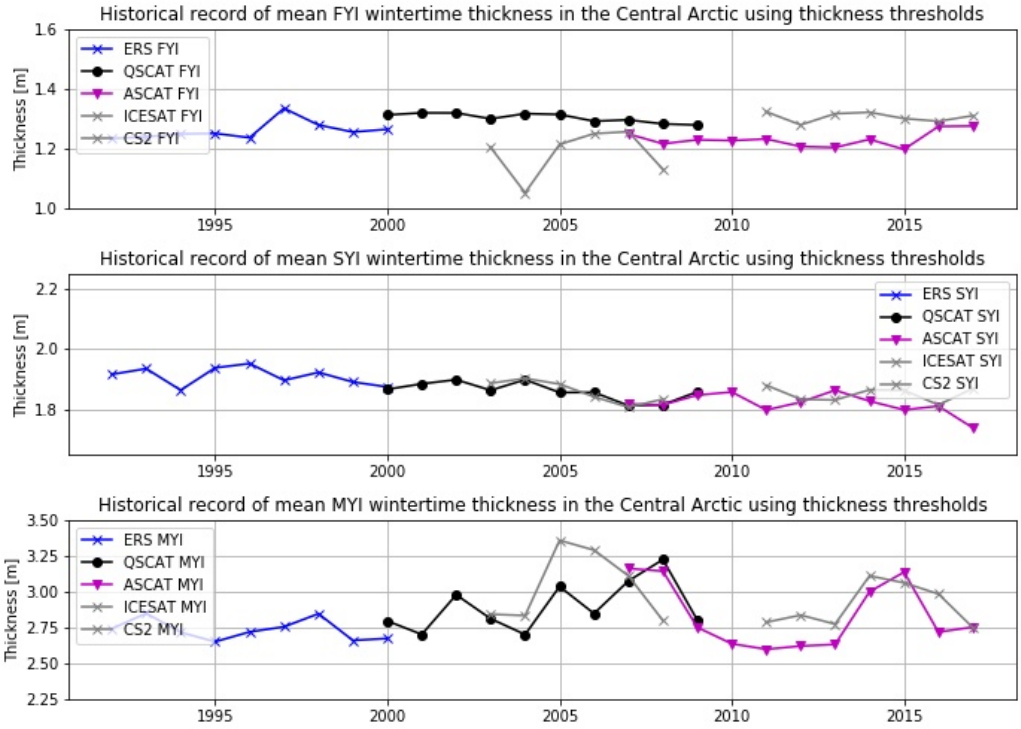

Figure 5.2: Historical record of mean Arctic sea ice thickness (1992-2017) per sea ice age class.

In other words, the extent of MYI may influence the basin-wide mean thickness, since a large loss of thick ice area extent will decrease the mean thickness basin-wide. Thus, by using a thickness based threshold, the mean thickness of MYI may still be high, but a loss of area fraction influences the basin-wide mean thickness greatly. Figure 1.3 indeed shows a decrease of area fraction of MYI (3+ years) in 2007, which in turn replaced by newly formed, thinner FYI, having a larger area fraction after 2007. Similarly to figure 1.3, figure 5.3 also shows a time series of monthly wintertime (March) sea ice extents (Belmonte-Rivas et al., 2018) showing the same strong decline in older MYI sea ice extent in 2008.

2014 shows a strong increase in mean sea ice thickness in figure 5.1 and also in figure 5.2 in the MYI class. In this case, a thickening of thick ice can be seen in the MYI class, directly affecting the basin-wide mean sea ice thickness. Kwok (2018) stated that the cause of this increase in thick ice was caused by a record extreme in ice convergence north of the Canadian Arctic archipelago and the Greenland coast, in addition with cooler summer air temperatures.

Figure 5.1 shows the scatterometer estimates together with an indication of the error, defined as the standard deviation between the (Ku-band - ICESat) / (C-band - CryoSat-2) mean sea ice thickness residuals from this plot, noted as σ_{Ku} and σ_C. The green line notes the trend, a result of linear regression between all March scatterometer estimates during (1992-2017). The trend shows that the wintertime sea ice thickness is decreasing with 0.28 m / decade.

Backscatter measurements at Ku- and C-band show a drastic decrease in areas with high σ^0 from 2007 onward, especially visible in Ku-band measurements, as seen in Appendix A. A reduction of thick ice near the Canadian Arctic archipelago and Greenland coast is also visible in the ICESat reference thickness in figure B.1. Similarly, the year 2014 shows an increase in backscatter compared to 2013, visible in figure A.3. An increase in sea ice thickness in 2014 is also observed in the CryoSat-2 reference sea ice thickness plot in figure B.2.

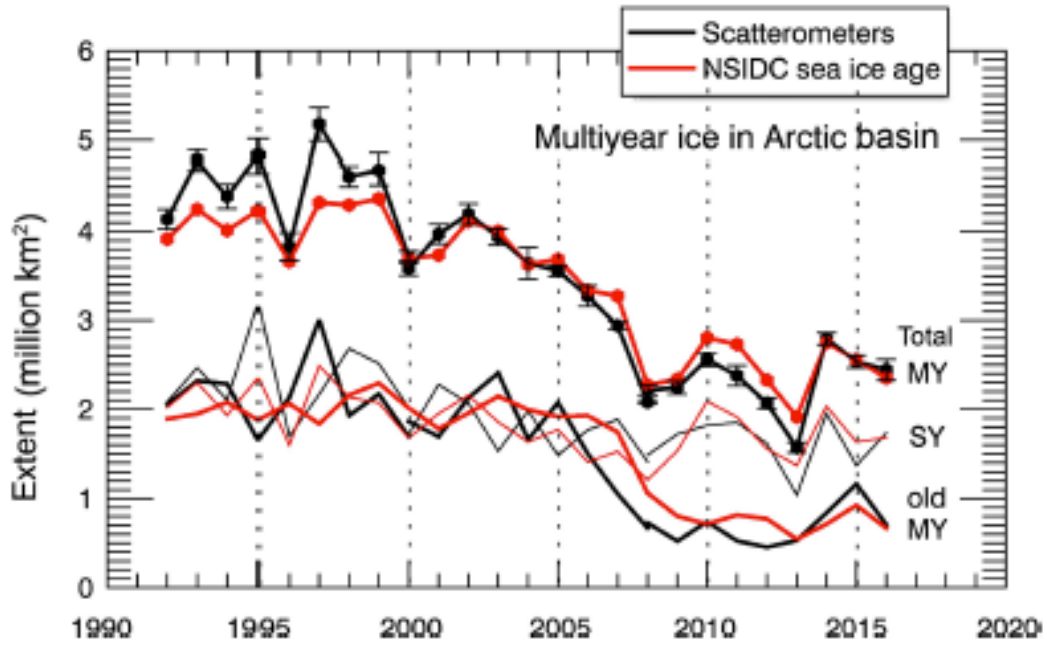

Figure 5.3: Time series of monthly wintertime (March) sea ice extent, classified as SYI and older MYI in the Arctic basin from scatterometer record (black) and the NSIDC sea ice age record (red) (Belmonte-Rivas et al., 2018).

6

Conclusions and Recommendations

In this chapter, the conclusions on the main research question and sub questions will be presented in section 6.1 and suggestions for future research are proposed in section 6.2.

6.1. Conclusion

This thesis explored the possibility of estimating wintertime (March) Arctic sea ice thickness by using normalized radar backscatter measurements from satellite scatterometers. The conclusions are organised as such that they relate to the main question and to the subquestions that were introduced in chapter 1. The conclusions are divided into subchapters, each of which relate to a specific (sub)question. Section 6.1.1 deals with the initial fits, whereas sections 6.1.2 and 6.1.3 deal with the questions on consistency and the error analysis, respectively. Finally, the questions dealing with the newly derived wintertime scatterometer sea ice thickness record are given in section 6.1.4.

6.1.1. Empirical fits

What is the empirical relationship between wintertime (March) Arctic sea ice thickness and σ^0 at C- and Ku-band?

An empirical relationship for C- (ASCAT/ERS) and Ku-band (QuikSCAT) scatterometers has been determined after using collocated sea ice backscatter and sea ice thickness measurements (QuikSCAT - ICESat & ASCAT - CryoSat-2). The collocated data for Ku-band consisted of QuikSCAT and ICESat collocated measurements during 2003 - 2008, whereas for C-band is consisted of collocated ASCAT and CryoSat-2 measurements during 2011-2017. Both datasets were masked to obtain measurements of the Arctic basin, to filter the high-backscatter response of deformed FYI in the marginal ice zone. The empirical relationships for C-band was $\bar{d}_i = 30.41 \cdot e^{0.21\sigma^0} + 2.39 + 0.05\sigma^0$, whereas the functional Ku-band relationship was reported to be $\bar{d}_i = 44.24 \cdot e^{0.42\sigma^0} + 1.76 + 0.04\sigma^0$. The uncertainties of the C- (0.47 m) and Ku-band (0.48 m) relationships are similar to previously reported ICESat and CryoSat-2 altimetry uncertainty estimates.

6.1.2. Consistency check

What is the consistency of the empirical relationships when they are applied?

The empirical relationships were checked for consistency during mission overlap years 2000, 2007, 2008 and 2009. C-band sea ice thickness estimates proved to be consistently higher than the Ku-band sea ice thickness estimates and were also found to be higher than the ICESat reference sea ice thickness during the mission overlap years. The observed bias in the C-band estimates has been calculated by using a weighted average of the mean differences between C-band estimates and Ku-band estimates/ICESat reference. The bias was found to be 0.55 m and was removed from both the C-band

estimate as the CryoSat-2 reference. After removing the bias from the C-band estimates, the C- and Ku-band estimates agreed with each other within 0.15 m. The bias has also been removed from the AWI CS-2 sea ice thickness product, as the provided high sea ice thickness estimates during mission overlap years.

Subsequently, new sea ice thickness thresholds were established by using backscatter based ice class thresholds together with the empirical relationships. These new thresholds were used to classify sea ice as either FYI, SYI or MYI. First-year ice in March is classified as thinner than 1.54 m, SYI ice is classified as sea ice with a thickness between 1.54 and 2.25 m and older multi-year ice will be classified as such when the sea ice thickness is larger than 2.25 m.

6.1.3. Error analysis

Under which conditions are these relationships valid and what are the limitations and error sources?

Analysis of the residuals with physical parameters showed that the Ku-band estimates are prone to underestimation in cases of strong sea ice convergence (e.g. in the Fram Strait) and overestimation in cases of strong shear and high snow loads (e.g. in the Beaufort Sea). Similarly, the C-band estimates also showed that convergence has more impact in the Fram Strait and shear in the Beaufort Sea. Thickness underestimation at both C- and Ku-band (Fram Strait) is interpreted as an effect of compression (due to convergence and shear), causing thicker (but not proportionally brighter) sea ice. Overestimation of sea ice thickness at Ku-band is interpreted as a combined effect of snow and shearing (without convergence), as these processes increase the surface backscatter, but without there being an increase in sea ice thickness. Note that shear plays a dual role: it may explain both under- and overestimation of the sea ice thickness depending on whether the increased backscatter due to surface deformation comes with or without thickening of the ice slab. Similar results were found at C-band, supporting the interpretation that an increase of surface backscatter due to surface deformation with (in case of convergence) or without (case of shear) thickness accretion are sources of systematic error when using normalized radar backscatter as an Arctic, wintertime sea ice thickness proxy.

A strong dependence of thickness errors on snow depth has been detected at C-band, which is considered unphysical and therefore attributed to the problems with the CryoSat-2 reference. Lastly, systematic overestimation patterns at C-band in the Kara/Laptev/Barents Seas are caused by rough ice with a high backscatter response.

6.1.4. Historical record

How does the scatterometer based Arctic mean wintertime sea ice thickness evolve from 1992 to present day?

The C-band relationship was applied to the, at C-band operating scatterometers, ERS and ASCAT backscatter measurements and the Ku-band relationship was applied to QuikSCAT (VV-polarized) backscatter measurements. The combination of the three scatterometers provided an uninterrupted record of Arctic sea ice thickness in March, between 1992-2017, and can be extended since ASCAT is still operational. The newly derived scatterometry sea ice thickness record between 1992-2017 showed that the average Arctic sea ice thickness in the Central basin is decreasing with a rate of -0.28 m / decade. It also showed that the most variability of average sea ice thickness is within the MYI class, whereas the mean SYI thickness shows a steady decline. The FYI record is variable and does not overlap nicely, this difference is inherited from the difference between the C- and Ku-band relationships for thin ice, where a disagreement between the models of 0.15 m (1-sigma) was found reasonable. No corrections were made to solve this difference, but an empirical correction could have prevented this disagreement in the historical record.

It must be also noted that the mean sea ice thickness of FYI/SYI/MYI ice age classes can exhibit different behaviour than the mean sea ice thickness of the entire basin. The mean sea ice thickness in the entire basin can be seen as weighted average of the area fractions of the distinct sea ice age classes. Therefore, a decline or increase in area fraction of one of the classes may result in a lower or higher mean sea ice thickness, respectively.

6.1.5. Final conclusion

How can normalized radar backscatter measured from satellite scatterometers be used to estimate wintertime Arctic sea ice thickness?

This study showed that normalized radar backscatter measurements done with C- and Ku-band can be used to estimate wintertime (March) Arctic sea ice thickness. The subquestion on the empirical relationships showed that collocation of normalized backscatter measurements together with wintertime sea ice thickness data made it possible to determine an empirical relationship between the two parameters at both C- and Ku-band, which is only valid in March. The scatterometer sea ice thickness estimates made with the determined relationships provide sea ice thickness estimates that have similar uncertainties when compared with their references, ICESat and CryoSat-2. This study showed the potential of using normalized radar backscatter as a proxy for Arctic sea ice thickness.

However, the subquestion about the error sources showed that both C- and Ku-band relationships suffer from overestimation/underestimation in the Arctic basin. Systematic overestimation has been observed in the Beaufort Gyre and Chukchi seas at C-band and Ku-band, whereas underestimation of sea ice thickness compared with the reference ICESat measurements was visible in the Fram Strait. Furthermore, at this moment the potential of using normalized radar backscatter as a proxy for sea ice thickness is limited to the month March.

6.2. Recommendations

Normalized radar backscatter has proved to be a good sea ice thickness proxy in the wintertime in this study. The acquired results, describing wintertime Arctic sea ice thickness with a similar precision as altimetry derived sea ice thickness, lead to interesting questions, which require further investigation.

Firstly, the empirical relationships used in this study apply only to March datasets. Therefore, it would be nice to extend the backscatter-thickness relationships to spring and autumn months. The relationships can not be used in this form, since sea ice grows/melts during the seasons, which will both affect the normalized radar backscatter signature due to the existence of melt ponds on top of the ice and sea ice thickness. Furthermore, it can also be used as a tool for estimating past wintertime sea ice thicknesses during periods with limited thickness measurements. An additional follow-up research could be to investigate whether these relationships can be applied to other winter months (December/-January/February) or if these months need a separate analysis due to a different backscatter-thickness relationship, since the sea ice slabs grow during the cold season, but the backscatter response may or may not change, resulting in possibly different empirical relationships.

Secondly, C-band estimates based on CryoSat-2 data have shown to be too high in overlap years, which showed the presence of a high bias in the thickness retrieval algorithm present in CryoSat-2. The launch of ICESat-2 in 2018 provides an opportunity for further validation with a laser altimeter, rather than a radar altimeter such as CryoSat-2.

Finally, this study showed that normalized radar backscatter can be used as a proxy for wintertime sea ice thickness and the continuation of C-band backscatter measurements with the planned launch of the MetOp-C satellite provides a good way of monitoring sea ice thickness in the future.

Bibliography

Arrigo, K., van Dijken, G. and Pabi, S., 2008. Impact of a shrinking arctic ice cover on marine primary production. *Geophysical Research Letters*.

Beaven, S., Lockhart, G., Goginieni, S., Hosseinmostafa, A., Jezek, K., Perovich, D., Fung, A. and Tjuatja, S., 1995. Laboratory measurements of radar backscatter from bare and snow-covered saline ice sheets. *International Journal of Remote Sensing* 16(5), pp. 851–876.

Belmonte-Rivas, M. and Stoffelen, A., 2011. New bayesian algorithm for sea ice detection with QuikSCAT]. *IEEE Transactions on Geoscience and Remote Sensing* 49(6), pp. 1894–1901.

Belmonte-Rivas, M., Otosaka, I., Verhoef, A. and Stoffelen, A., 2018. A scatterometer record of sea ice extents and backscatter: 1992-2016. *The Cryosohere*.

Belmonte-Rivas, M., Verspeek, J., Verhoef, A. and Stoffelen, A., 2012. Bayesian sea ice detection with the advanced scatterometer ASCAT. *IEEE Transactions on Geoscience and Remote Sensing* 50(7), pp. 2649–2657.

Bolstad, W., 2009. *Introduction to Bayesian statistics*. John Wiley and Sons.

Calafat, F., Cipollini, P., Bouffard, J., Snaith, H. and P., F., 2017. Evaluation of new CryoSat-2 products over the ocean. *Remote Sensing of Environment* 191, pp. 131–144.

Comiso, J., 2010. *Fundamental characteristics of the polar oceans and their sea ice cover, chapter in Polar Oceans from Space.* Springer.

Comiso, J., 2012. Large decadal decline of the arctic multiyear ice cover. *Journal of Climate* 25, pp. 1176–1193.

Cox, G. and Weeks, W., 1974. Salinity variations in Sea Ice. *Journal of Glaciology* 13(67), pp. 109–120.

Deser, C., Walsh, J. and Timlin, M., 2010. Arctic sea ice variability in the context of recent atmospheric circulation trends. *Journal of Climate* 13(3), pp. 617–633.

Drinkwater, M. and Liu, X., 2000. Seasonal to interannual variability in antarctic sea ice surface melt. *IEEE Transactions on Geoscience and Remote Sensing*.

ESA, 2019. CryoSat-2 Geographical Mode Mask 3.0.

Ezraty, R. and Cavanie, E., 1999. Construction and evaluation of 12.5 km grid NSCAT backscatter maps over Arctic sea ice. *IEEE Transactions on Geoscience and Remote Sensing* 37(3), pp. 1685–1697.

Figa-Saldaña, J., Wilson, J., Attema, E., Gelsthorpe, R., Drinkwater, M. and Stoffelen, A., 2002. The advanced scatterometer (ASCAT) on the meteorological operational (MetOp) platform: A follow on for the european wind scatterometers. *Can. J. Remote Sensing* 28(3), pp. 404–412.

Gow, A. and Tucker, W., 1990. *Sea ice in the polar regions*. Academic Press, San Diego.

Hendricks, S., Ricker, R. and Helm, V., 2016. AWI CryoSat-2 Sea Ice Thickness Data Product (v1.2).

Kim, S., Onstott R, . and Moore, R., 1984. Effect of a snow cover on microwave backscatter from sea ice. *IEEE Journal of Oceanic Engineering* 9(5), pp. 383–388.

KNMI, 2018. Daily sea ice extent and normalized radar backscatter (ASCAT, ERS, QuikSCAT and OceanSAT-2) User Manual.

Kurtz, N., Markus, T., Farrell, S., Worthen, D. and Boisvert, L., 2011. Observations of recent Arctic sea ice volume loss and its impacton ocean-atmosphere energy exchange and ice production. *Journal of Geophysical Research*.

Kwok, R., 2004. Annual cycles of multiyear sea ice coverage of the Arctic Ocean: 1999-2003. *J. Geophys. Res.*

Kwok, R., 2018. Arctic sea ice thickness, volume, and multiyear ice coverage: losses and coupled variability (1958-2018). *Environmental Research Letters*.

Kwok, R. and Cunningham, G., 2008. Icesat over arctic sea ice: Estimation of snow deth and ice thickness. *Journal of Geophysical Research*.

Kwok, R. and Rothrock, D., 2009. Decline in Arctic sea ice thickness from submarine and ICESat records: 1958-2008. *Geophysical Research Letters*.

Laxon, S., Giles, K., Ridout, A., Wingham, D., Willatt, R., Cullen, R., Kwok, R., Schweiger, A., Zhang, J., Haas, C., Hendricks, S., Krishfield, R., Kurtz, N., Farrell, S. and Davidson, M., 2013. CryoSat-2 estimates of Arctic sea ice thickness and volume. *Geophysical Research Letters* 40, pp. 732–737.

Onstott, R., 1992. *Microwave remote sensing of sea ice.* American Geophyical Union.

Otosaka, I., Belmonte-Rivas, M. and Stoffelen, A., 2017. Bayesian sea ice detection with the ERS scatterometer and sea ice backscatter model at c-band. *IEEE Transactions on Geoscience and Remote Sensing* 56(4), pp. 2248–2254.

Perovich, D., Meier, W., Tschudi, M., Farrell, S., Hendricks, S., Haas, C., Krumpen, T., Polashenshki, C., Ricker, R. and Webster, M., 2018. *Arctic repord card: update for 2018 - Sea ice*. NOAA's Arctic Programme, Retrieved on March 5th, 2019 from https://www.arctic.noaa.gov/Report-Card/Report-Card-2018/ArtMID/7878/ArticleID/780/SeanbspIce.

Rahmstorf, S., 2006. *Encyclopedia of Quaternary Sciences: Thermohaline Ocean Circulation*. Elsevier.

Ricker, R., Hendricks, S., Helm, V., Skourup, H. and Davidson, M., 2014. Sensitivity of CryoSat-2 Arctic sea ice freeboard and thickness on radar-waveform interpretation. *Cryosphere* 8(4), pp. 1607–1622.

Ricker, R., Hendricks, S., Perovich, D., Helm, V. and Gerdes, R., 2015. Impact of snow accumulation on CryoSat-2 range retrievals over Arctic sea ice: An observational approach with buoy data. *Geophysical Research Letters* 42(11), pp. 4447–4455.

Schutz, B., Zwally, H., Shuman, C., Hancock, D. and DiMarzio, J., 2005. Overview of the ICESat mission. *Geophysical Research Letters*.

Shokr, M. and Sinha, N., 2015. *Ice Physics and Physical Processes*. John Wiley & and Sons, Inc.

Spencer, M., Wu, C. and Long, D., 2000. Improved resolution backscatter measurements with the SeaWinds pencil-beam scatterometer. *IEEE Transactions on Geoscience and Remote Sensing* 38(1), pp. 89–104.

Stoffelen, A., 2001. Scatterometry.

Stoffelen, A. and de Haan, S., 2001. Ice discrimination using ERS scatterometer. *EUMETSAT OSI-SAF Technical report SAF/OSI/KNMI/TEC/TN/120*.

Szanyi, S., Lukovich, J., Barber, D. and Haller, G., 2016. Persistent artefacts in the NSIDC sea ice motion data set and their implications for analysis. *Geophysical Research Letters*.

Teleti, P. and Luis, A., 2013. Sea ice observations in polar regions: Evolution of technologies in remote sensing. *International Journal of Geosciences* 4(7), pp. 1031–1050.

Tschudi, M., Fowler, C., J., M., Stewart, J. and Meier, W., 2017. Polar pathfinder daily 25 km ease-grid sea ice motion vectors. version 3. [monthly, northern hemisphere subset was used.].

Tschudi, M., Fowler, C., Maslanik, J., Stewart, J. and Meier, W., 2016a. EASE-Grid Sea Ice Age, Version 3. [March 2003-2018].

Tschudi, M., Stroeve, J. and Stewart, J., 2016b. Relating the age of Arctic sea ice to its thickness, as measured during NASA's ICESat and IceBridge campaigns. *Remote Sensing*.

Vaughan, D., Comiso, J., Allison, I., Carrasco, J., Kaser, G., Kwok, R., Mote, P., Murray, T., Paul, F., Ren, J., Rignot, E., Solomina, O., Steffen, K. and Zhang, T., 2013. *Observations: Cryosphere*. Cambridge University Press, Cambridge, United Kingdom and New York, USA.

Vihma, T., 2014. Effects of Arctic Sea Ice Decline on Weather and Climate: A Review. *Surveys of Geophysics* 35(5), pp. 1175–1214.

Voss, S., Heygster, G. and Ezraty, R., 2003. Improving sea ice type discrimination by the simultaneous use of SSM/I and scatterometer data. *Polar Research* 22(1), pp. 35–42.

Warren, S., Rigor, I., Untersteiner, N., Radionov, V., Bryazgin, N., Aleksandrov, Y. and Colony, R., 1999. Snow depth on Arctic sea ice. *J. Climate* 12, pp. 1814–1829.

Willmes, S., Haas, C. and Nicolaus, M., 2011. High radar backscatter regions on Antarctic sea ice and their relation to sea ice and snow properties and meteorological conditions. *International Journal of Remote Sensing* 32(14), pp. 3967–3984.

Yi, D. and Zwally, H., 2009. *Arctic Sea Ice Freeboard and Thickness, Version 1. [All subsets were used]*. Boulder, Colorado USA. NSIDC: National Snow and Ice Data Center. Retrieved on June 4th, 2018 from https://doi.org/10.5067/SXJVJ3A2XIZT.

Zhang, J. and Rothrock, D., 2003. Modeling global sea ice with a thickness and enthalpy distribution modelin generalized curvilinear coordinates. *Monthly Weather Review* 131(5), pp. 681–697.

Zhang, J., Lindsay, R., Schweiger, A. and Rigor, I., 2012. Recent changes in the dynamic properties of declining Arctic sea ice: A model study. *Geophysical Research Letters*.

Zwally, H., Schutz, B., Abdalati, W., Abshire, J., Bently, C., Brenner, A., Bufton, J., Dezio, J., Hancock, D., Harding, D., Herring, T., Minster, B., Quinn, K., Palm, S., Spinhirne, J. and Thomas, R., 2002. ICESat's laser measurements of polar ice, atmosphere, ocean and land. *Journal of Geodynamics* 34, pp. 405–445.

Zwally, H., Yi, D., Kwok, R. and Zhao, Y., 2008. ICESat Measurements of Sea Ice Freeboard and Estimates of Sea Ice Thickness in the Weddell Sea. *Journal of Geophysical Research*.

A

Backscatter maps

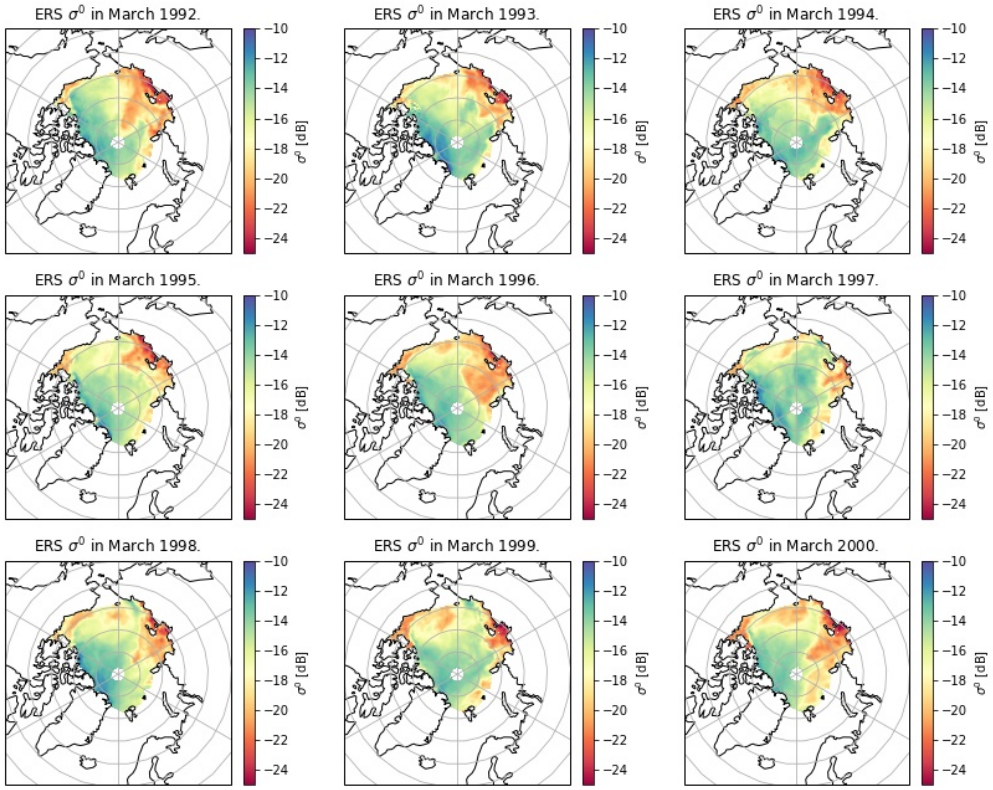

Figure A.1: ERS March average normalized σ^0 (1992-2000).

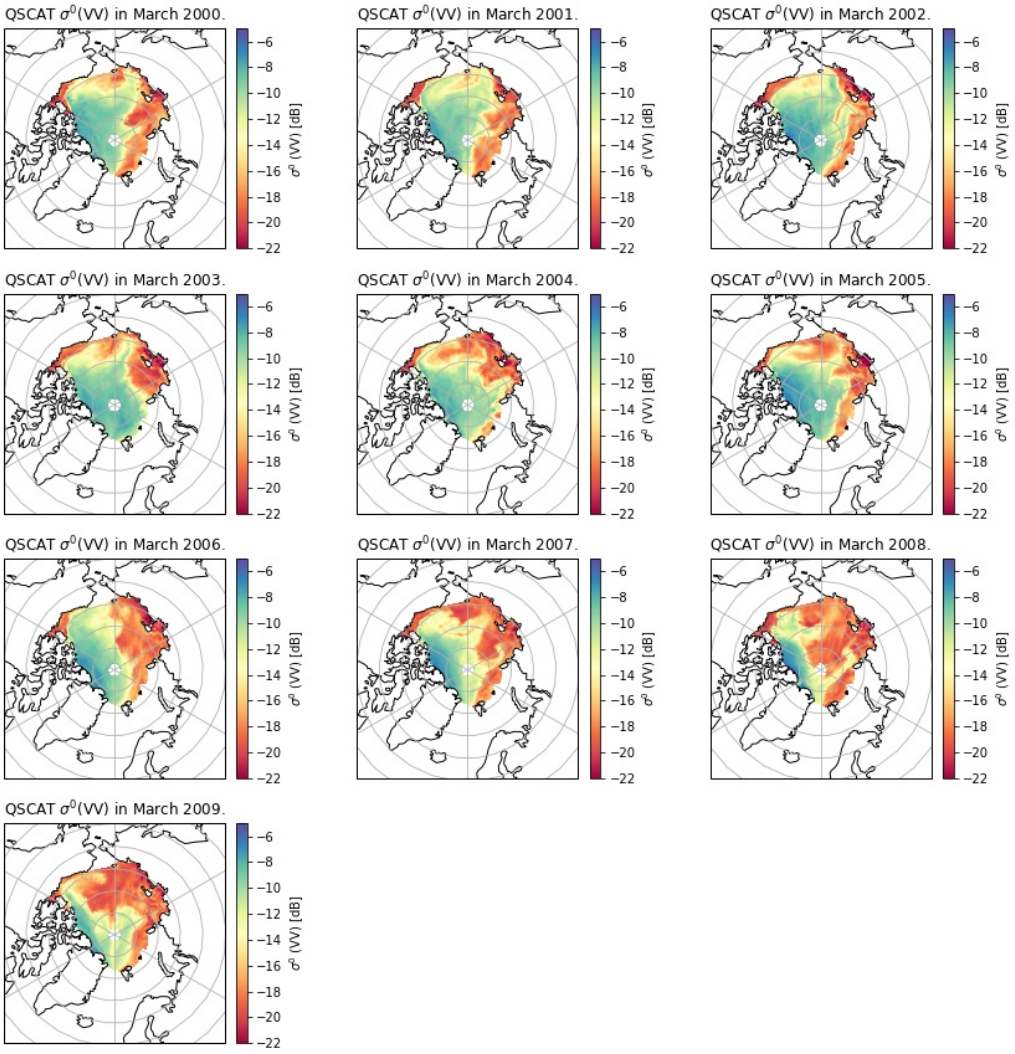

Figure A.2: QuikSCAT March average normalized σ^0 (2000-2009).

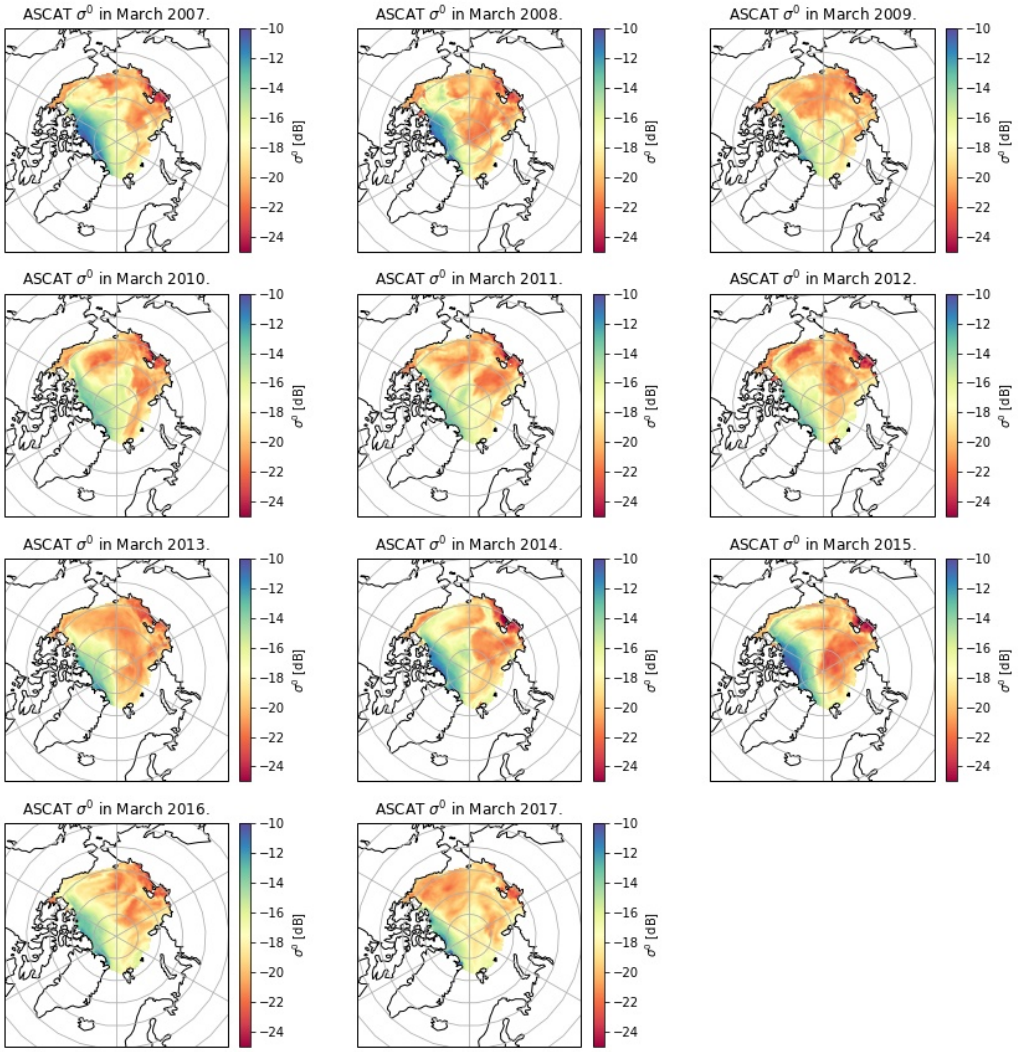

Figure A.3: ASCAT March average normalized σ^0 (2007-2017).

B

Reference ICESat + CryoSat-2 sea ice thickness maps

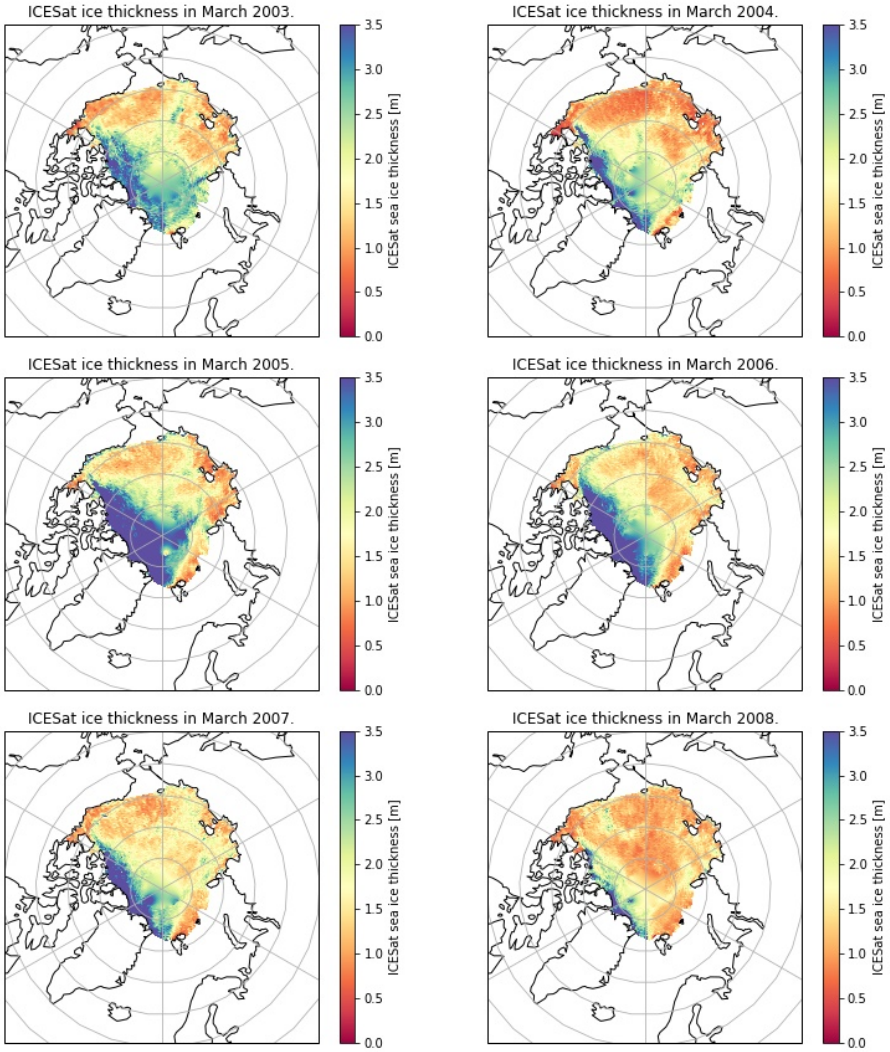

Figure B.1: ICESat (March) sea ice thickness (2003-2008).

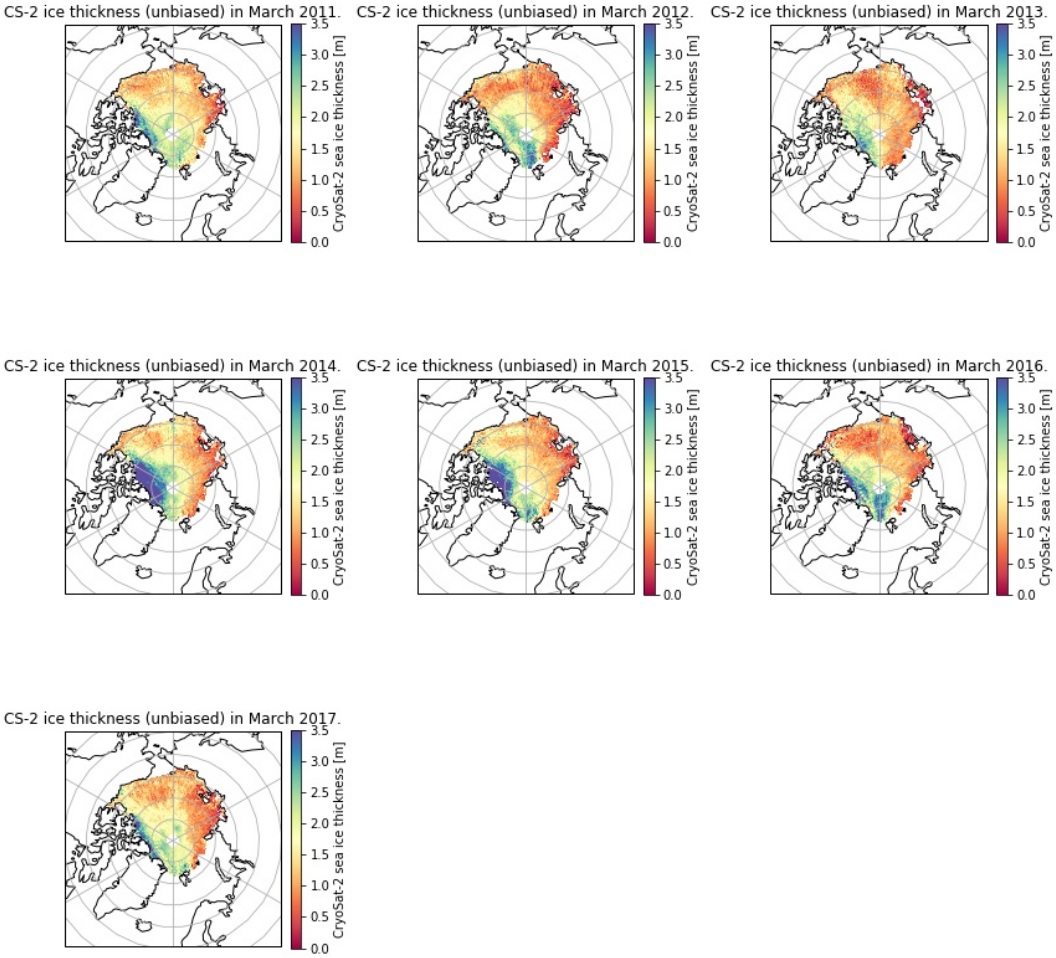

Figure B.2: CryoSat-2 (March) sea ice thickness (2011-2017), where the 55 cm bias has been removed.

C

Gaussian fitting procedure tables

Table C.1: Gaussian fits per bin, Ku-band.

σ^0 [dB]	a	b	c	σ_a	σ_b	σ_c
-24.80	0.65	1.01	0.18	0.10	0.03	0.03
-24.62	1.69	1.03	0.09	0.13	0.01	0.01
-24.43	1.13	1.37	0.17	0.09	0.02	0.02
-24.24	1.74	1.15	-0.12	0.14	0.01	0.01
-24.05	2.32	1.03	0.12	0.32	0.02	0.02
-23.87	16.82	1.01	0.02	300096.25	16.61	80.27
-23.68	0.72	1.03	0.53	0.14	0.13	0.14
-23.49	1.34	1.24	0.60	0.25	0.13	0.14
-23.30	15.90	0.89	0.03	20.93	0.03	0.03
-23.12	4.46	0.92	0.29	0.34	0.03	0.03
-22.93	10.12	0.87	0.13	0.51	0.01	0.01
-22.74	13.32	0.96	0.16	0.41	0.01	0.01
-22.55	12.60	0.91	0.17	0.42	0.01	0.01
-22.37	15.47	0.93	0.17	0.50	0.01	0.01
-22.18	21.29	0.92	0.15	0.73	0.01	0.01
-21.99	25.55	0.90	0.15	0.70	0.00	0.00
-21.80	29.27	0.94	0.19	1.09	0.01	0.01
-21.61	27.08	0.96	0.21	0.58	0.01	0.01
-21.43	27.78	0.94	0.21	0.63	0.01	0.01
-21.24	35.16	0.96	0.16	0.93	0.00	0.00
-21.05	39.36	0.99	0.19	1.20	0.01	0.01
-20.86	81.88	0.96	0.14	1.68	0.00	0.00
-20.68	98.65	0.96	0.15	2.59	0.00	0.00
-20.49	99.78	0.99	0.20	1.93	0.00	0.00
-20.30	116.22	1.06	0.23	1.72	0.00	0.00
-20.11	161.47	1.07	0.25	2.28	0.00	0.00
-19.93	239.20	1.08	0.22	3.18	0.00	0.00
-19.74	295.40	1.14	0.23	3.84	0.00	0.00
-19.55	360.84	1.12	0.23	5.27	0.00	0.00
-19.36	365.87	1.14	0.25	8.01	0.01	0.01
-19.18	411.54	1.15	0.26	10.66	0.01	0.01
-18.99	439.83	1.15	0.29	12.39	0.01	0.01
-18.80	488.34	1.18	0.30	10.66	0.01	0.01
-18.61	545.85	1.20	0.29	11.44	0.01	0.01
-18.43	579.23	1.19	0.27	9.38	0.01	0.01
-18.24	553.34	1.20	0.28	8.94	0.01	0.01

-18.05	459.73	1.22	0.32	7.92	0.01	0.01
-17.86	421.95	1.23	0.32	6.30	0.01	0.01
-17.68	413.88	1.26	0.31	5.08	0.00	0.00
-17.49	343.58	1.27	0.34	5.79	0.01	0.01
-17.30	321.43	1.28	0.33	5.70	0.01	0.01
-17.11	304.53	1.27	0.32	5.70	0.01	0.01
-16.93	264.42	1.25	0.33	6.06	0.01	0.01
-16.74	251.91	1.25	0.31	5.47	0.01	0.01
-16.55	238.45	1.23	0.32	5.84	0.01	0.01
-16.36	219.99	1.21	0.30	4.77	0.01	0.01
-16.17	190.35	1.23	0.32	4.13	0.01	0.01
-15.99	162.68	1.25	0.35	3.79	0.01	0.01
-15.80	170.26	1.26	0.35	4.57	0.01	0.01
-15.61	161.37	1.30	0.37	3.96	0.01	0.01
-15.42	152.51	1.33	0.36	3.32	0.01	0.01
-15.24	144.54	1.38	0.36	2.71	0.01	0.01
-15.05	145.20	1.38	0.34	2.74	0.01	0.01
-14.86	150.32	1.38	0.32	3.21	0.01	0.01
-14.67	157.27	1.40	0.32	2.98	0.01	0.01
-14.49	156.63	1.40	0.31	2.88	0.01	0.01
-14.30	169.57	1.41	0.30	3.44	0.01	0.01
-14.11	178.96	1.41	0.29	3.62	0.01	0.01
-13.92	183.23	1.42	0.30	3.30	0.01	0.01
-13.74	185.31	1.43	0.30	3.17	0.01	0.01
-13.55	183.24	1.44	0.31	3.61	0.01	0.01
-13.36	196.53	1.47	0.32	3.92	0.01	0.01
-13.17	203.01	1.49	0.32	3.92	0.01	0.01
-12.99	218.66	1.54	0.30	3.38	0.01	0.01
-12.80	215.46	1.57	0.30	4.02	0.01	0.01
-12.61	216.29	1.59	0.32	4.36	0.01	0.01
-12.42	204.44	1.63	0.33	4.22	0.01	0.01
-12.24	200.04	1.65	0.35	4.07	0.01	0.01
-12.05	201.16	1.70	0.36	4.51	0.01	0.01
-11.86	188.98	1.78	0.42	5.39	0.01	0.01
-11.67	171.83	1.84	0.47	4.87	0.02	0.02
-11.49	162.57	1.85	0.44	4.69	0.01	0.01
-11.30	158.97	1.87	0.46	4.67	0.02	0.02
-11.11	158.76	1.87	0.44	4.67	0.01	0.01
-10.92	177.29	1.88	0.40	4.47	0.01	0.01
-10.73	200.61	1.87	0.35	6.69	0.01	0.01
-10.55	194.82	1.91	0.34	6.18	0.01	0.01
-10.36	236.59	1.94	0.31	6.62	0.01	0.01
-10.17	282.89	2.01	0.33	7.45	0.01	0.01
-9.98	267.44	2.10	0.37	7.93	0.01	0.01
-9.80	304.14	2.15	0.36	12.01	0.02	0.02
-9.61	456.89	2.16	0.25	15.24	0.01	0.01
-9.42	291.64	2.26	0.38	10.48	0.02	0.02
-9.23	213.81	2.48	0.52	6.04	0.02	0.02
-9.05	187.40	2.54	0.55	6.21	0.02	0.02
-8.86	179.13	2.65	0.65	5.32	0.02	0.02
-8.67	203.58	2.66	0.60	5.55	0.02	0.02
-8.48	274.06	2.71	0.46	8.15	0.02	0.02
-8.30	252.46	2.76	0.46	7.54	0.02	0.02
-8.11	155.36	3.13	0.70	4.72	0.02	0.02
-7.92	114.87	3.29	0.72	2.31	0.02	0.02
-7.73	128.79	3.46	0.59	2.13	0.01	0.01

-7.55	133.35	3.62	0.58	3.79	0.02	0.02
-7.36	110.96	3.93	0.53	1.77	0.01	0.01
-7.17	69.80	4.07	0.52	2.57	0.02	0.02
-6.98	28.82	4.29	0.65	1.53	0.04	0.04
-6.80	15.00	4.02	nan	inf	inf	inf
-6.61	9.00	4.29	nan	inf	inf	inf
-6.42	1.86	4.43	1.55	0.27	0.27	0.29
-6.23	3.81	2.75	0.23	0.30	0.02	0.02

Table C.2: Gaussian fits per bin, C-band.

σ^0 **[dB]**	**a**	**b**	**c**	σ_a	σ_b	σ_c
-25.50	2.00	1.83	-0.01	0.00	0.00	0.00
-25.36	7.62	1.68	0.01	734517.24	0.00	340.18
-25.22	0.84	1.59	0.09	0.08	0.01	0.01
-25.08	0.47	1.34	0.33	0.10	0.08	0.08
-24.94	0.91	1.29	0.13	0.16	0.03	0.03
-24.80	0.90	1.06	0.48	0.14	0.09	0.09
-24.66	0.95	1.20	0.46	0.12	0.06	0.06
-24.52	1.96	1.08	0.08	0.20	0.01	0.01
-24.38	1.33	1.18	0.54	0.13	0.06	0.06
-24.24	1.49	1.25	0.50	0.14	0.05	0.06
-24.10	2.62	1.48	0.46	0.24	0.05	0.05
-23.96	3.77	1.30	0.34	0.26	0.03	0.03
-23.82	2.30	1.23	0.54	0.25	0.07	0.07
-23.68	4.75	1.25	0.37	0.32	0.03	0.03
-23.54	5.19	1.24	0.41	0.35	0.03	0.03
-23.40	6.36	1.15	0.42	0.38	0.03	0.03
-23.26	9.09	1.23	0.40	0.56	0.03	0.03
-23.12	10.16	1.28	0.47	0.74	0.04	0.04
-22.98	9.95	1.46	0.60	0.57	0.04	0.04
-22.84	14.42	1.66	0.55	0.85	0.04	0.04
-22.70	22.90	1.78	0.49	1.55	0.04	0.04
-22.56	37.24	1.85	0.43	2.62	0.04	0.04
-22.42	42.13	1.81	0.46	2.12	0.03	0.03
-22.28	44.78	1.68	0.45	1.24	0.01	0.01
-22.14	71.14	1.62	0.38	1.43	0.01	0.01
-22.00	94.39	1.64	0.37	1.95	0.01	0.01
-21.86	176.98	1.73	-0.28	3.60	0.01	0.01
-21.72	241.09	1.72	0.24	4.44	0.01	0.01
-21.58	267.97	1.70	0.27	4.85	0.01	0.01
-21.44	335.02	1.68	0.26	4.24	0.00	0.00
-21.30	400.70	1.67	0.27	3.07	0.00	0.00
-21.16	491.33	1.65	0.27	4.72	0.00	0.00
-21.02	512.39	1.69	0.29	5.00	0.00	0.00
-20.88	513.17	1.67	0.29	6.03	0.00	0.00
-20.74	544.53	1.66	0.29	5.92	0.00	0.00
-20.60	546.55	1.65	0.29	6.61	0.00	0.00
-20.46	520.20	1.64	0.29	5.89	0.00	0.00
-20.32	518.08	1.64	0.29	7.42	0.00	0.00
-20.18	498.32	1.66	0.30	6.68	0.00	0.00
-20.04	487.32	1.68	0.34	6.55	0.01	0.01
-19.90	460.81	1.69	0.35	6.08	0.01	0.01
-19.76	456.85	1.70	0.36	5.23	0.00	0.00

-19.62	468.00	1.68	0.35	5.82	0.01	0.01
-19.48	469.37	1.68	0.35	6.44	0.01	0.01
-19.34	447.33	1.71	0.36	4.67	0.00	0.00
-19.20	381.47	1.70	0.39	6.57	0.01	0.01
-19.06	299.81	1.70	0.45	5.61	0.01	0.01
-18.92	264.71	1.73	0.48	4.99	0.01	0.01
-18.78	237.70	1.78	0.54	5.61	0.01	0.01
-18.64	226.52	1.82	0.56	4.76	0.01	0.01
-18.50	218.16	1.90	0.58	3.30	0.01	0.01
-18.36	206.53	1.93	0.57	3.68	0.01	0.01
-18.22	182.32	2.03	0.60	3.23	0.01	0.01
-18.08	187.45	2.16	0.56	3.65	0.01	0.01
-17.94	170.28	2.13	0.54	3.48	0.01	0.01
-17.80	178.29	2.15	0.48	3.47	0.01	0.01
-17.66	165.38	2.21	0.49	3.63	0.01	0.01
-17.52	152.99	2.29	0.50	3.38	0.01	0.01
-17.38	144.38	2.39	0.52	3.07	0.01	0.01
-17.24	160.37	2.43	0.49	4.48	0.02	0.02
-17.10	152.97	2.44	0.49	3.67	0.01	0.01
-16.96	144.08	2.44	0.52	3.45	0.01	0.01
-16.82	136.90	2.50	0.55	2.79	0.01	0.01
-16.68	129.00	2.53	0.51	2.74	0.01	0.01
-16.54	124.92	2.59	0.46	2.76	0.01	0.01
-16.40	113.59	2.66	0.46	2.67	0.01	0.01
-16.26	111.31	2.69	0.40	2.65	0.01	0.01
-16.12	115.54	2.73	0.39	2.05	0.01	0.01
-15.98	148.80	2.80	0.33	2.83	0.01	0.01
-15.84	120.05	2.81	0.36	2.54	0.01	0.01
-15.69	118.17	2.80	0.32	2.36	0.01	0.01
-15.55	118.85	2.78	0.30	2.31	0.01	0.01
-15.41	120.54	2.81	0.30	2.26	0.01	0.01
-15.27	128.58	2.84	0.31	2.15	0.01	0.01
-15.13	144.57	2.88	0.30	2.25	0.01	0.01
-14.99	148.40	2.87	0.30	2.41	0.01	0.01
-14.85	109.06	2.85	0.38	1.59	0.01	0.01
-14.71	87.88	2.83	0.41	1.50	0.01	0.01
-14.57	86.17	2.82	0.43	2.02	0.01	0.01
-14.43	82.80	2.92	0.49	1.87	0.01	0.01
-14.29	81.12	2.97	0.50	2.04	0.01	0.01
-14.15	80.37	3.06	0.50	1.55	0.01	0.01
-14.01	78.78	3.13	0.46	1.24	0.01	0.01
-13.87	67.58	3.23	0.48	1.05	0.01	0.01
-13.73	60.61	3.27	0.44	1.06	0.01	0.01
-13.59	51.80	3.34	0.51	1.13	0.01	0.01
-13.45	49.12	3.41	0.59	1.23	0.02	0.02
-13.31	42.42	3.47	0.63	1.07	0.02	0.02
-13.17	34.79	3.61	0.64	0.81	0.02	0.02
-13.03	24.24	3.64	0.67	0.65	0.02	0.02
-12.89	23.32	3.84	-0.62	0.63	0.02	0.02
-12.75	19.22	3.90	0.71	0.71	0.03	0.03
-12.61	19.31	3.98	0.75	0.94	0.04	0.04
-12.47	18.11	4.01	0.82	0.85	0.04	0.04
-12.33	18.41	3.88	0.65	0.64	0.03	0.03
-12.19	-0.00	0.35	-0.36	2.53	1598373.82	1718171.32
-12.05	-0.00	0.47	-0.40	2.28	6130.96	6655.52
-11.91	0.00	0.69	-0.68	2.19	3459.99	3816.49

-11.77	-0.00	1.08	-0.22	3.32	1791724828.06	1791724841.51
-11.63	-0.00	1.09	-0.19	3.08	912088386.22	912088380.53
-11.49	-0.00	1.09	0.18	2.92	11635826.13	11635826.23
-11.35	0.00	1.15	0.16	2.14	1133229403.32	1133229397.68
-11.21	-0.00	1.26	-0.01	nan	nan	nan
-11.07	0.00	1.34	0.14	1.76	11798370263.81	11798370220.76
-10.93	0.00	1.29	0.04	2.34	143676499.45	179064408.80
-10.79	0.00	1.14	0.08	1.12	237926601.89	237926429.54
-10.65	0.00	0.82	0.22	0.40	2652966587.64	2653021575.05
-10.51	-0.00	1.10	0.12	0.74	44781439755.16	44781439631.57
-10.37	0.00	1.30	0.00	inf	inf	inf
-10.23	0.00	1.94	-0.02	0.87	1156492895.65	511817649.40

D

2-D yearly histograms

Figure D.1: Yearly 2-D histograms showing QuikSCAT σ^0 vs. ICESat sea ice thickness (2003-2008).

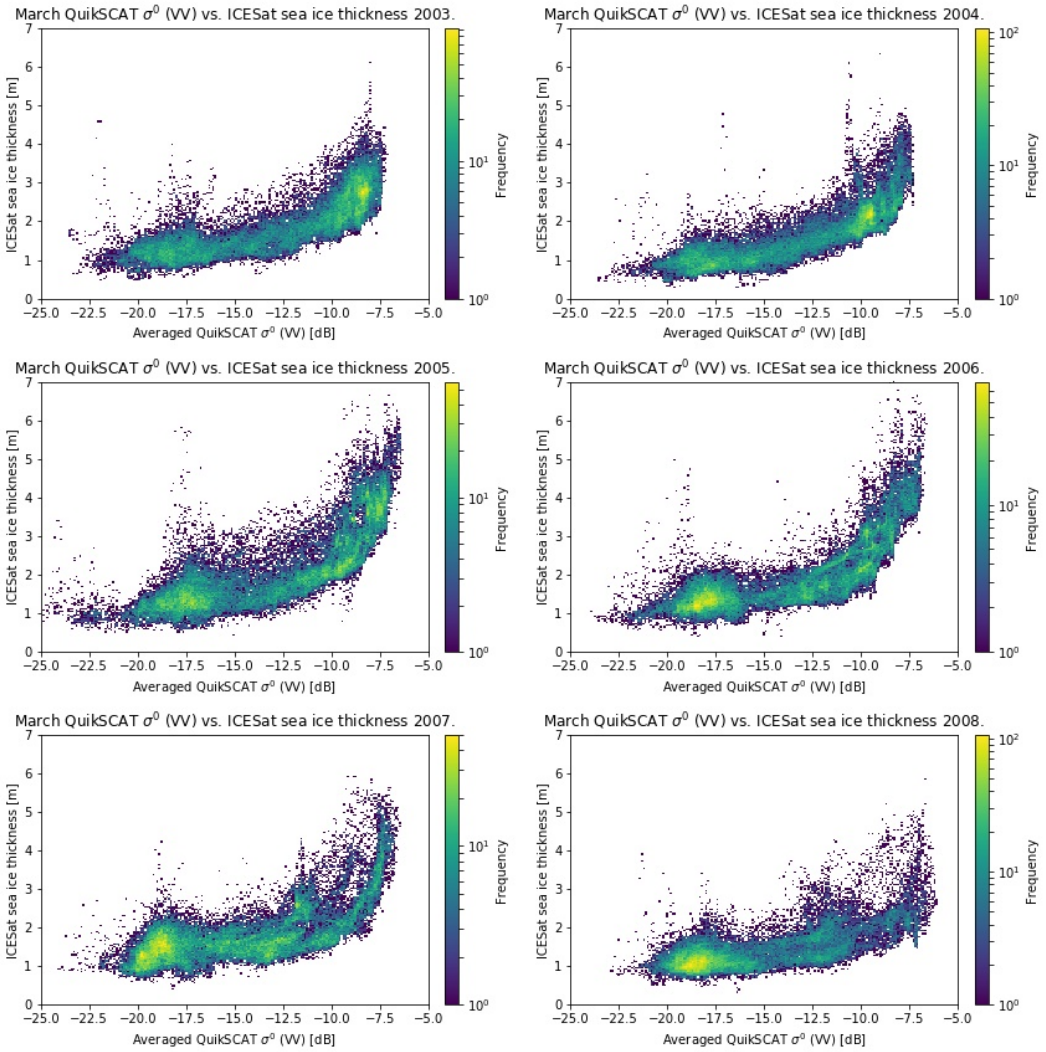

Figure D.2: Yearly 2-D histograms showing ASCAT σ^0 vs. CryoSat-2 AWI sea ice thickness (2011-2017).

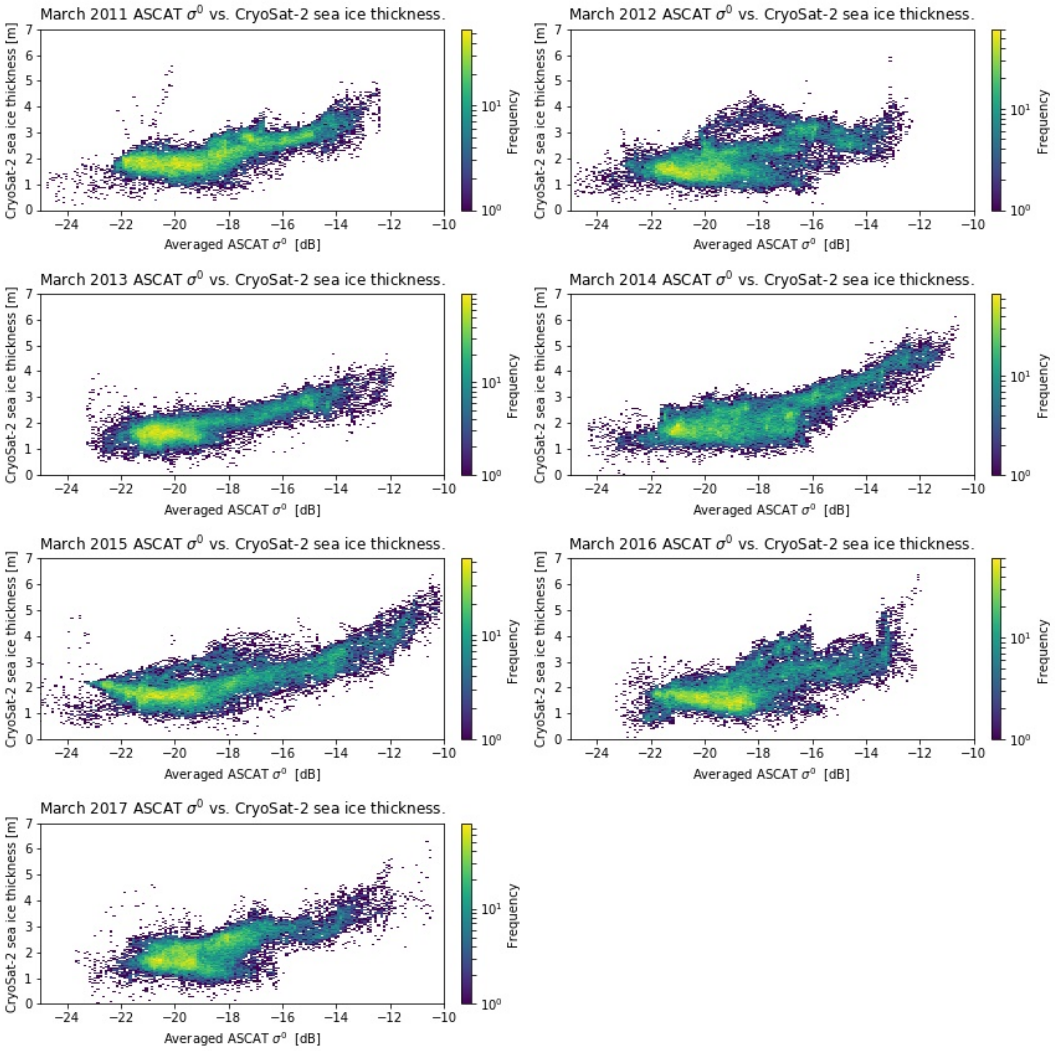

E

Yearly March average parameter plots

E.1. 2003

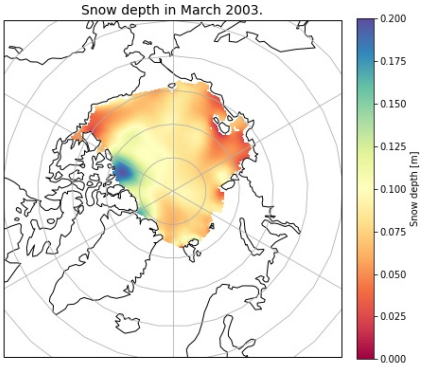

(a) PIOMAS snow depth in March 2003.

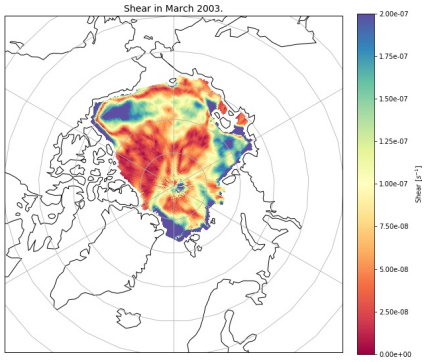

(b) Sea ice shear in March 2003.

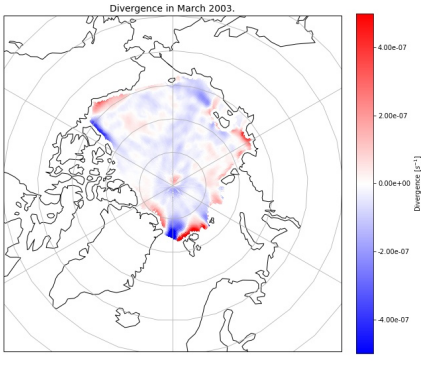

(c) Sea ice divergence in March 2003.

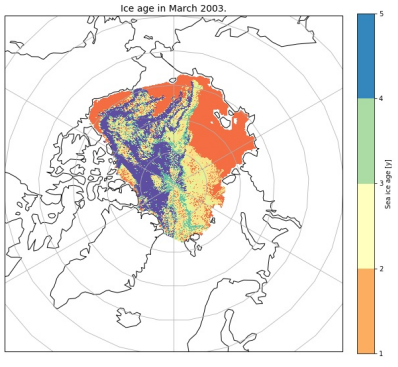

(d) NSIDC sea ice age in March 2003.

Figure E.2: Monthly averaged parameters in March 2003

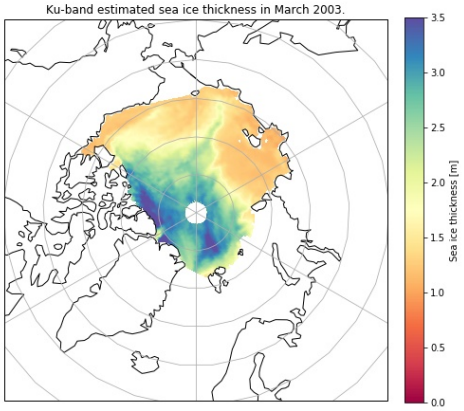

(a) Ku-band sea ice thickness in March 2003.

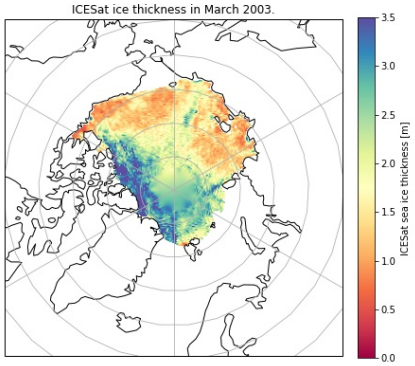

(b) ICESat sea ice thickness in March 2003.

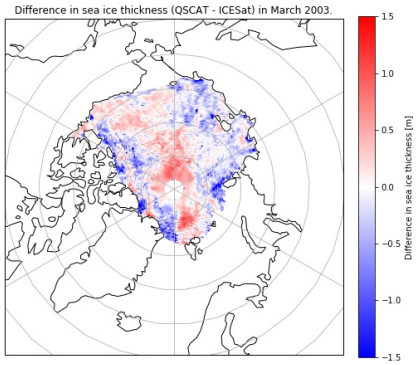

(c) Residuals of (QuikSCAT - ICESat) sea ice thickness in March 2003.

Figure E.1: Monthly sea ice thickness + residuals in March 2003.

E.2. 2004

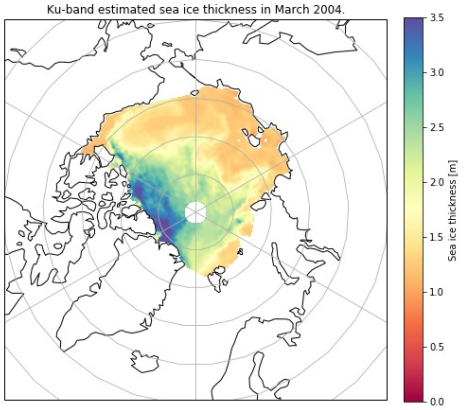

(a) Ku-band sea ice thickness in March 2004.

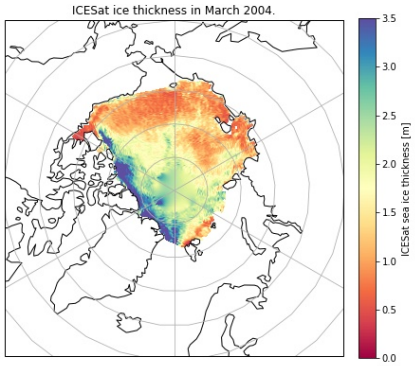

(b) ICESat sea ice thickness in March 2004.

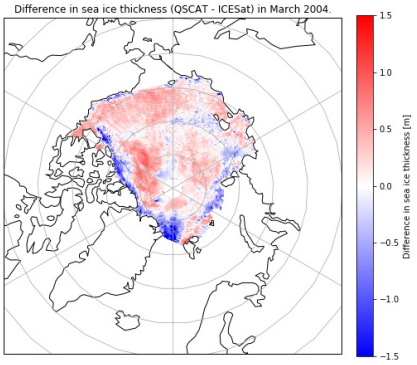

(c) Residuals of (QuikSCAT - ICESat) sea ice thickness in March 2004.

Figure E.3: Monthly sea ice thickness + residuals in March 2004.

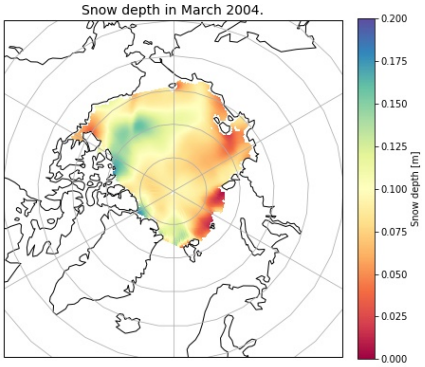

(a) PIOMAS snow depth in March 2004.

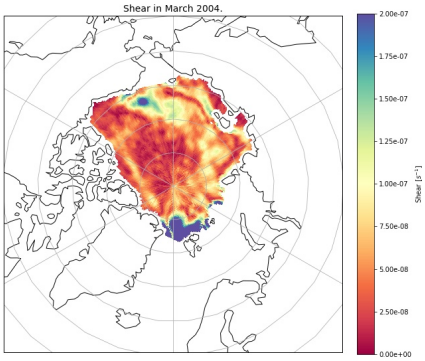

(b) Sea ice shear in March 2004.

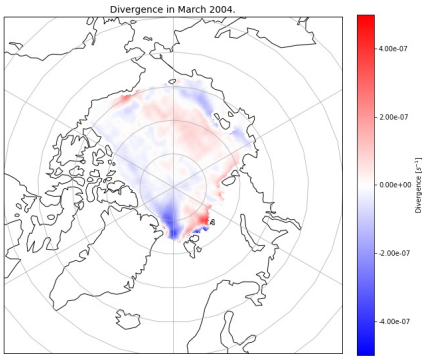

(c) Sea ice divergence in March 2004.

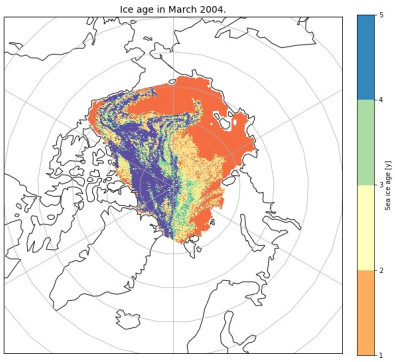

(d) NSIDC sea ice age in March 2004.

Figure E.4: Monthly averaged parameters in March 2004

E.3. 2005

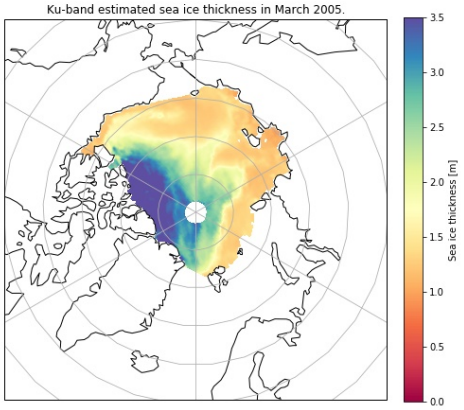

(a) Ku-band sea ice thickness in March 2005.

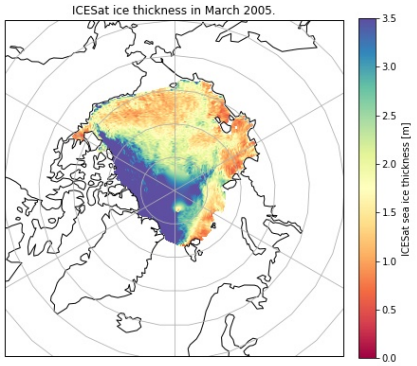

(b) ICESat sea ice thickness in March 2005.

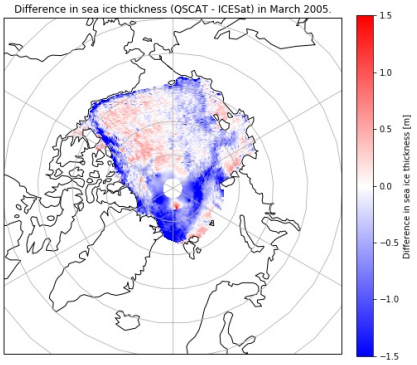

(c) Residuals of (QuikSCAT - ICESat) sea ice thickness in March 2005.

Figure E.5: Monthly sea ice thickness + residuals in March 2005.

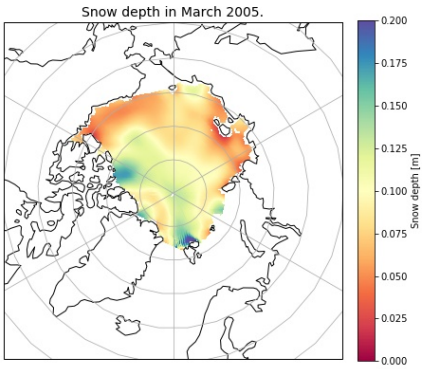

(a) PIOMAS snow depth in March 2005.

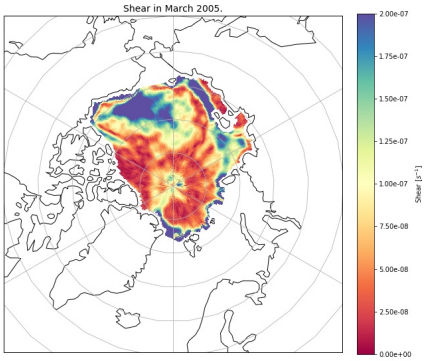

(b) Sea ice shear in March 2005.

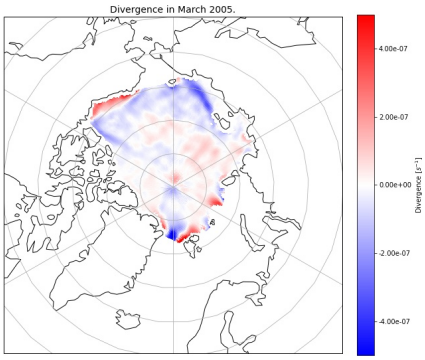

(c) Sea ice divergence in March 2005.

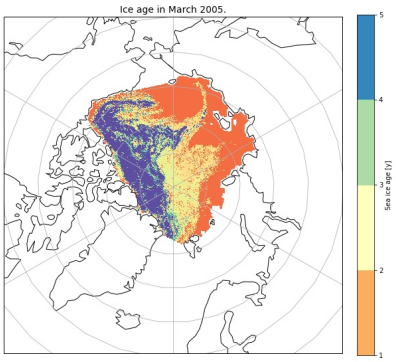

(d) NSIDC sea ice age in March 2005.

Figure E.6: Monthly averaged parameters in March 2005.

E.4. 2006

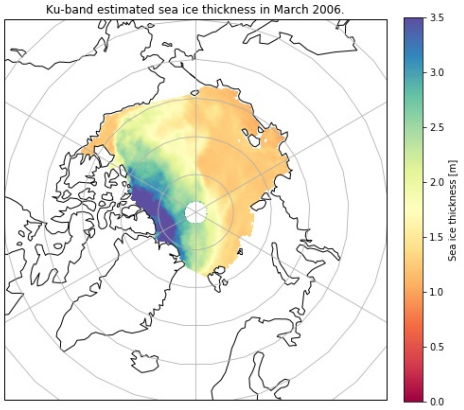

(a) Ku-band sea ice thickness in March 2006.

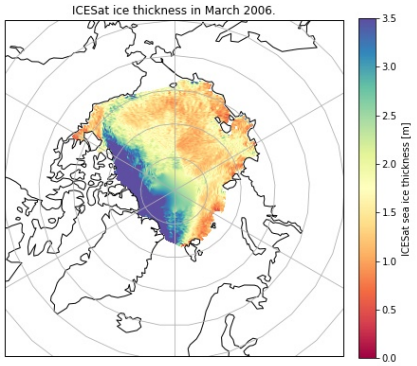

(b) ICESat sea ice thickness in March 2006.

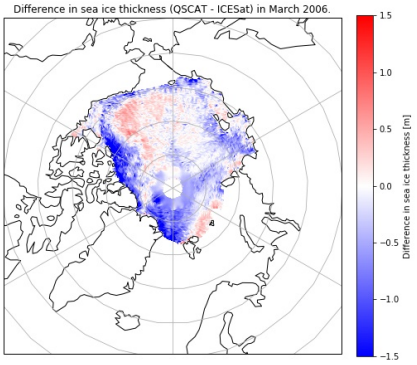

(c) Residuals of (QuikSCAT - ICESat) sea ice thickness in March 2006.

Figure E.7: Monthly sea ice thickness + residuals in March 2006.

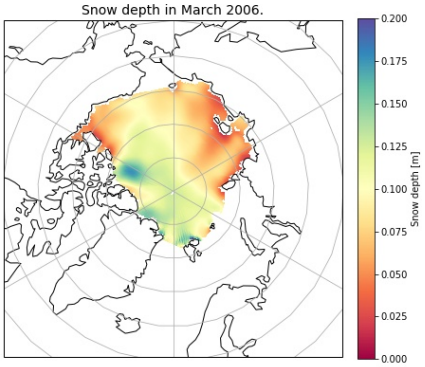

(a) PIOMAS snow depth in March 2006.

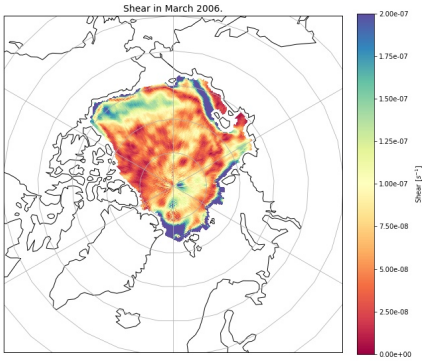

(b) Sea ice shear in March 2006.

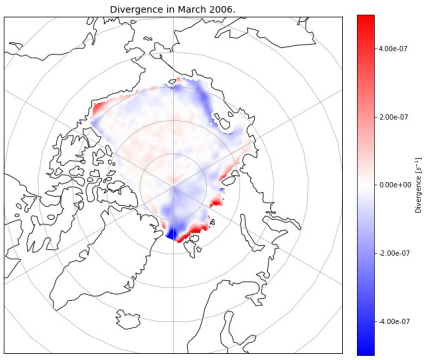

(c) Sea ice divergence in March 2006.

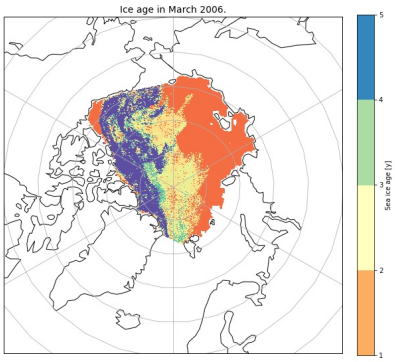

(d) NSIDC sea ice age in March 2006.

Figure E.8: Monthly averaged parameters in March 2006.

E.5. 2007

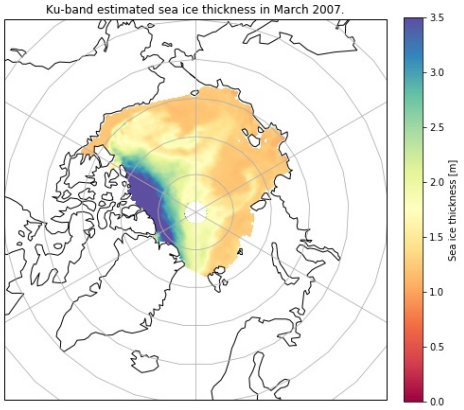

(a) Ku-band sea ice thickness in March 2007.

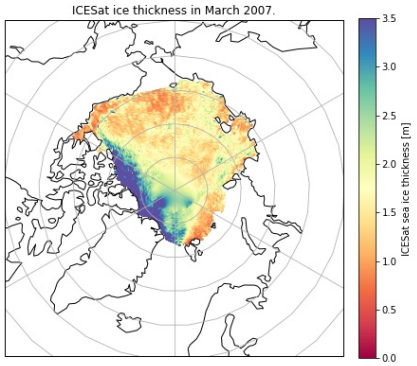

(b) ICESat sea ice thickness in March 2007.

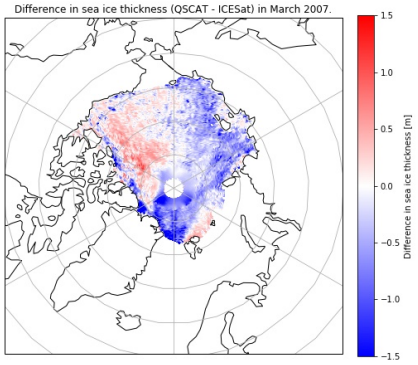

(c) Residuals of (QuikSCAT - ICESat) sea ice thickness in March 2007.

Figure E.9: Monthly sea ice thickness + residuals in March 2007.

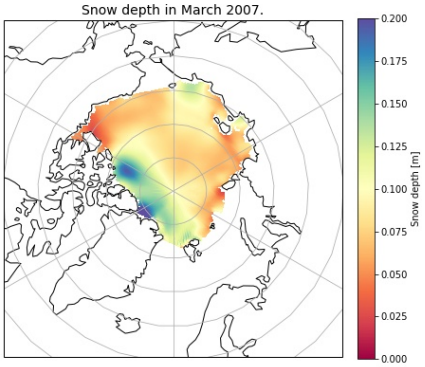

(a) PIOMAS snow depth in March 2007.

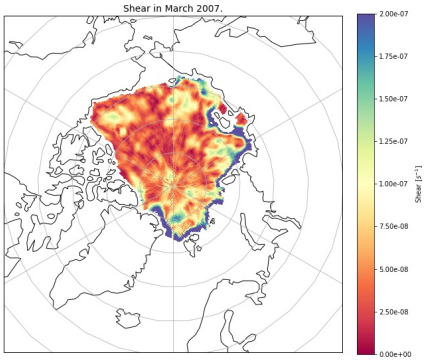

(b) Sea ice shear in March 2007.

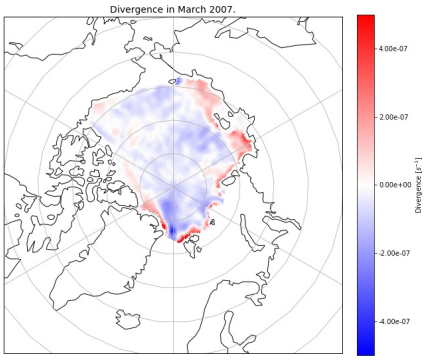

(c) Sea ice divergence in March 2007.

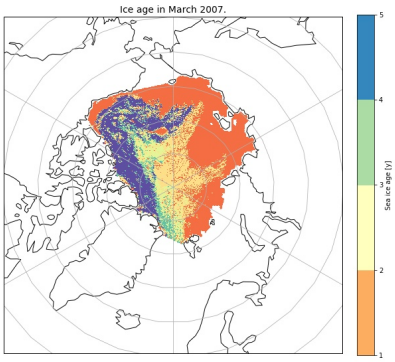

(d) NSIDC sea ice age in March 2007.

Figure E.10: Monthly averaged parameters in March 2007.

E.6. 2008

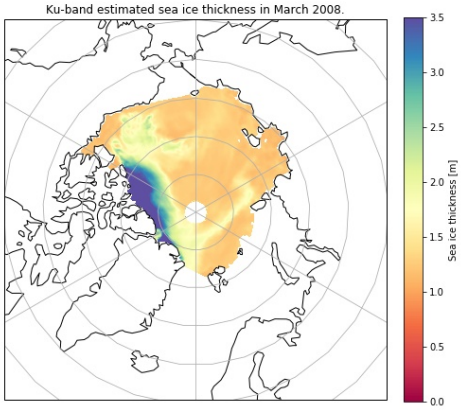

(a) Ku-band sea ice thickness in March 2008.

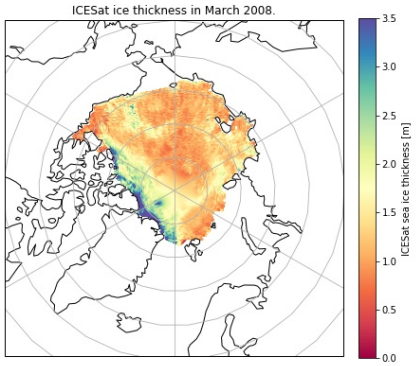

(b) ICESat sea ice thickness in March 2008.

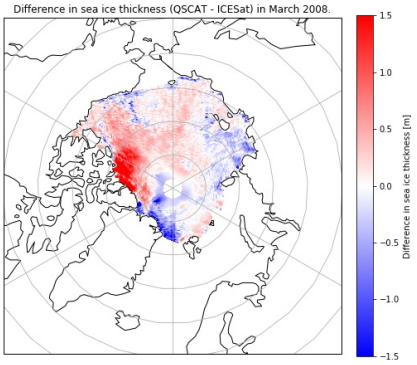

(c) Residuals of (QuikSCAT - ICESat) sea ice thickness in March 2008.

Figure E.11: Monthly sea ice thickness + residuals in March 2008.

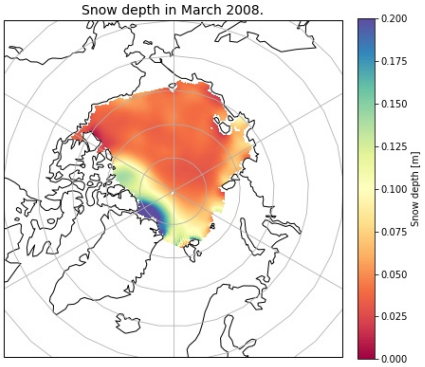

(a) PIOMAS snow depth in March 2008.

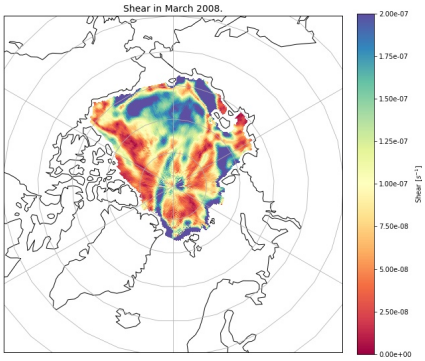

(b) Sea ice shear in March 2008.

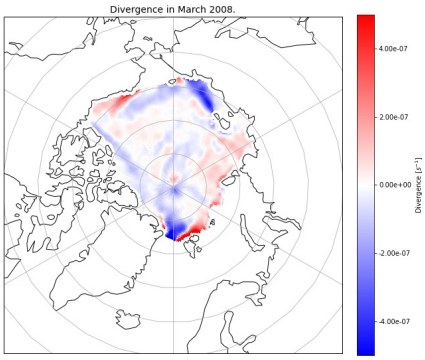

(c) Sea ice divergence in March 2008.

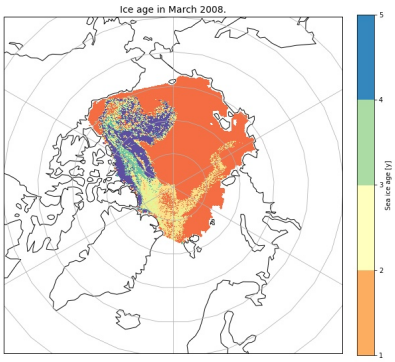

(d) NSIDC sea ice age in March 2008.

Figure E.12: Monthly averaged parameters in March 2008.

E.7. 2011

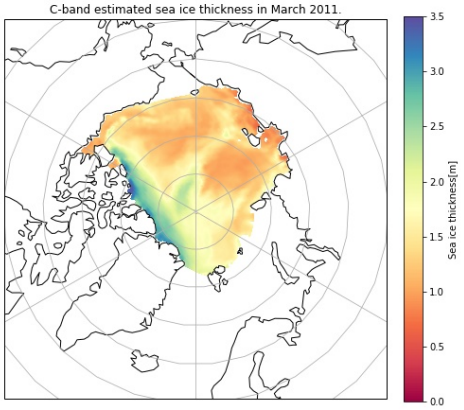

(a) C-band sea ice thickness in March 2011.

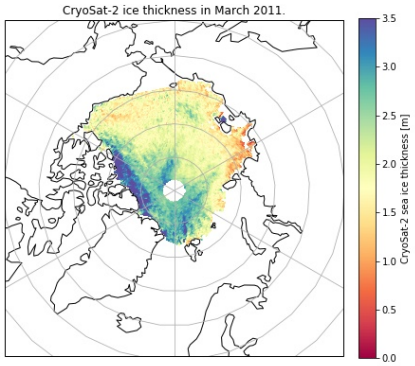

(b) CryoSat-2 sea ice thickness in March 2011.

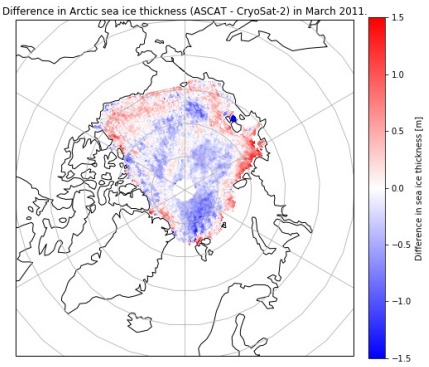

(c) Residuals of (ASCAT - CS-2) sea ice thickness in March 2011.

Figure E.13: Monthly sea ice thickness + residuals in March 2011.

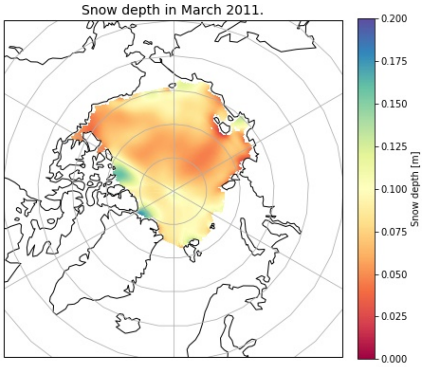

(a) PIOMAS snow depth in March 2011.

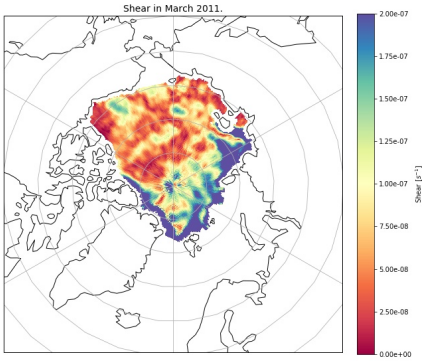

(b) Sea ice shear in March 2011.

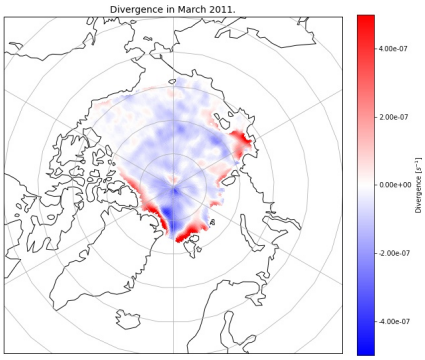

(c) Sea ice divergence in March 2011.

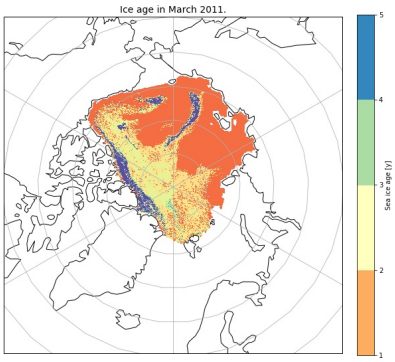

(d) NSIDC sea ice age in March 2011.

Figure E.14: Monthly averaged parameters in March 2011.

E.8. 2012

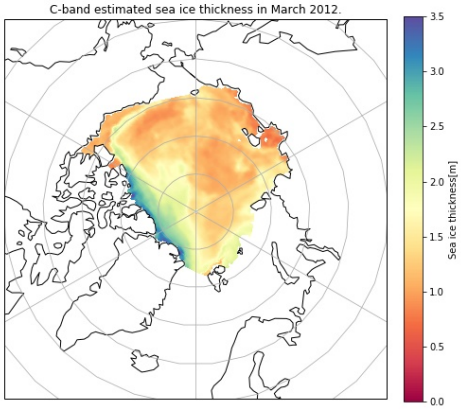

(a) C-band sea ice thickness in March 2012.

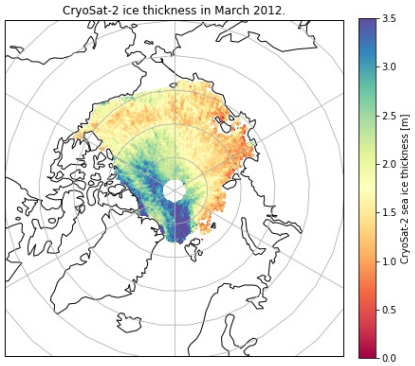

(b) CryoSat-2 sea ice thickness in March 2012.

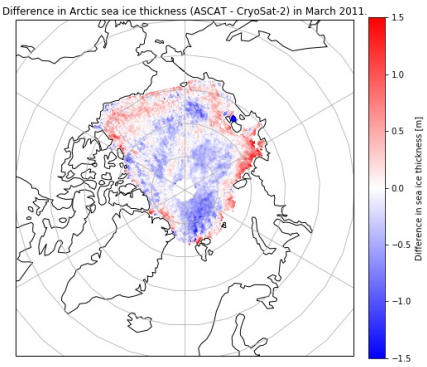

(c) Residuals of (ASCAT - CS-2) sea ice thickness in March 2012.

Figure E.15: Monthly sea ice thickness + residuals in March 2012.

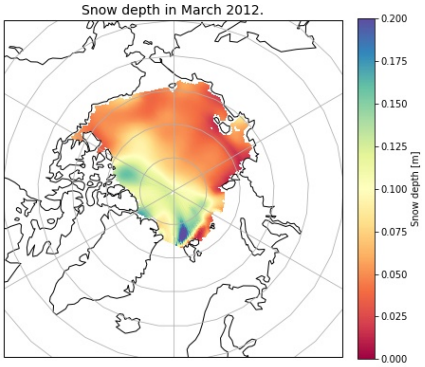

(a) PIOMAS snow depth in March 2012.

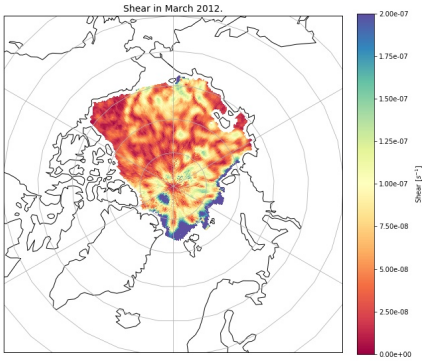

(b) Sea ice shear in March 2012.

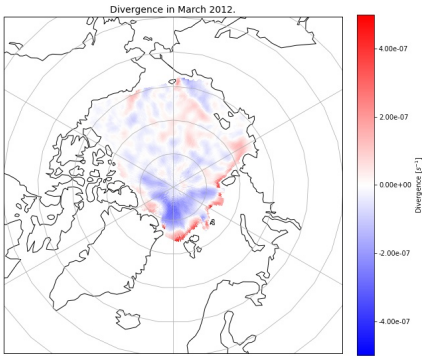

(c) Sea ice divergence in March 2012.

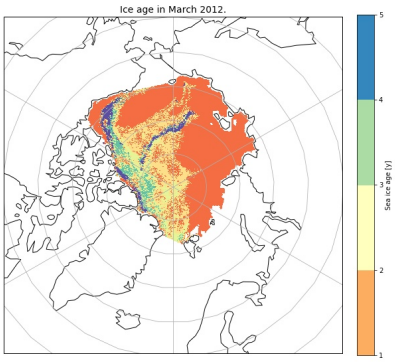

(d) NSIDC sea ice age in March 2012.

Figure E.16: Monthly averaged parameters in March 2012.

E.9. 2013

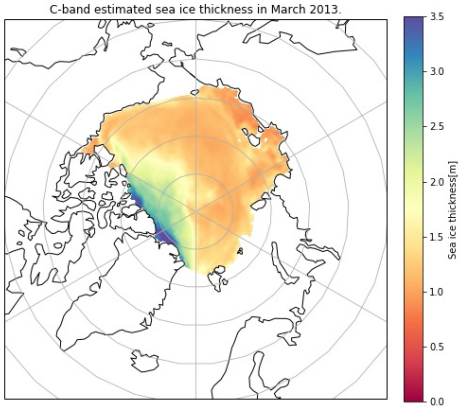

(a) C-band sea ice thickness in March 2013.

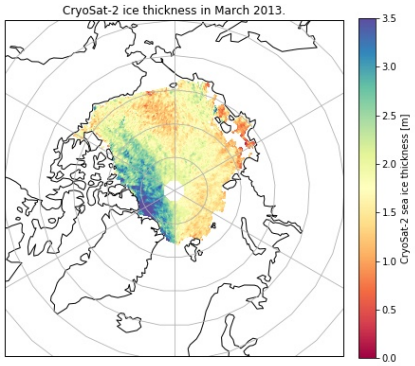

(b) CryoSat-2 sea ice thickness in March 2013.

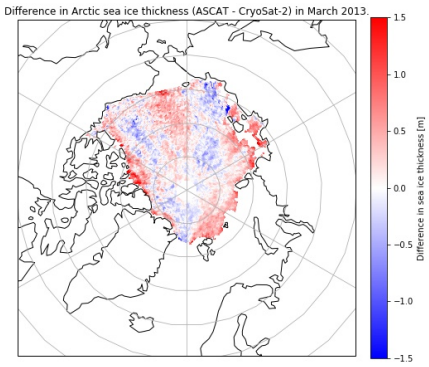

(c) Residuals of (ASCAT - CS-2) sea ice thickness in March 2013.

Figure E.17: Monthly sea ice thickness + residuals in March 2013.

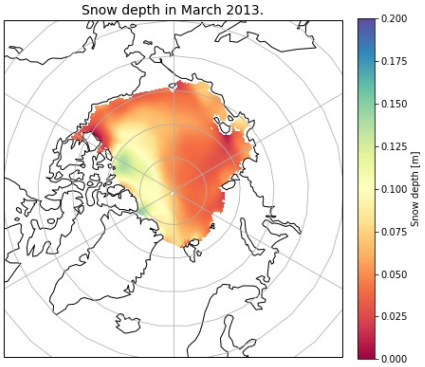

(a) PIOMAS snow depth in March 2013.

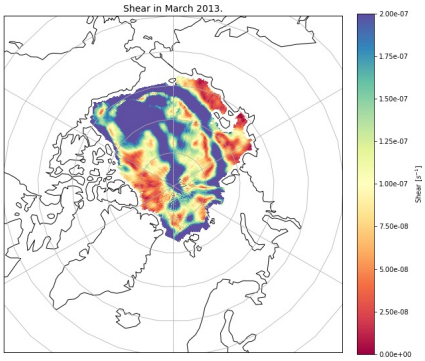

(b) Sea ice shear in March 2013.

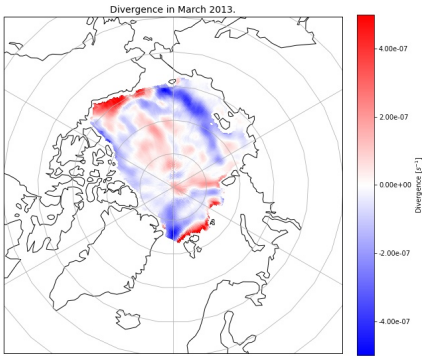

(c) Sea ice divergence in March 2013.

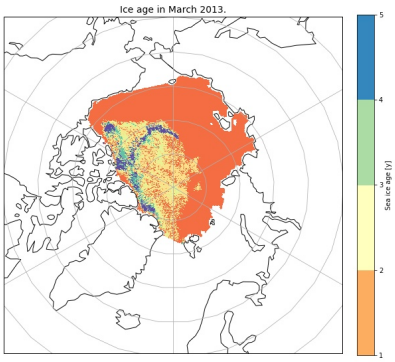

(d) NSIDC sea ice age in March 2013.

Figure E.18: Monthly averaged parameters in March 2013.

E.10. 2014

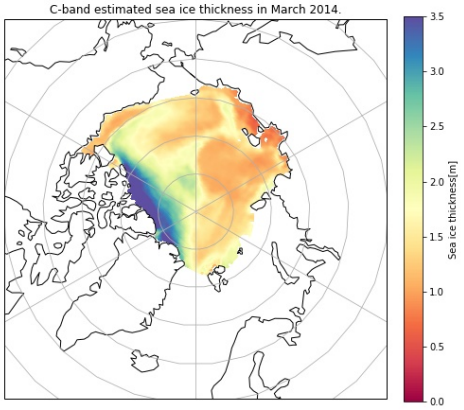

(a) C-band sea ice thickness in March 2014.

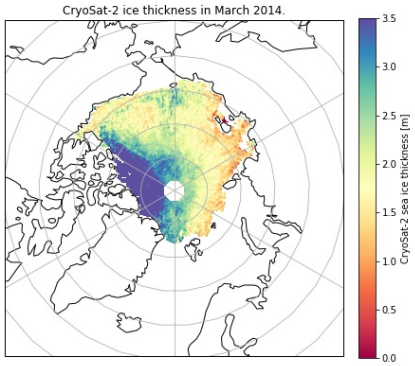

(b) CryoSat-2 sea ice thickness in March 2014.

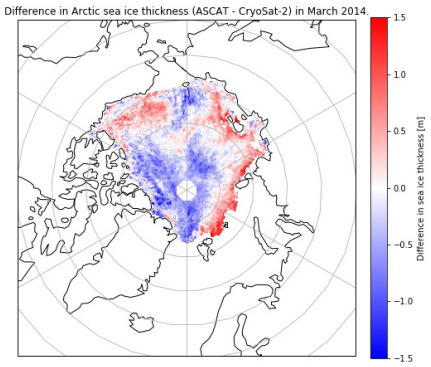

(c) Residuals of (ASCAT - CS-2) sea ice thickness in March 2014.

Figure E.19: Monthly sea ice thickness + residuals in March 2011.

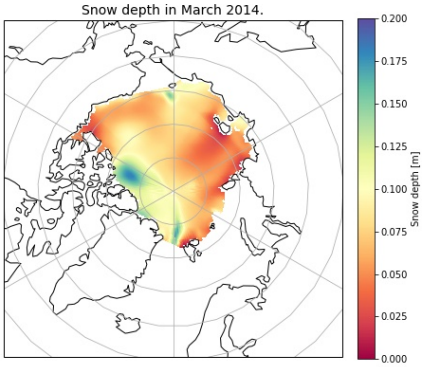

(a) PIOMAS snow depth in March 2014.

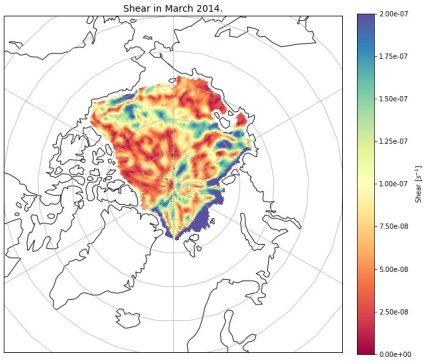

(b) Sea ice shear in March 2014.

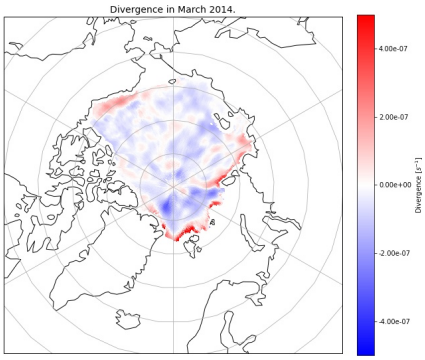

(c) Sea ice divergence in March 2014.

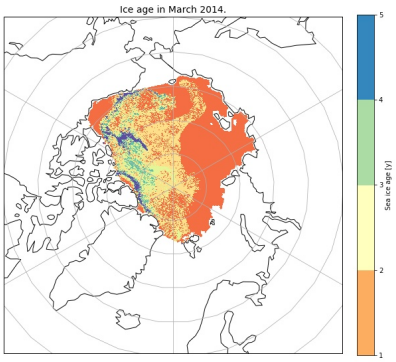

(d) NSIDC sea ice age in March 2014.

Figure E.20: Monthly averaged parameters in March 2014.

E.11. 2015

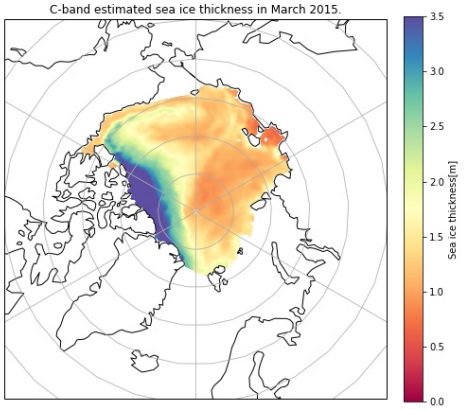

(a) C-band sea ice thickness in March 2015.

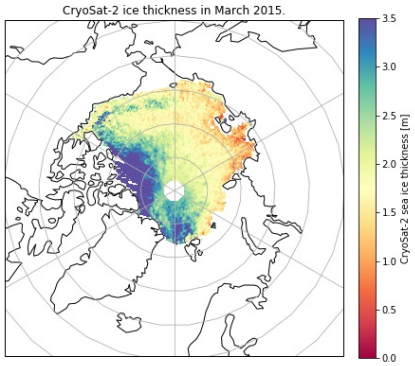

(b) CryoSat-2 sea ice thickness in March 2015.

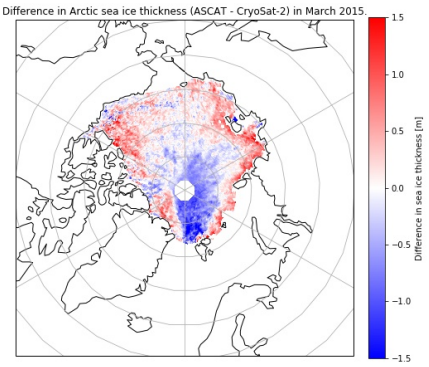

(c) Residuals of (ASCAT - CS-2) sea ice thickness in March 2015.

Figure E.21: Monthly sea ice thickness + residuals in March 2015.

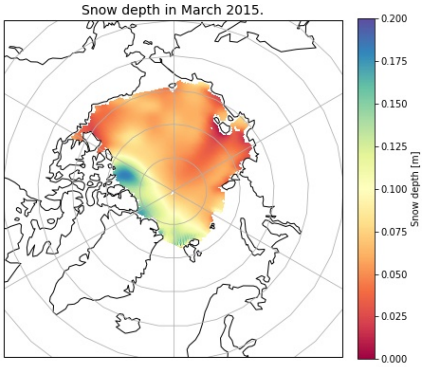

(a) PIOMAS snow depth in March 2015.

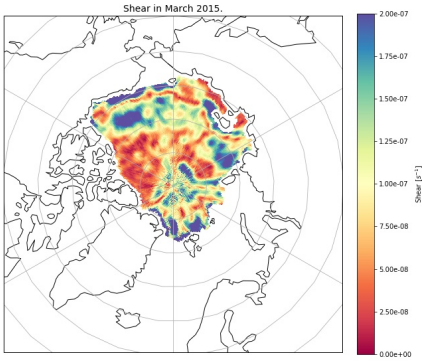

(b) Sea ice shear in March 2015.

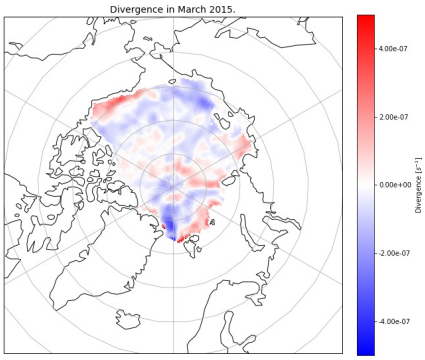

(c) Sea ice divergence in March 2015.

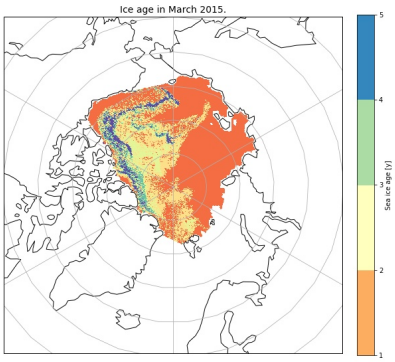

(d) NSIDC sea ice age in March 2015.

Figure E.22: Monthly averaged parameters in March 2015.

E.12. 2016

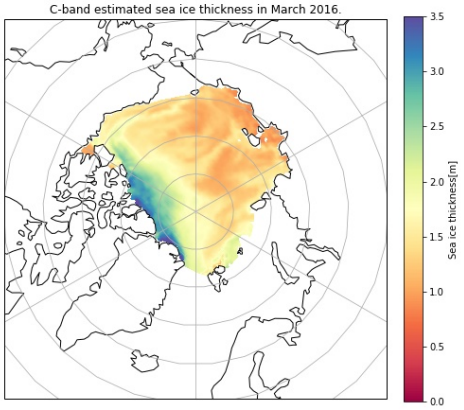

(a) C-band sea ice thickness in March 2016.

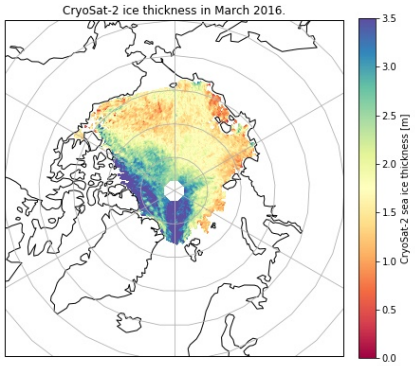

(b) CryoSat-2 sea ice thickness in March 2016.

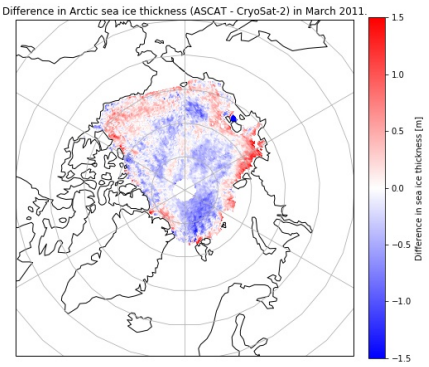

(c) Residuals of (ASCAT - CS-2) sea ice thickness in March 2016.

Figure E.23: Monthly sea ice thickness + residuals in March 2016.

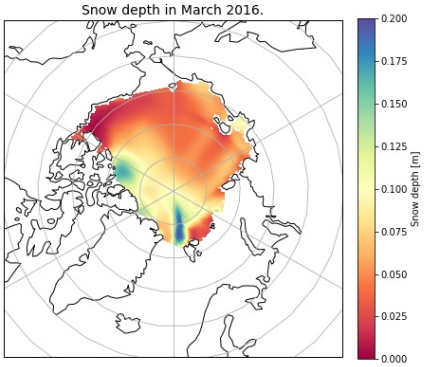

(a) PIOMAS snow depth in March 2016.

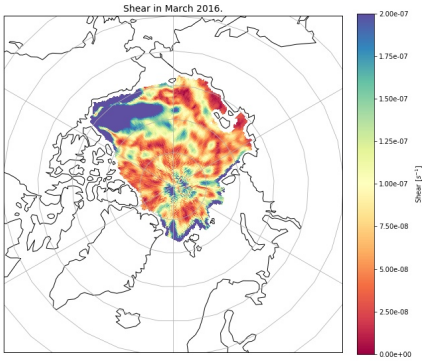

(b) Sea ice shear in March 2016.

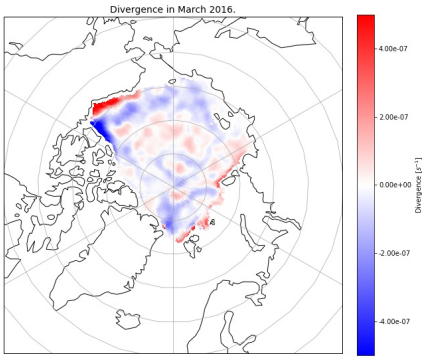

(c) Sea ice divergence in March 2016.

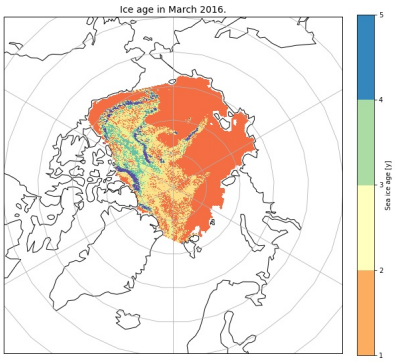

(d) NSIDC sea ice age in March 2016.

Figure E.24: Monthly averaged parameters in March 2016.

E.13. 2017

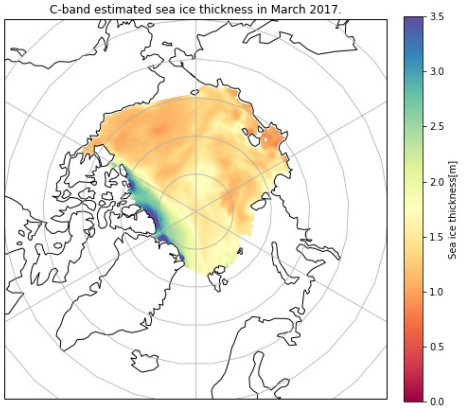

(a) C-band sea ice thickness in March 2017.

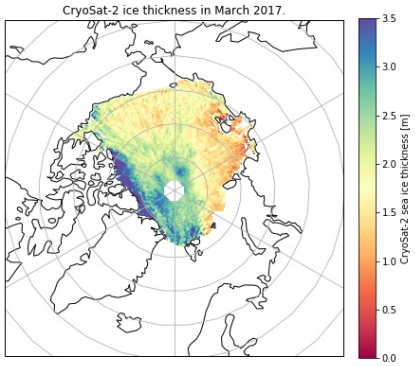

(b) CryoSat-2 sea ice thickness in March 2017.

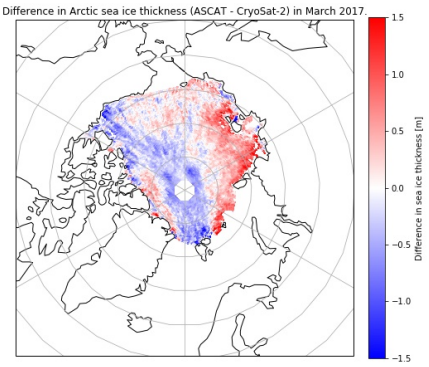

(c) Residuals of (ASCAT - CS-2) sea ice thickness in March 2017.

Figure E.25: Monthly sea ice thickness + residuals in March 2017.

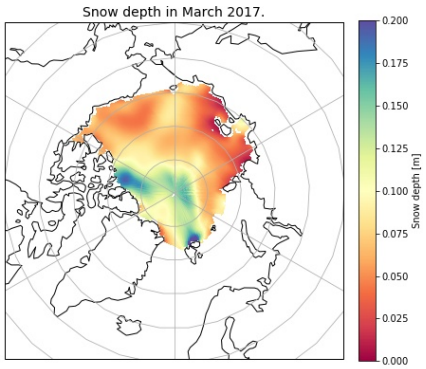

(a) PIOMAS snow depth in March 2017.

Figure E.26: Monthly averaged parameters in March 2017.

F

Scatterometer sea ice thickness

F.1. Arctic sea ice thickness maps 1992-2017

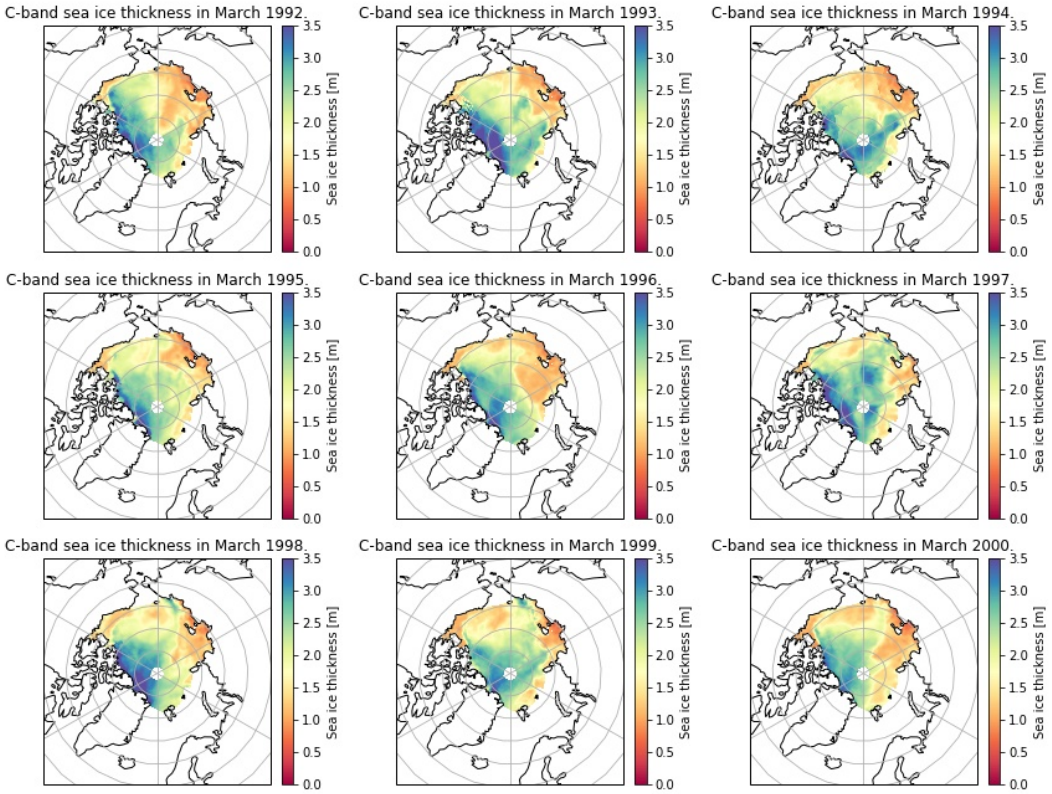

Figure F.1: ERS March sea ice thickness (1992-2000).

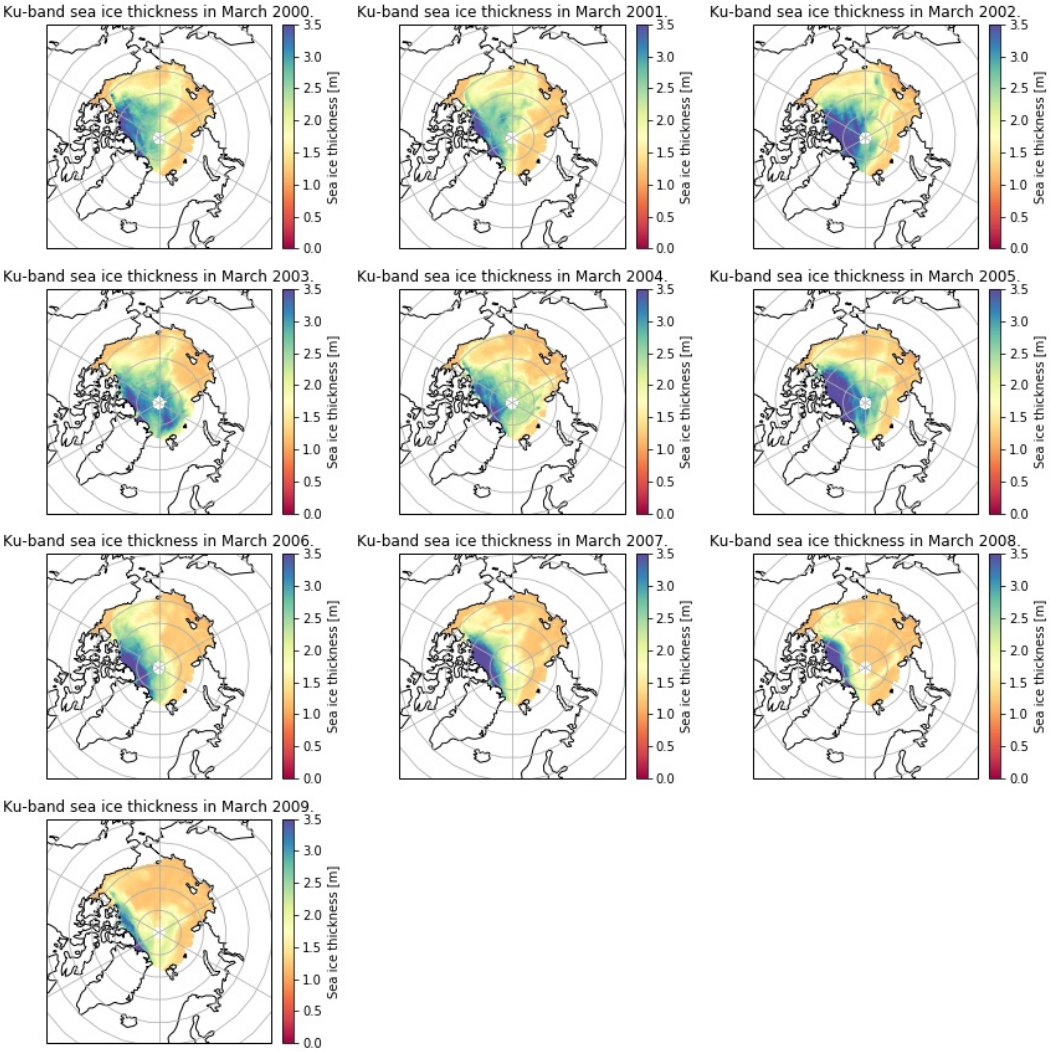

Figure F.2: QuikSCAT March sea ice thickness (2000-2009).

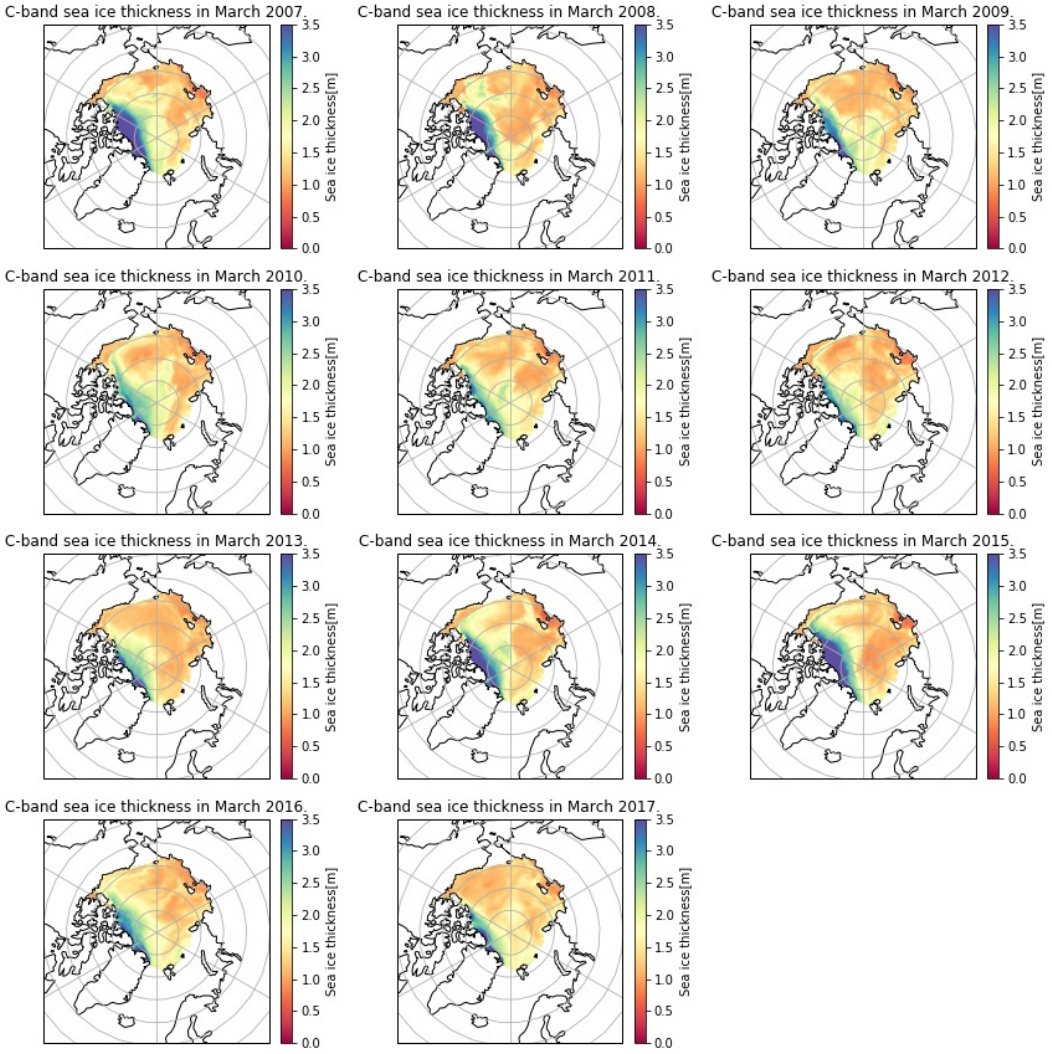

Figure F.3: ASCAT March sea ice thickness (2007-2017).

F.2. Residuals between scatterometer estimated sea ice thickness and altimeter sea ice thickness

F.2.1. QuikSCAT - ICESat (2003-2008)

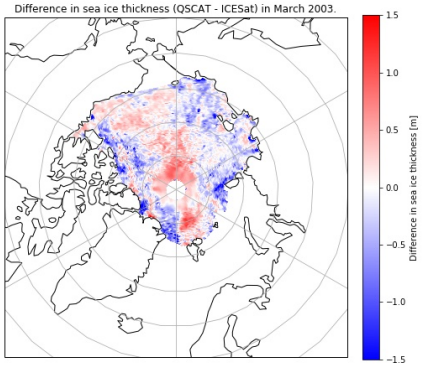

Figure F.4: QuikSCAT - ICESat residuals in March 2003.

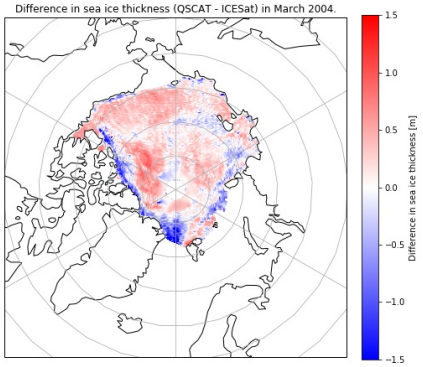

Figure F.5: QuikSCAT - ICESat residuals in March 2004.

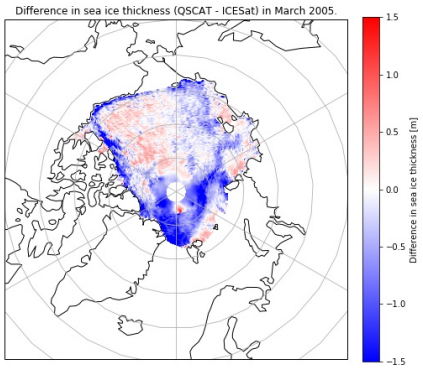

Figure F.6: QuikSCAT - ICESat residuals in March 2005.

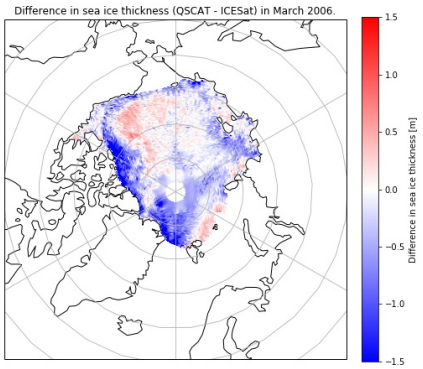

Figure F.7: QuikSCAT - ICESat residuals in March 2006.

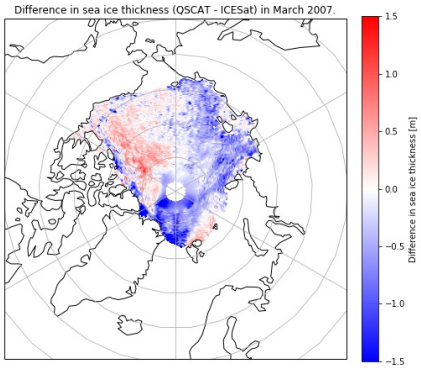

Figure F.8: QuikSCAT - ICESat residuals in March 2007.

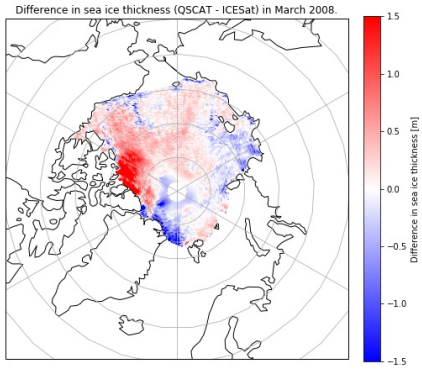

Figure F.9: QuikSCAT - ICESat residuals in March 2008.

F.2.2. ASCAT - CryoSat-2 (2011-2017)

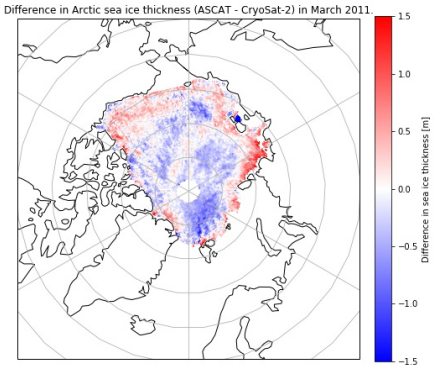

Figure F.10: ASCAT - CryoSat-2 residuals in March 2011.

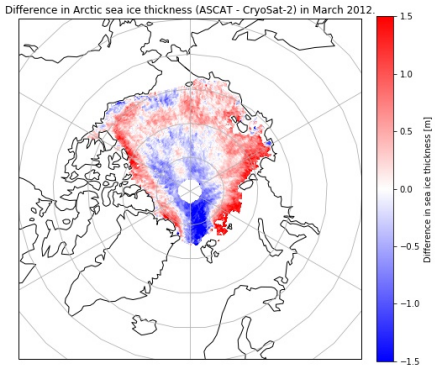

Figure F.11: ASCAT - CryoSat-2 residuals in March 2012.

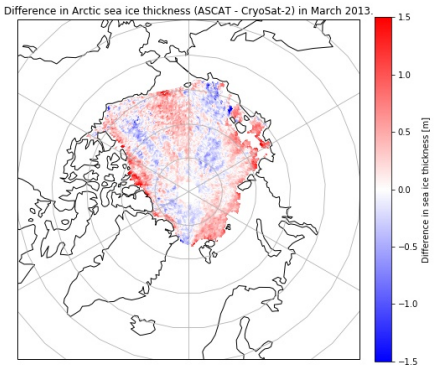

Figure F.12: ASCAT - CryoSat-2 residuals in March 2013.

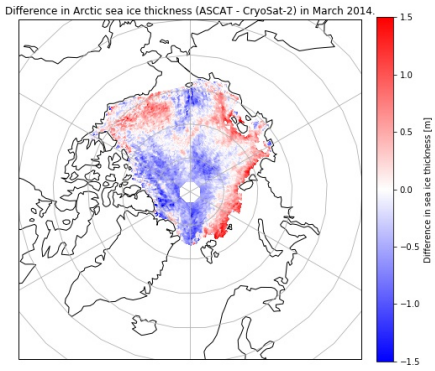

Figure F.13: ASCAT - CryoSat-2 residuals in March 2014.

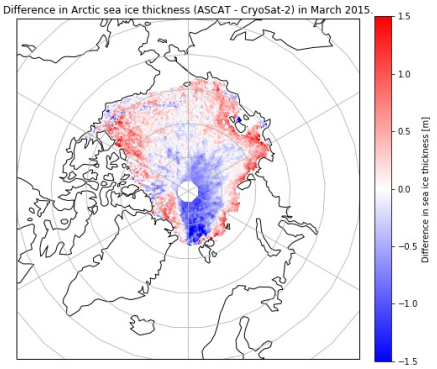

Figure F.14: ASCAT - CryoSat-2 residuals in March 2015.

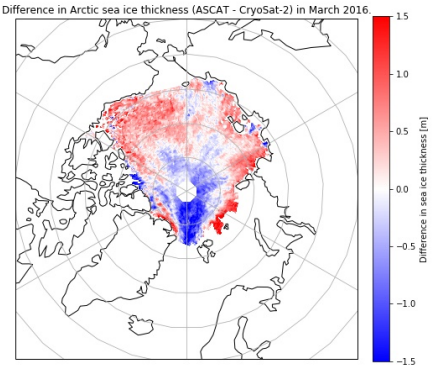

Figure F.15: ASCAT - CryoSat-2 residuals in March 2016.

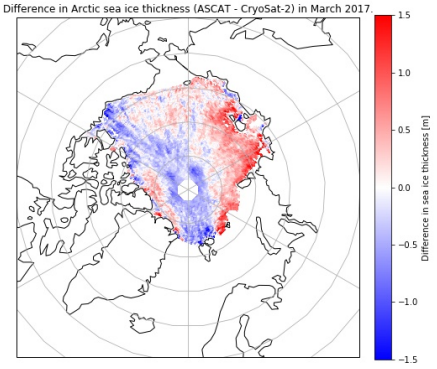

Figure F.16: ASCAT - CryoSat-2 residuals in March 2017.